Merging, fragmentation and collapse of interstellar filaments

Elena Brigitte Hoemann

München 2023

Merging, fragmentation and collapse of interstellar filaments

Elena Brigitte Hoemann

Dissertation
an der Fakultät für Physik
der Ludwig–Maximilians–Universität
München

vorgelegt von
Elena Brigitte Hoemann
aus Köln

München, den 28.08.2023

Erstgutachter: Prof. Dr. Andreas Burkert
Zweitgutachter: Prof. Dr. Paola Caselli
Tag der mündlichen Prüfung: 16. Oktober 2023

Zusammenfassung

Sterne haben die Menschen schon seit jeher fasziniert und Beobachtungen zeigten bereits vor Jahrzehnten, dass leichte Sterne filamentartigen Strukturen entspringen. Dennoch ist der Entstehungsprozess dieser Filamente sowie deren Entwicklung und Fragmentierung in einzelne Kerne bislang nicht hinreichend verstanden. Wie ich in der vorliegenden Arbeit, die neue Erkenntnisse zur Dynamik, Fragmentierung und zum Kollaps von Filamenten ermöglicht, zeige, spielt das Aufstellen, Verstehen und Vergleichen von Zeitskalen hierbei eine wesentliche Rolle.

Von zentraler Bedeutung hierbei ist die Zeitskala, auf der Filamente kollabieren, denn diese bestimmt ihre Lebensdauer und somit den zeitlichen Rahmen in dem physikalische Prozesse innerhalb des Filaments ablaufen können. Da es keine hydrostatische Lösung entlang der Hauptachse eines Filaments gibt, sind diese nicht stabil. Aus theoretischer Sicht müssen somit alle Filamente einem longitudinalen Kollaps unterliegen, wobei sich durch das Profil der Beschleunigung eine Verdichtung an jedem Ende des Filaments bildet. Dies ist der sogenannte „Edge Effect“. Die vorliegende Arbeit zeigt, dass der Filament-Kollaps in einem zweistufigen Prozess abläuft. Die erste Phase ist dominiert durch Eigengravitation, die zu einem beschleunigten Kollaps führt. In der zweiten Phase erfährt die Verdichtung am Ende des Filaments einen Staudruck durch das Material im Inneren des Filaments, was zu einer gleichförmigen Bewegung führt. Ausgehend von diesen Erkenntnissen lässt sich der Kollaps analytisch beschreiben und eine Kollapszeit berechnen, welche mit empirischen Betrachtungen übereinstimmt.

Unsere Studien zeigen, dass die Zeitskala, auf denen Filamente kollabieren, und somit auch der Edge Effect stark vom Dichtegradienten in der Endregion abhängt. Auch wenn er den Kollaps nicht aufhalten kann, so kann er diesen verlangsamen. Wird der Kollaps hinreichend verlangsamt, können Störungen schneller anwachsen, was zur Fragmentation entlang des Filaments führt. Das erklärt, weshalb der Edge Effect seltener beobachtet wird, als bisher theoretisch erwartet. Auf Basis unserer Ergebnisse ist zu erwarten, dass die meisten Filamente Dichtegradienten am Ende besitzen, die größer sind als der kritische Gradient, bei dem der Edge Effect und das Anwachsen der Störungen gleich schnell sind.

Eine Verlangsamung des Filament Kollaps ermöglicht den Ablauf von Prozessen, welche auf ähnlichen Zeitskalen stattfinden, wie zum Beispiel das Verschmelzen von Filamenten. Ich zeige in dieser Arbeit, dass es ohne die Verlangsamung des Kollapses bestimmte Rahmenbedingungen braucht, unter denen eine Verschmelzung überhaupt möglich ist. Die notwendigen Grenzwerte verschieben sich durch die Verlangsamung und machen eine Verschmelzung deutlich wahrscheinlicher. Durch die Verschmelzung unterliegen Filamente einer langanhaltenden Oszillation, die auch in der Geschwindigkeitsdispersion und der Säulendichte beobachtbar ist. In beispielhaften Filamenten der Orion-Region haben wir Hinweise auf ähnliche Strukturen gefunden.

Schlussendlich gebe ich noch einen Ausblick, wie maschinelles Lernen Simulationen von Filamenten beschleunigen kann. Wir haben ein Netzwerk entwickelt, das die Abschwächungskoeffizienten von interstellarer ultravioletter Strahlung bei bekannter Dichteverteilung bestimmt, was rechnerisch deutlich effizienter ist als herkömmliche Methoden. Große Strukturen werden gut reproduziert, jedoch ist die Reproduktion von kleinen und dichten Strukturen noch nicht hinreichend akkurat.

Abstract

Stars have always fascinated people and already decades ago observations showed that low-mass stars originate from filamentary structures. Nevertheless, the formation process of these filaments, as well as their evolution and fragmentation into individual cores, is not yet sufficiently understood. As I will show in this thesis, which provides new insights into the dynamics, fragmentation and collapse of filaments, determining, understanding and comparing timescales plays a crucial role, in this regard.

The timescale on which filaments collapse is of key importance because it determines their lifetime and therefore the timeframe in which physical processes can take place within the filament. Since there is no hydrostatic solution, filaments are not stable along their main axis. From a theoretical point of view, all filaments must therefore collapse in longitudinal direction with a compression forming at each end of the filament due to the profile of the acceleration. This is the so-called 'edge effect'. The present thesis demonstrates that the filament collapse is a two-phase process. The first phase is dominated by the self-gravity of the filament, leading to an accelerated collapse. In the second phase, the condensations at the end of the filament experience the ram pressure of the material inside the filament, leading to a uniform movement. With these findings, the collapse can be described analytically and a collapse timescale can be determined which agrees well with empirical results.

Our studies show that the timescale on which filaments collapse, and therefore also the edge effect, strongly depends on the density gradient in the end region. Although a density gradient cannot stop the edge effect, it can slow it down. If the slow-down is sufficiently large, perturbations can grow faster than the edge, leading to fragmentation along the filament. This explains why the edge effect is observed less than theoretically expected. Our results suggest that most of the filaments are required to have density gradients shallower than the critical gradient, for which the edge effect and the perturbations grow on the same timescale.

The slow down of the filament collapse allows processes to occur that happen on similar timescales as, for example, filament mergers. In this work, I show that without slowing down the collapse, special initial conditions have to be met in order to make filament mergers possible. The necessary thresholds are shifted due to the slow-down, making a filament merger much more probable. The merger induces long-lived oscillations which can be observed in velocity dispersion and column density. We found evidence of similar signatures in exemplary filaments in the Orion region.

Finally, I will give an outlook on how machine learning can speed up simulations of filaments. We developed a network that predicts attenuation coefficients of interstellar ultraviolet radiation given a certain density distribution and which is computationally much more efficient than traditional methods. The overall structure is well reproduced, whereas the determination of small and dense features needs further improvement.

Contents

Chapter 1

Introduction

1.1 The interstellar medium

The space between the stars is everything but empty. It is filled with what is called the interstellar medium (ISM), a mixture of gas and dust. The ISM is a complex medium, spanning several orders of magnitude in density and temperature and hosting all the relevant processes inside a galaxy, from stellar birth over planet formation to supernovae explosion and the creation of black holes. Thus, a deeper understanding of its internal structure is necessary to comprehend the bigger picture of galaxies and star formation.

In the following, I will go into more detail on the composition of the ISM, how to observe it and how it is a self-sustaining process.

1.1.1 Phases of the ISM

The interstellar medium consists of 74% hydrogen, 15% helium and 1% other elements (Williams, 2021). It is a multi-phase medium spanning about six orders of magnitude in temperature and five orders of magnitude in density. Thus, each phase is governed by different physical processes, which I will describe in the next paragraphs in more detail following Williams (2021). An overview of the components is given in Figure 1.1. It shows in-plane observations of the different ISM components of the Milky Way. In the top row, stellar light is given as a reference.

Atomic gas
The most massive component in the ISM consists of atomic hydrogen, also known as HI clouds. The kinetic energy in these clouds is too low to excite hydrogen by collisions. However, the hyperfine splitting of the ground state can be observed, the 21 cm line. Since it is a forbidden transition its spontaneous emission is long-lived ($\sim 11\,\mathrm{Myr}$) and rare. Nevertheless, it still occurs often enough to be detected, because of the large amount of hydrogen atoms.

The 21 cm line lies in the radio regime ($300\,\mu\mathrm{m} < \lambda < 10\,\mathrm{m}$) where also the ionised and molecular gas emit. Due to its long wavelength, its angular resolution is limited, however, combining several dishes into an interferometric array can increase the resolution. An example of such an array is the Atacama Large Millimeter Array, short ALMA, in Chile. It consists of 50 dishes with each a diameter of 2 m.

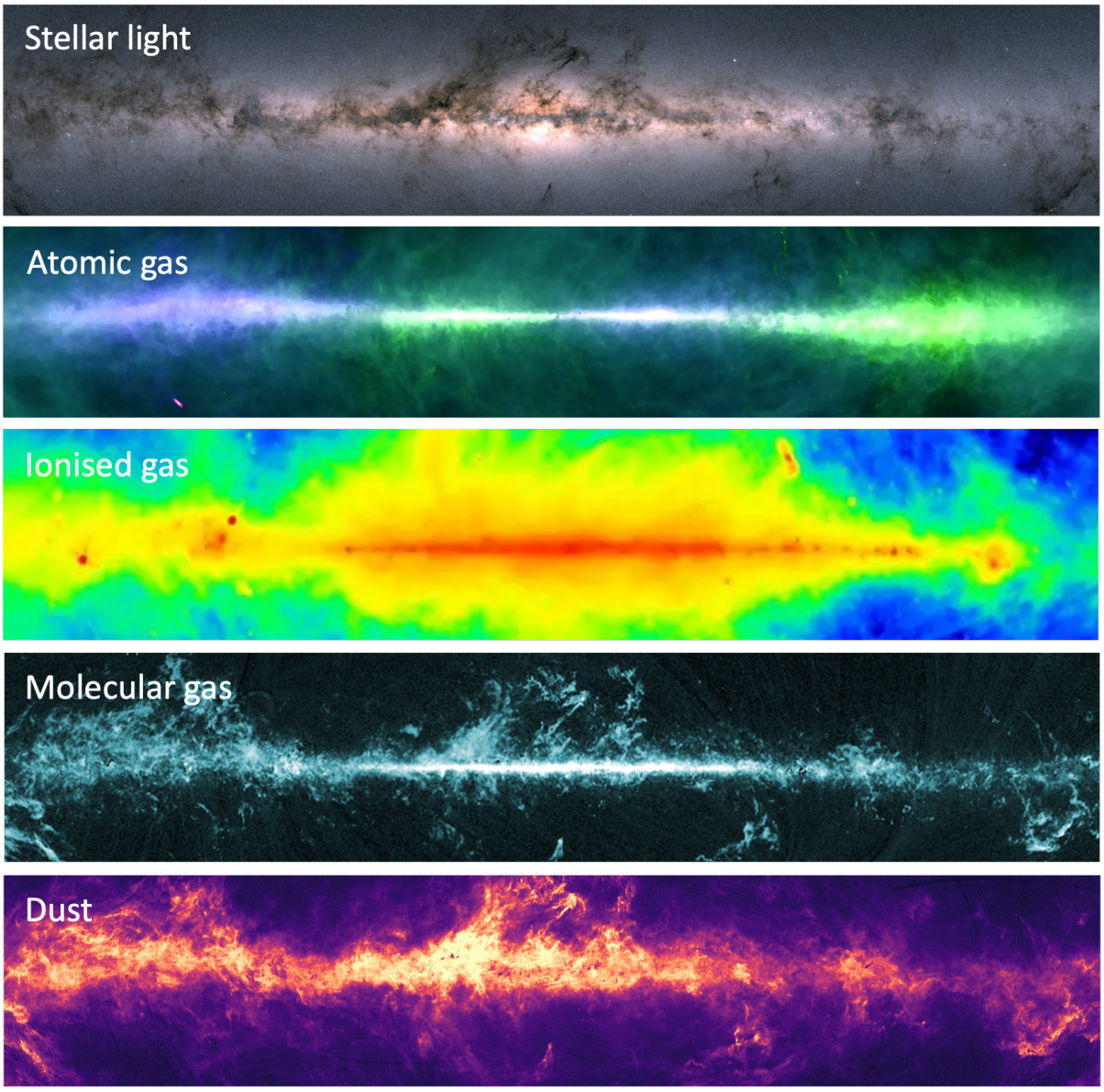

Figure 1.1: In-plane observations of the different ISM components in the Milky Way as indicated in the pictures. (Picture credits: Starlight/Dust - ESA/Gaia/DPAC, CC BY-SA 3.0 IGO; Atomic gas - HI4PI Collaboration; Ionised gas - Max Planck Institute for Radio Astronomy, Haslam et al. (1982); Molecular gas - ESA and the Planck Collaboration)

The atomic gas can be subdivided into two different phases. The *warm neutral medium* with a number density of $n \sim 10^6\,\mathrm{m}^{-3}$, a temperature of $T \sim 8000\,\mathrm{K}$ and the *cold neutral medium* with $n \sim 10^8\,\mathrm{m}^{-3}$, $T \sim 100\,\mathrm{K}$. There is an abrupt change in the cooling function when some hydrogen atoms can be excited via the Lyman alpha transition, below this temperature HI clouds are mostly cooled by line emission of oxygen and carbon. This leads to a cooling instability and two stable constellations which can coexist having the same pressure, but different temperatures and densities (Field, 1965; Field et al., 1969). Absorption features of background stars give insights into the composition of the atomic component.

Ionised gas
Hot stars emit a lot of ultraviolet (UV) radiation which is sufficient to ionise their surroundings. Since recombination in these diffuse areas is slow this component builds a low-density plasma with densities of $\sim 10^{-3}\,\mathrm{cm}^{-3}$ and temperatures around $\sim 10^6\,\mathrm{K}$ (McKee & Ostriker, 1977). Although dust sublimates at 1600 K it can survive in these hot environments, since the dust decouples from the gas and can cool to much lower temperatures via continuum emission, as a result of the low densities. The gas is heated by the fast-moving photoelectrons and cools via escaping radiation. Because of the high temperatures a lot of different processes occur producing radiation at various wavelengths. Line cooling is mainly accomplished via forbidden transitions, but also the continuum emission from bremsstrahlung of deflected electrons and synchrotron radiation from relativistic protons in the magnetic field are important.

Molecular gas
In very dense ($n \sim 100\,\mathrm{cm}^{-3}$) regions of the ISM, which are shielded from energetic radiation, molecules can form. The most abundant molecule is molecular hydrogen. However, it is not detectable due to the cold temperatures $\sim 10\,\mathrm{K}$ which are not sufficient to excite electrons from the ground state. Much higher temperatures are needed (around 500 K) to excite rotational modes since the symmetry of the hydrogen molecule leads to a vanishing dipole moment. Thus, different tracers are used to detect the molecular component of the ISM, such as dust or asymmetric molecules like carbon monoxide (CO), which can be detected in the mm regime. Although the dust shields the molecular clouds from optical and UV irradiation, cosmic rays, highly energetic particles, can still penetrate in these dense regions. They ionise H_2 and the freed electron can excite more molecules. Goldsmith & Langer (1978) showed that a temperature of 10 K is reached for an equilibrium between cosmic ray heating and line cooling, mostly by the rotational lines of CO. As the line width of the transition was observed to be much wider than predicted at that temperature, the molecular regions are expected to be turbulent, with a velocity dispersion scaling relation of $\sigma \propto R^{0.5}$ known as one of the Larson's relations (Larson, 1981; Solomon et al., 1987; Heyer et al., 2009), with R the radius of the cloud and σ the velocity dispersion.

Dust
One per cent of the total mass of the ISM is found to be in dust grains (Bohlin et al., 1978). These are created during the expansion of stellar winds, which cool and then condense to solid particles. The size distribution between $0.005 - 1.0\,\mu\mathrm{m}$ is given by a power law with

an exponent of -3.5 (Mathis et al., 1977; Draine & Lee, 1984). In comparison to the gaseous components of the ISM, dust interacts with light over a broad wavelength range. Since they absorb in the ultraviolet and optical regime, they appear as black patches in the sky when observed by eye. Due to the wavelength-dependent absorption, the light of background stars appears redder if absorbed through a dusty cloud which is called extinction. Since the dust particles are much cooler than these background sources, they emit at a much longer wavelength than they absorb, in the infrared.

The infrared regime is subdivided into three groups, the near-infrared $\sim 0.8 - 2.4\,\mu m$ dominated by starlight, the mid-infrared $\sim 2.4 - 25\,\mu m$ where observations of warm dust and molecular transitions are possible, and the far infrared $\sim 25{-}300\,\mu m$ the emitting regime of cold dust. The wavelength range corresponds to the spectrum of a black body of $10 - 4000\,K$. Since far infrared radiation cannot easily transmit through the Earth's atmosphere space telescopes like Spitzer and Herschel are used for observations in this wavelength regime. However, both missions have ended and there is currently no operating alternative.

Although most of the dust mass is provided by larger grains, the small ones provide the larger surface area. The surface area is important for the chemical processes happening in molecular clouds since they are much more likely to happen on the surface of dust grains, especially the formation of molecular hydrogen (Gould & Salpeter, 1963; Hollenbach & Salpeter, 1971). On those surfaces, the relative velocities of the reactants are nearly zero and the energy excess of a chemical reaction can be transferred to the grain.

1.1.2 Life cycle of the ISM

The ISM undergoes a self-regulating cycle, sketched in Figure 1.2, connecting the different phases of the ISM. The diffuse and hot component of the interstellar medium condenses into thicker regions, where the UV irradiation from outside is blocked. In these cold environments, molecules can form. Decades ago, observations already showed that these molecular clouds are pervaded by filaments, being dense, cold, cylindrical substructures (Schneider & Elmegreen, 1979). These have been shown to be stellar nurseries (Arzoumanian et al., 2011; Könyves et al., 2015), since most of the low-mass prestellar cores are found within them. This is what makes them so interesting, since they are the pre-phase of star formation. A deeper understanding of their evolution and fragmentation is necessary to understand, how stars are formed. While the cores in filaments collapse to form stars, discs are created around the prestellar object due to the conservation of angular momentum. In these discs, planetary systems such as our own solar system form. During the lifetime of a star, especially in its later stages, a lot of matter is ejected back into the interstellar medium. The most disruptive event in this regard are supernovae. When luminous stars collapse at the end of their lifetime their collapse as supernova releases around $\sim 10^{51}\,erg/10\,M_\odot$ (for a type II supernova, Rubin et al., 2016) which disrupts the surrounding medium. These processes enrich the ISM with heavy elements formed during stellar evolution, bringing it back in to a more diffuse state and the cycle starts all over again.

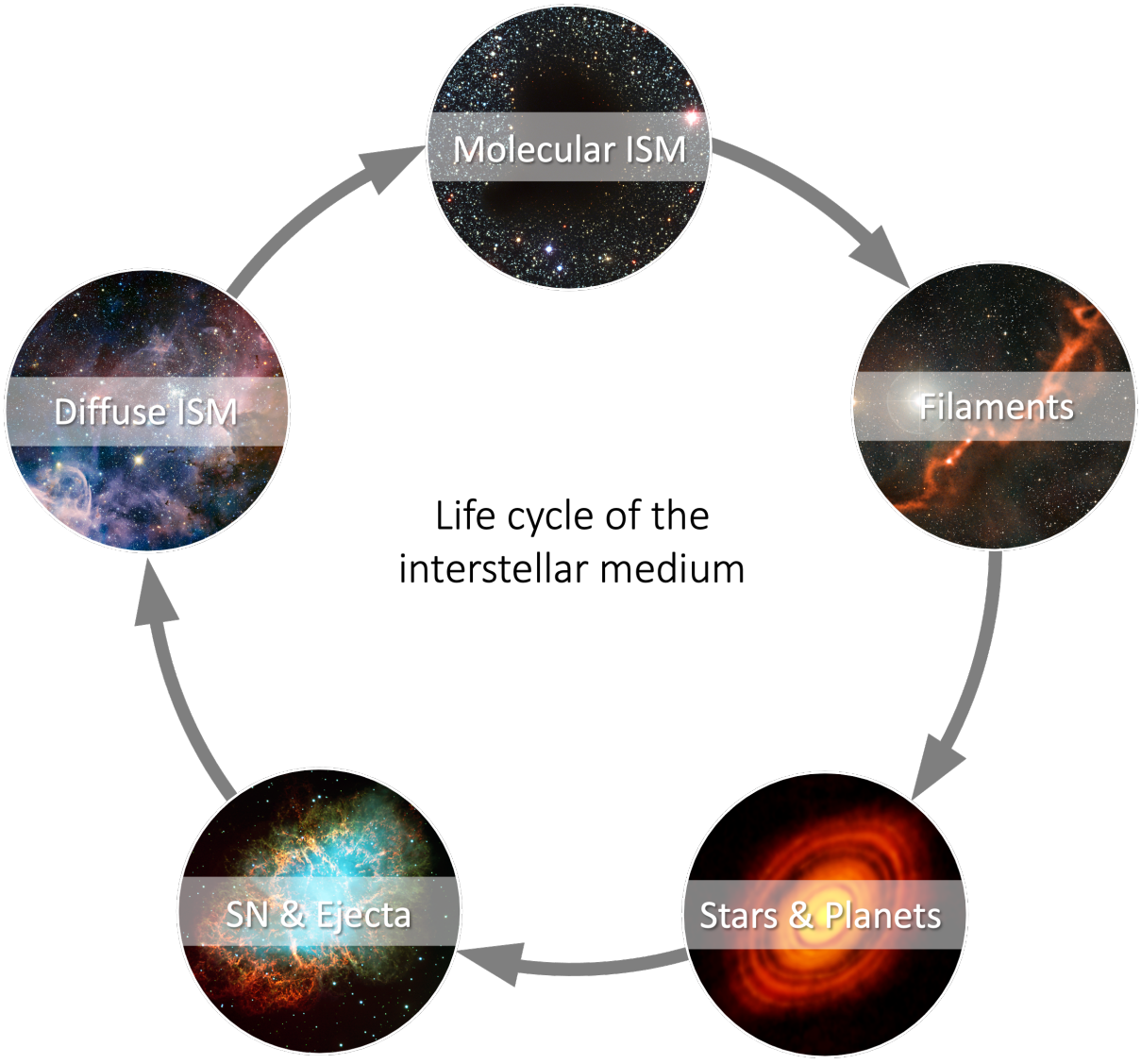

Figure 1.2: Life cycle of the gas in the interstellar medium. Starting with a diffuse cloud, these collapse into dense regions where molecules can be created. Inside the clouds filaments form which collapse to stars with protoplanetary discs, where also planets can be created. Especially at the end of a star's lifetime a lot of its matter is ejected back into the diffuse ISM. (Picture credit: Diffuse ISM - ESO/T. Preibisch; Molecular ISM - ESO; Filaments - ESO/APEX (MPIfR/ESO/OSO)/A. Hacar et al./Digitized Sky Survey; Stars & Planets - ALMA (ESO/NAOJ/NRAO); SN & Ejecta - ESO; CC BY 4.0)

1.2 Filaments

It is known that the molecular phase of the interstellar medium (ISM) is pervaded by filamentary substructure. Filaments are the cylindrical and cold density enhancements where pre-stellar cores are forming (Arzoumanian et al., 2011; Könyves et al., 2015). Therefore, filaments are important for understanding the physics of star formation. They have been observed across various different regions and they span several orders of magnitude from the sub-parsec regime to hundreds of parsec in length (Hacar et al., 2023).

In the following, I will go into detail about the theory of filaments in hydrostatic equilibrium as well as their fragmentation, in particular the edge effect and perturbation-induced fragmentation, followed by an overview of some observational findings in comparison.

1.2.1 Hydrostatic filaments

Considering filaments are perfect gaseous cylinders. In hydrostatic equilibrium the gradient of the potential Φ has to counterbalance the pressure gradient ∇P:

$$-\nabla\Phi = \frac{1}{\rho}\nabla P, \tag{1.1}$$

ρ being the density. For the following, we will solve only for the radial component r of the filament. For an isothermal solution, the equation of state is given by the law for ideal gases:

$$P = \frac{kT}{\mu m_0}\rho, \tag{1.2}$$

with k the Boltzman constant, T the temperature and μ the particle mass times m_0, the atomic mass constant. By applying some algebra and the substitution $r \propto \xi$ and $\rho = \rho_\mathrm{c}\exp(-\psi)$, where ρ_c is the central density of the filament, we get the cylindrical form of the Lane-Emden-Equation:

$$\frac{\mathrm{d}^2\psi}{\mathrm{d}\xi^2} + \frac{1}{\xi}\frac{\mathrm{d}\psi}{\mathrm{d}\xi} = e^{-\psi}. \tag{1.3}$$

Ostriker (1964) and Stodólkiewicz (1963) derived the radial profile which solves Equation 1.3. Thus, for this radial density distribution filaments are in hydrostatic equilibrium

$$\rho(r) = \rho_\mathrm{c}\left[1 + \left(\frac{r}{H}\right)^2\right]^{-2}, \tag{1.4}$$

where H is the scale height given by

$$H^2 = \frac{2c_\mathrm{s}^2}{\pi G\rho_\mathrm{c}}, \tag{1.5}$$

with c_s being the speed of sound, which is $0.19\,\mathrm{km\,s^{-1}}$ for a molecular weight of 2.36 and a temperature of 10 K (Fischera & Martin, 2012) and G the gravitational constant. An example is given in Figure 1.3. Integrating the displayed profile for $[0, \infty]$ gives the

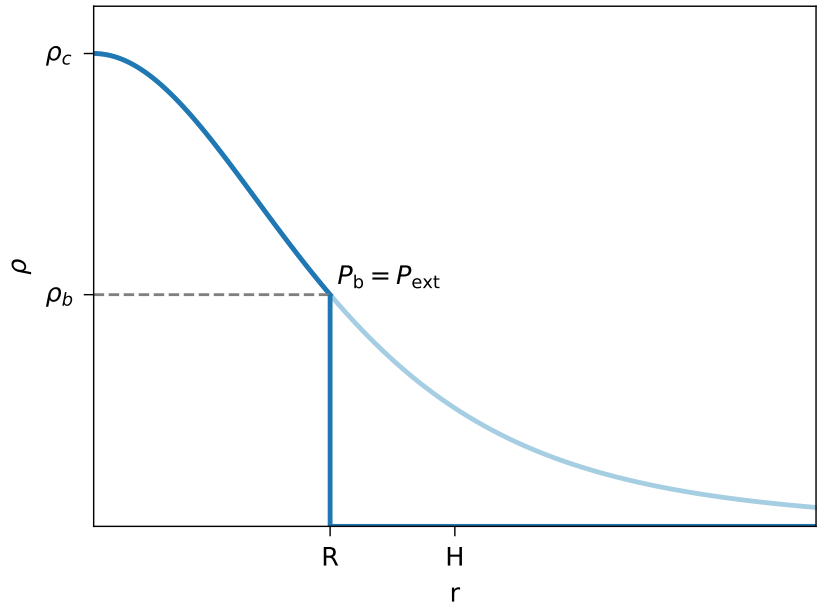

Figure 1.3: Radial profile of a filament in hydrostatic equilibrium, (Equation 1.4). At pressure equilibrium between the pressure inside and outside of the filament, the filament is cut off. The boundary density ρ_b determines the radius R.

maximal mass per length called line-mass ($\mu \equiv M/L$ the mass of the filament divided by its length) for which a filament can be in hydrostatic equilibrium, the critical line-mass:

$$\mu_{\mathrm{crit}} = \frac{2c_s^2}{G} \approx 16.4\,\mathrm{M}_\odot\,\mathrm{pc}^{-1}. \tag{1.6}$$

Above this value, all filaments would start to collapse radially (Fischera & Martin, 2012). Therefore, the criticality f of the filament is defined as the ratio of the line-mass divided by the critical line-mass:

$$f = \frac{\mu}{\mu_{\mathrm{crit}}}. \tag{1.7}$$

In reality, filaments certainly do not extend infinitely but are constrained by the outside pressure confining the filament to a certain radius. With

$$\rho_b = \rho_c(1-f)^2 \tag{1.8}$$

being the boundary density at pressure equilibrium between the external pressure and the pressure of the boundary of the filament ($P_{\mathrm{ext}} = P_b$, Figure 1.3). The outside material then has a higher temperature and thus a lower density, which induces a cut-off at radius R:

$$R = H\left(\frac{f}{1-f}\right)^{1/2}. \tag{1.9}$$

1.2.2 Edge effect

As discussed in the previous section a filament can be radially in hydrostatic equilibrium. In contrast, there is no solution for the main axis of a filament. Thus, every filament should theoretically be collapsing longitudinally due to its self-gravitation, the process is depicted in Figure 1.4. The acceleration a along the filament due to self-gravity was already investigated by Burkert & Hartmann (2004):

$$a = -2\pi G\bar{\rho}\left[2z - \sqrt{\left(\frac{l}{2}+z\right)^2 + R^2} + \sqrt{\left(\frac{l}{2}-z\right)^2 + R^2}\right] \tag{1.10}$$

with $\bar{\rho}$ the mean density and z the position along the filament and l its length. In Figure 1.4, a sketch of the acceleration is given in the graph on the upper left-hand side. The acceleration is calculated for a filament with a constant density inside and a sharp cut-off to the surrounding medium, I will discuss in Chapter 4 (Hoemann et al., 2023b) how this approximation influences the filament fragmentation and collapse. However, because of the strong increase of acceleration at the end of the filament, matter is piled up in these regions while everything falls into the centre. Thus, cores are forming in the end regions during the overall collapse. This is the so-called 'edge effect' (Bastien, 1983).

In the first paper (Chapter 2, Hoemann et al., 2021) we determined the time scale on which end cores are built, the edge effect formation timescale t_{edge}, considering the acceleration given above:

$$t_{\mathrm{edge}} = \sqrt{\frac{1.69 \times 10^{-20}\,\mathrm{g\,cm^{-3}}}{f\rho_{\mathrm{c}}}}\,\mathrm{Myr} \tag{1.11}$$

In addition, the overall collapse timescale determines the lifetime of a filament. There have already been several investigations (Toalá et al., 2011; Pon et al., 2012) and the latest by Clarke & Whitworth (2015) to quantify the filaments' lifetime. They found, that due to ram pressure, the end cores reach a terminal velocity after about 1 Myr. Due to the fit to simulated data, they found the collapse timescale t_{col}. In the second paper (Chapter 3, Hoemann et al., 2023a) we found the derivation this timescale

$$t_{\mathrm{col}} = \frac{0.42 + 0.28A}{\sqrt{G\bar{\rho}}} \tag{1.12}$$

and an analytic description of how the merger evolves.

Although the edge effect has been theoretically expected to occur rapidly, it was only observed in limited cases (Zernickel et al., 2013; Kainulainen et al., 2016; Bhadari et al., 2020; Yuan et al., 2020; Cheng et al., 2021). One exemplary observation of S 242 by Dewangan et al. (2019) is shown in Figure 1.4 on the lower left-hand side. Nevertheless, this results in a big puzzle: what is the cause for observing the edge effect only rarely, although it is theoretically expected to appear frequently?

There have already been some works for different collapse modes. Seifried & Walch (2015), for example, found that an initial density peak in the centre leads to a centrally dominated filament collapse. This was also investigated by Keto & Burkert (2014) for filaments with length to radius ratio of 3:1, although the necessary perturbations have not

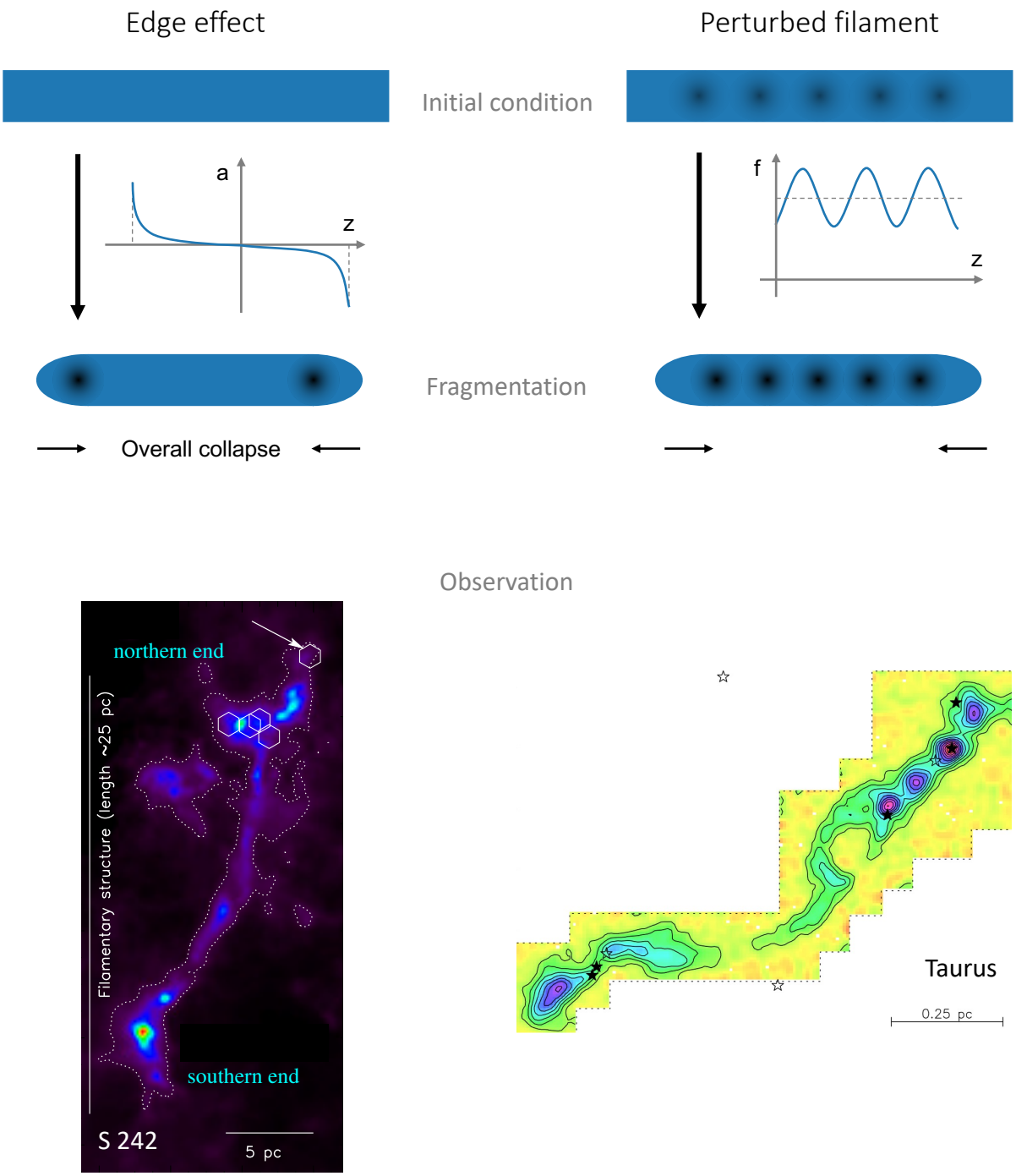

Figure 1.4: Fragmentation mechanisms in filaments. Left: Fragmentation through the edge effect. A filament of constant density along its main axes has a sharp increase in acceleration at the end of the filament, due to self-gravitation. Thus, cores are formed at the end during the overall collapse. An observed example is S242 (Picture credit: Dewangan et al., 2019, CC BY 4.0). Right: Fragmentation through the growth of perturbations. Initial perturbations in line-mass can grow over time. An example of this core formation along the filament is given in Taurus (Picture credit: Tafalla & Hacar, 2015, CC BY 4.0).

been observed, the expected oscillating cores have been (Redman et al., 2006; Aguti et al., 2007). A different possibility was suggested by Heigl et al. (2022), where the filament is built and constantly fed by a converging flow. Since the filament is contracting inside the constant inflow region the ends are recreated behind the filament ends, this matter reduces the acceleration at the end of the filament which slows down the creation of end cores. In Chapter 4 I show that whether the edge effect is suppressed or not depends on the density gradient at the end of the filament.

1.2.3 Perturbations in filaments

A second mode of fragmentation is given through the growth of perturbations inside the filament for which a corresponding sketch is given in Figure 1.4 on the right-hand side. Considering a perturbation strength of ϵ and a wavelength λ leads to the following perturbation in the criticality (equivalent to line-mass perturbations):

$$f(z) = f_0 \left[1 + \epsilon \cos\left(\frac{2\pi z}{\lambda}\right)\right]. \tag{1.13}$$

Hershel observations in the Pipe, Taurus and IC 5146 molecular cloud revealed perturbations in the line-mass of about $\epsilon = 0.09$ (Roy et al., 2015). The perturbations grow over time, resulting in cores forming along the filament. An example observation of Taurus (Tafalla & Hacar, 2015) is shown in Figure 1.4 on the lower right.

Nagasawa (1987) already performed a comprehensive perturbation analysis. Fischera & Martin (2012) then found a polynomial approximation of the characteristic scales for the growth of perturbations: First, they approximated the critical wavelength $\lambda_{\rm crit}$ which is at least needed for perturbations grow. Second, the dominant wavelength $\lambda_{\rm dom}$ was determined for which perturbations grow most efficiently and third its corresponding growth timescale $\tau_{\rm dom}$. $\lambda_{\rm crit}/FWHM$, $\lambda_{\rm dom}/FWHM$ and $\tau_{\rm dom}\sqrt{4\pi G\rho_{\rm c}}$, represented by y, are approximated by a fourth-order polynomial of the criticality, with coefficients a_i:

$$y(f) = \sum_{i=0}^{4} a_i f^i. \tag{1.14}$$

The associated full width at half maximum $FWHM$ is given in terms of the scale height H by:

$$FWHM/H = \sum_{i=0}^{5} a_i f^{i/2}. \tag{1.15}$$

The coefficients a_i are given in Table 1.1 and a visualisation of the wavelength and the dominant growing timescale is displayed in Figure 1.5 depending on the criticality f.

Using the dominant fragmentation mode $\lambda_{\rm dom}$ we can determine how much mass a single core induced by initial perturbations could accrete. This results in an upper mass for cores formed via perturbations in filaments:

$$M = \lambda_{\rm dom} f \mu_{\rm crit}. \tag{1.16}$$

Figure 1.6 shows the expected masses depending on the criticality f for different radii R. This shows that high-mass stars cannot be formed via perturbations, since not enough mass can be transferred to a single core in this scenario.

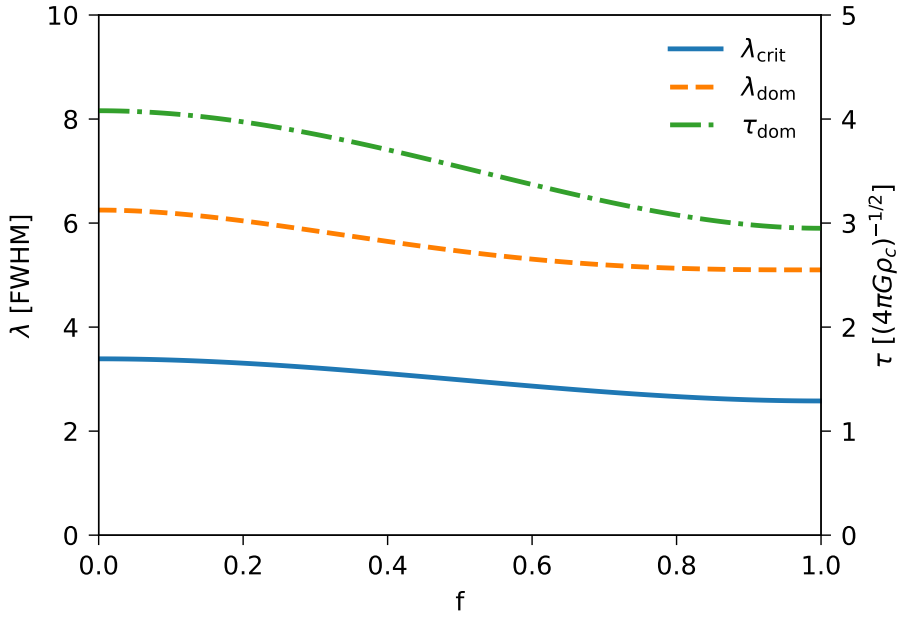

Figure 1.5: The dominant and critical fragmentation length, with the y-axis on the left-hand side and the dominant perturbation timescale depending on the criticality, with the y-axis on the right-hand side.

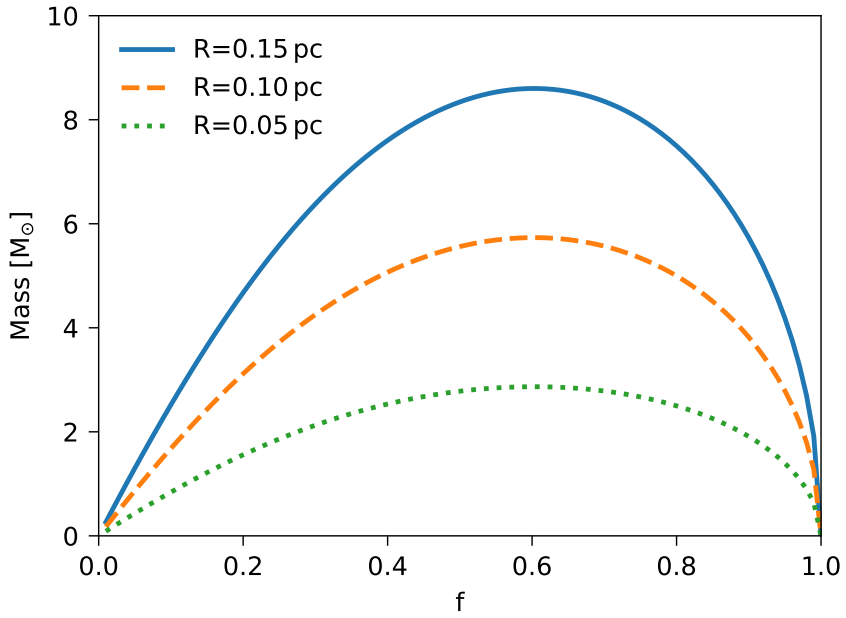

Figure 1.6: Mass of the cores which could be created by perturbations depending on the criticality of the filament and its radius.

Table 1.1: Fit parameter for the coefficients a_i of the polynomial approximation done in Fischera & Martin (2012) for the main perturbation characteristics, Equation 1.14 and 1.15.

	a_0	a_1	a_2	a_3	a_4	a_5
$\tau_{\rm dom}\sqrt{4\pi G\rho_{\rm c}}$	4.08	0.00	-2.990	1.460	0.400	0.00
$\lambda_{\rm crit}/FWHM$	3.39	0.00	-2.414	1.588	0.016	0.00
$\lambda_{\rm dom}/FWHM$	6.25	0.00	-6.890	9.180	-3.440	0.00
$FWHM/H$	0.00	1.732	0.000	-0.041	0.818	-0.976

1.2.4 Observations

Filaments are observed everywhere in the interstellar medium and on various different scales: form large structures of more than 100 pc in length like Nessie (Goodman et al., 2014; Mattern et al., 2018), infrared dark clouds (Perault et al., 1996; Alves et al., 1998; Egan et al., 1998; Hennebelle et al., 2001; Peretto & Fuller, 2009; Miettinen & Harju, 2010), to (sub-)parsec scales (Molinari et al., 2010; Arzoumanian et al., 2011; Hacar et al., 2013; Schmiedeke et al., 2021). As Figure 1.7 from Hacar et al. (2023) indicates the observed filaments in the Milky Way span eight orders of magnitude in mass and four in length with a scaling relation of

$$L \propto M^{0.5}. \tag{1.17}$$

Depending on the resolution and density threshold of the observations, filaments of different scales are detected, revealing that filaments are hierarchical structures (Hacar et al., 2013; Fehér et al., 2016). The black dashed line indicates the critical line-mass for $T = 10\,\mathrm{K}$, above which filaments cannot be in hydrostatic equilibrium (see Section 1.2.1). As can be seen, longer filaments are predominantly supercritical ($f > 1$) whereas subparsec and parsec-sized filaments are mainly sub-critical ($f < 1$) and accordingly in the radially stable regime. There are two theories about how these structures are created, the top-down fragmentation where larger filamentary structures fragment (Hacar et al., 2013) or the bottom-up process where due to gravitational collapse small filaments form bigger structures (Smith et al., 2014). Also, a simultaneous formation could be possible (Hacar et al., 2023).

Although there are isolated filaments as the ones shown in Figure 1.4, many filaments appear to be part of larger filamentary networks (André, 2017), for example, in the Aquila molecular cloud shown in Figure 1.8 (Könyves et al., 2015) observed with the Herschel telescope. The left Figure shows the detected filaments, indicated by the blue lines, whereas the plot on the right-hand side shows the distribution of prestellar cores in blue and protostellar cores in green. The positions of the cores fit the positions of the filaments which demonstrates what has already been discovered a long time ago (Schneider & Elmegreen, 1979): prestellar cores are formed within filaments (Arzoumanian et al., 2011; Könyves et al., 2015). Therefore, they play a crucial role in the process of star formation, especially their fragmentation and collapse.

In addition to filamentary networks, hubs are systems, where the central clump is fed by several converging filaments (Myers, 2009; Schneider et al., 2010; Treviño-Morales et al., 2019). Their line-masses usually exceed the critical line-mass drastically (Schneider et al., 2010; Hill et al., 2011) and they are supposed to be the origin of high-mass stars and

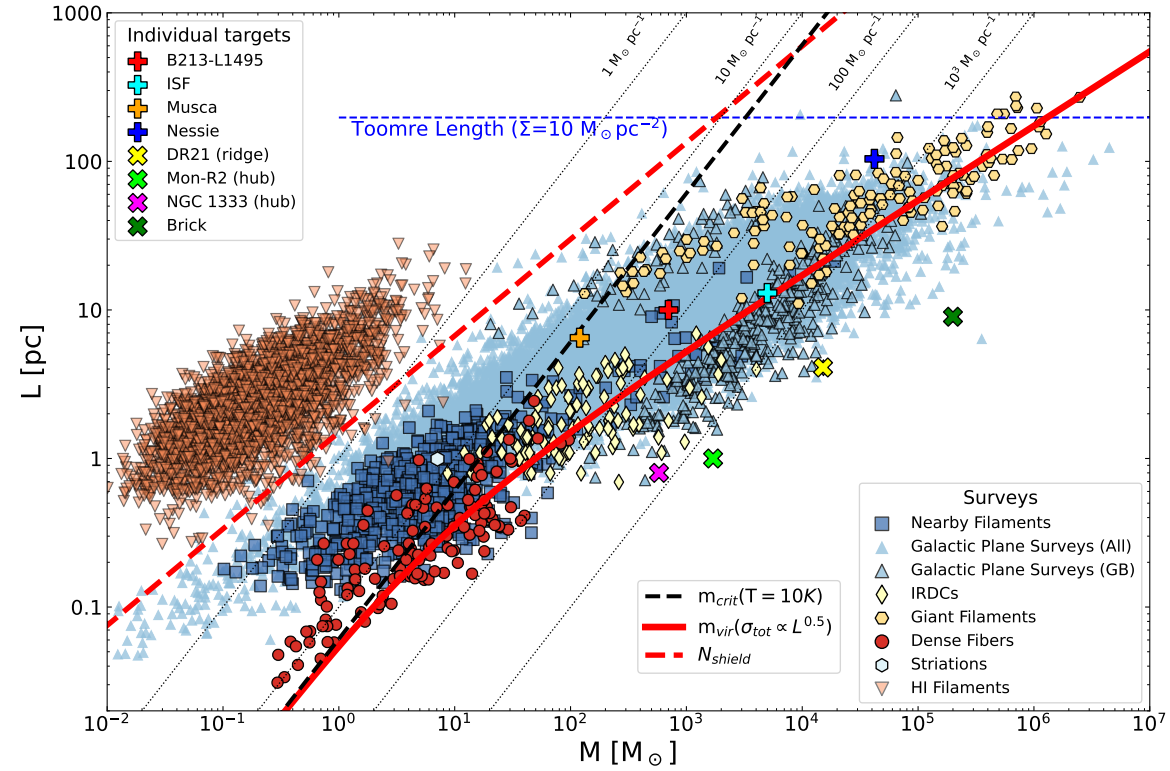

Figure 1.7: The mass length relationship for filaments in the Milky Way. The black dashed line indicates the critical line-mass for 10 K.
(Picture credit: Hacar et al., 2023, CC BY 4.0)

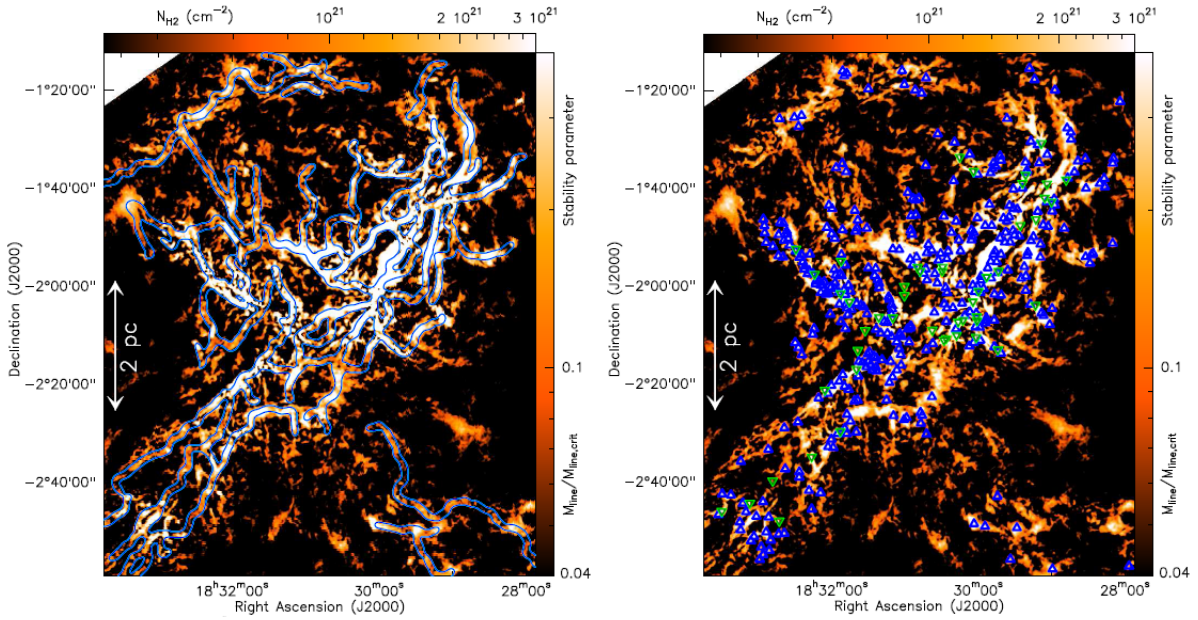

Figure 1.8: Filamentary network in the Aquila starforming region. The left-hand side shows the distributions of the filaments given by the blue contours. On the right-hand side, the distribution of cores in the same region is displayed (prestellar cores in blue and protostellar cores in green). It can clearly be seen that most of the cores are found within these filamentary structures. (Picture credit: Könyves et al., 2015, CC BY 4.0)

stellar clusters (Motte et al., 2018), since they are often associated with such structures. It is still an open question how these more complex filamentary structures are created. In Chapter 2 and 5 I discuss the scenario of filament mergers being the origin of these intricate systems.

The radial profiles of observed filaments are well described by Plummer-like curves (Arzoumanian et al., 2011):

$$N(x) = A_{\mathrm{p}} \frac{n_0 R_{\mathrm{flat}}}{\left(1 + \left(\frac{x}{R_{\mathbf{flat}}}\right)^2\right)^{\frac{p-1}{2}}}. \tag{1.18}$$

A_{p} is a proportionality constant, x the projected distance to the filament centre, R_{flat} the flat inner region, n_0 the number column density along the spine and p the exponent fitted to the observed profile. For $p = 4$ Equation 1.18 is an approximation of the column density you would observe when looking at a filament in hydrostatic equilibrium following Equation 1.4. Nevertheless, observations mainly show values between $p = 1.5 - 2.5$ (Arzoumanian et al., 2011; Palmeirim et al., 2013). The flattening of the filamentary profile in comparison to the expected one can have many different reasons such as magnetisation (Fiege & Pudritz, 2000; Tomisaka, 2014), external pressure (Fischera & Martin, 2012), nonisothermality (Recchi et al., 2013; Smith et al., 2014), a polytropic equation of state (Gehman et al., 1996) or rotation (Recchi et al., 2014).

Altogether, observations (e. g., Schneider & Elmegreen, 1979) showed already decades ago that filaments are the places where star formation happens. Thus far they revealed a lot more about their hierarchical structure, their profile and their fragmentation. Analytical models and simulations now need to show how these phenomena can be explained and how they can be placed in the bigger picture.

1.3 Hydrodynamic simulations

In observations of the interstellar medium we only see a snapshot of a specific phenomenon since the dynamical scale of filaments in the ISM is on the order of million years. Furthermore, due to our fixed perspective, only projections are observable. Therefore, to gain a deeper understanding, simulations are necessary to validate (semi-)analytic and empirical models as well as to build the bridge between theory and observation.

Since it is impossible to account for every single gas molecule in simulations, the gas has to be treated statistically. The gas can be considered as a continuum if the mean free path l is much smaller than the fluid element ϵ which needs to be much smaller than the macroscopic length scale L. The mean free path l is given by:

$$l = \frac{1}{n\sigma} \tag{1.19}$$

with n the number density and σ the cross section of a gas particle. For a HI region typical values are $n \approx 10\,\mathrm{cm}^{-3}$, $\sigma \approx 10^{-15}\,\mathrm{cm}^{-2}$ which results in a mean free path of $l \approx 10^{14}\,\mathrm{cm}$. Since these gas clouds are of the order of several parsecs $L \approx 10^{19}\,\mathrm{cm}$ (Shu, 1991) $l \ll L$ is fulfilled and thus, the assumption of a continuum is valid.

In the following section, I will go into detail about the Euler equations, which govern these continuous media and their implementation in the RAMSES code (Teyssier, 2002), which was used in the course of this thesis.

1.3.1 Euler equations

The derivation of the Euler equations, which describe the evolution of continuous media, follow loosely Shu (1991) and Bodenheimer et al. (2006).

As discussed before we can treat the gas in molecular clouds as a fluid and use statistics to describe its behaviour. Consider $f(\mathbf{x}, \mathbf{p}, t)$ being the distribution function of particles in phase space, depending on the position $\mathbf{x}$ and its momentum $\mathbf{p}$ at time t. Then the number of particles within a phase space element $\mathrm{d}\mathbf{x}, \mathrm{d}\mathbf{p}$ is determined by:

$$\mathrm{d}N = f(\mathbf{x}, \mathbf{p}, t)\mathrm{d}\mathbf{x}\mathrm{d}\mathbf{p}. \tag{1.20}$$

The total differential of f is then given as:

$$\mathrm{d}f = \frac{\partial f}{\partial x_i}\mathrm{d}x_i + \frac{\partial f}{\partial p_i}\mathrm{d}p_i + \frac{\partial f}{\partial t}\mathrm{d}t. \tag{1.21}$$

Considering that the change in position and momentum is

$$\mathrm{d}x_i = \frac{p_i}{m}\mathrm{d}t, \tag{1.22}$$

$$\mathrm{d}p_i = F_i\mathrm{d}t, \tag{1.23}$$

where F_i donates the acting force and inserting this in Equation 1.21 leads to:

$$\mathrm{d}f = \frac{\partial f}{\partial x_i}\frac{p_i}{m}\mathrm{d}t + \frac{\partial f}{\partial p_i}F_i\mathrm{d}t + \frac{\partial f}{\partial t}\mathrm{d}t. \tag{1.24}$$

Collisions change the velocity and position of individual particles, scattering them in and out of their phase space element and, thus, modifying $\mathrm{d}f/\mathrm{d}t$. This leads to the Boltzmann Equation:

$$\left(\frac{\partial f}{\partial t}\right)_{\mathrm{coll}} = \frac{\partial f}{\partial x_i}\frac{p_i}{m} - m\frac{\partial f}{\partial p_i}\nabla_i\Phi + \frac{\partial f}{\partial t}, \tag{1.25}$$

where F_i is given by the gradient of the gravitational potential $\nabla_i\Phi$.

Considering that no particles are created or destroyed during a collision, the velocity integral over $\chi\left(\frac{\partial f}{\partial t}\right)_{\mathrm{coll}}$ is zero for conserved quantities χ, because we integrate over the complete velocity space:

$$\int \chi\left(\frac{\partial f}{\partial t}\right)_{\mathrm{coll}} \mathrm{d}^3v = 0. \tag{1.26}$$

Following the derivation in Shu (1991), we introduce the average of a quantity Q as:

$$\langle Q\rangle = n^{-1}\int Qf\mathrm{d}^3v, \tag{1.27}$$

so the Boltzmann equation can be rewritten to:

$$\frac{\partial}{\partial t}(n\langle\chi\rangle) + \frac{\partial}{\partial x_i}(n\langle v_i\chi\rangle) + \frac{\partial\Phi}{\partial x_i}n\langle\frac{\partial\chi}{\partial v_i}\rangle = 0, \tag{1.28}$$

whereas for the last term partial integration was used and the divergence theorem for $\int_{\mathrm{V}}\frac{\partial(\chi f))}{\partial v_i}\mathrm{d}^3v = \int_{\mathrm{S}}\chi f\mathrm{d}^2v$, assuming that f goes faster to zero than the growth of χ for $v\to\infty$ on the sphere. We will now evaluate the first three velocity moments:

$$\mathbf{U} \equiv \begin{pmatrix}\rho\\ \rho\mathbf{u}\\ \rho e\end{pmatrix} = \int\begin{pmatrix}m\\ mv\\ m|\mathbf{v}|^2/2\end{pmatrix} f(\mathbf{x},\mathbf{v},t)\mathrm{d}^3v. \tag{1.29}$$

Mass conservation $\chi = m$
Inserting $\chi = m$ into Equation 1.28 leads to the so-called continuity equation:

$$\frac{\partial\rho}{\partial t} + \frac{\partial}{\partial x_i}u_i\rho = 0. \tag{1.30}$$

Momentum conservation $\chi = mv_i$
The momentum conservation equation is given by using $\chi = mv_i$ in Equation 1.28

$$\frac{\partial}{\partial t}(\rho u_i) + \frac{\partial}{\partial x_k}(\rho\langle v_iv_k\rangle) + \rho\frac{\partial\Phi}{\partial x_i} = 0 \tag{1.31}$$

with v_i the particle motion which is composed by the fluid motion u_i and the random velocity w_i

$$\langle v_iv_k\rangle = u_iu_k + \langle w_iw_k\rangle. \tag{1.32}$$

Dividing $\langle w_i w_k \rangle$ in a diagonally part and an a non diagonal part leads to

$$\rho \langle w_i w_k \rangle = P\delta_{ik} - \pi_{ik} \tag{1.33}$$

with δ_{ik} the Kronecker-Delta and defining the gas pressure P and the viscous stress tensor π_{ik}:

$$P := \rho \langle \frac{1}{3} |w|^2 \rangle, \tag{1.34}$$

$$\pi_{ik} := \rho \langle \frac{1}{3} |\mathbf{w}|^2 \delta_{ik} - w_i w_k \rangle. \tag{1.35}$$

Inserting Equation 1.32-1.35 into Equation 1.31 leads to

$$\frac{\partial}{\partial t}(\rho u_i) + \frac{\partial}{\partial x_k}\left(\rho u_i u_k + P\delta_{ik} - \pi_{ik}\right) = -\rho \frac{\partial \Phi}{\partial x_i}. \tag{1.36}$$

Energy conservation $\chi = m|\mathbf{v}|^2/2$
$\chi = m|\mathbf{v}|^2/2$ is used in Equation 1.28 to constrain energy conservation

$$\frac{\partial}{\partial t}\rho e + \frac{\partial}{\partial x_k}\left[\frac{\rho}{2}\langle (u_k + w_k)(u_i + w_i)^2 \rangle\right] + \rho \frac{\partial \Phi}{\partial x_k} u_k = 0. \tag{1.37}$$

Every average value including a single w is zeros since it is a random movement distributed in all directions. Unfolding the second term leads to:

$$\langle (u_k + w_k)(u_i + w_i)^2 \rangle = |\mathbf{u}|^2 u_k + 2u_i \langle w_i w_k \rangle + u_k \langle |\mathbf{w}|^2 \rangle + \langle w_k |\mathbf{w}|^2 \rangle. \tag{1.38}$$

Defining F_k as the conduction heat flux

$$F_k = \rho \langle w_k \frac{1}{2} |\mathbf{w}|^2 \rangle \tag{1.39}$$

leads to

$$\frac{\partial}{\partial t}\rho e + \frac{\partial}{\partial x_k}\left[\rho e u_k + u_k P - u_i \pi_{ik} + F_k\right] = -\rho u_k \frac{\partial \Phi}{\partial x_k}. \tag{1.40}$$

Closure condition
Altogether the conservation laws lead to five independent equations: mass conservation (Equation 1.30), energy conservation (Equation 1.40) and three components of momentum conservation (Equation 1.36). However, there are thirteen free variables describing the system. Thus, additional constraints have to be made. Allowing only elastic scattering the particle distribution function follows the Maxwellian one:

$$f_0 = n \left(\frac{m}{2\pi k T}\right)^{3/2} \exp\left(\frac{-m|w|^2}{2kT}\right). \tag{1.41}$$

Together with $\pi_{ik}^0 = F_i^0 = 0$ this constitutes the first-order approximation and the Euler equations follow:

$$\frac{\partial \rho}{\partial t} + \nabla \cdot (\rho \mathbf{u}) = 0, \tag{1.42}$$

$$\frac{\partial}{\partial t}(\rho \mathbf{u}) + \nabla(\rho \mathbf{u} \otimes \mathbf{u} + P I_3) = -\rho \nabla \Phi, \tag{1.43}$$

$$\frac{\partial}{\partial t}\rho e + \nabla\left[\rho e \mathbf{u} + \mathbf{u} P\right] = -\rho \mathbf{u} \nabla \Phi, \tag{1.44}$$

with I_3 the identity matrix. The Euler equations belong to the class of hyperbolic partial differential equations, which means that with given initial values and boundary conditions they can be solved at any time describing the evolution of the given system. Neglecting the external forces, as the gravitational potential, they can be rewritten to:

$$\frac{\partial}{\partial t}\mathbf{U} + \nabla \mathbf{F} = 0, \tag{1.45}$$

with $\mathbf{U}$ given by Equation 1.29 and

$$\mathbf{F} \equiv \begin{pmatrix} \rho \mathbf{u} \\ \rho \mathbf{u} \otimes \mathbf{u} + P I_3 \\ \rho e \mathbf{u} + \mathbf{u} P \end{pmatrix}. \tag{1.46}$$

1.3.2 Grid codes

Grid codes subdivide the simulation volume into voxels, each carrying the defining parameters density, velocity, and pressure. At each cell interface, the Euler equations are solved with the boundary conditions provided by the surrounding cells. An example of such a code is RAMSES, a Fortran code developed by Teyssier (2002), which was used in this thesis. In the following, I will discuss how grid codes work in more detail, by describing the Gudonov solver, the Riemann problem and the adaptive mesh refinement.

Gudonov solver

The Gudonov scheme solves Equation 1.45 with initial conditions and boundary conditions. For simplicity, we will here discuss the method for a 1D setup following Toro (1999) which is scaled to a 3D version for the simulations done in this thesis.

Consider discretising certain initial conditions, such as density, velocity, and energy given by $\mathbf{U}$ to a one-dimensional grid along x_i, by averaging over each cell:

$$\mathbf{U}_i^n = \frac{1}{\Delta x} \int_{x_{i-1/2}}^{x_{i+1/2}} \tilde{\mathbf{U}}\left(x, t^n\right) \mathrm{d}x, \tag{1.47}$$

where n is the corresponding evolved timestep. A schematic drawing is given in Figure 1.9 for cell x_i and its two neighbouring cells. The dark blue line indicates the cell average of $\mathbf{U}_i$. Using linear approximations in each cell instead of the constant average leads to a better interpolation of the underlying quantities, reducing numerical diffusion. This is the second-order extension which was used in this work, the Monotonic Upstream-Centered Scheme for conservation laws (MUSCL) introduced by van Leer (1979):

$$\mathbf{U}_i(x) = \mathbf{U}_i^n + \frac{(x - x_i)}{\Delta x}\Delta_i, \tag{1.48}$$

where Δ_i is a chosen slope, indicated by the light blue lines in Figure 1.9 and an example slope is given by

$$\Delta_i = \frac{1}{2}(1+\omega)(\mathbf{U}_i - \mathbf{U}_{i-1}) + \frac{1}{2}(1-\omega)(\mathbf{U}_{i+1} - \mathbf{U}_i), \tag{1.49}$$

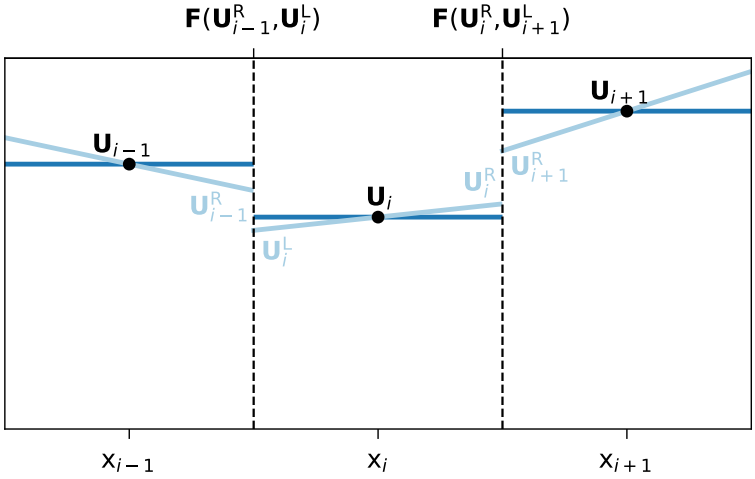

Figure 1.9: Schematic drawing of a 1D grid for cell i and its neighbouring cells, each having quantities $\mathbf{U}$. The cell boundaries are indicated by the black dashed line. The dark blue line shows the cell average, whereas the light blue line indicates linear approximations. With the Gudonov solver, $\mathbf{U}_i$ can be determined for the next time step.

with $\omega \in [-1, 1]$. To suppress high values of Δ_i slope limiters are used (in this thesis the monotonized central-difference slope limiter was used van Leer, 1979). This gradient then changes the values of $\mathbf{U}$ at the cell boundary indicated by the indices L-left and R-right. Now the discontinuities between the cells have to be solved. For piecewise constant configuration a Riemann solver is used (more details in the paragraph below). Thus, we have to determine average values for the piecewise linear interpolation:

$$\bar{\mathbf{U}}^{\mathrm{L}}_i = \mathbf{U}^{\mathrm{L}}_i + \frac{1}{2}\frac{\Delta t}{\Delta x}\left[\mathbf{F}(\mathbf{U}^{\mathrm{L}}_i) - \mathbf{F}(\mathbf{U}^{\mathrm{R}}_i)\right], \tag{1.50}$$

$$\bar{\mathbf{U}}^{\mathrm{R}}_i = \mathbf{U}^{\mathrm{R}}_i + \frac{1}{2}\frac{\Delta t}{\Delta x}\left[\mathbf{F}(\mathbf{U}^{\mathrm{L}}_i) - \mathbf{F}(\mathbf{U}^{\mathrm{R}}_i)\right]. \tag{1.51}$$

Now with this configuration a Riemann solver can be used to determine the values for the next time step:

$$\mathbf{U}^{n+1}_i = \mathbf{U}^{n}_i + \frac{\Delta t}{\Delta x}\left[\mathbf{F}^{hllc}_{i-1/2} - \mathbf{F}^{hllc}_{i+1/2}\right]. \tag{1.52}$$

$\mathbf{F}^{hllc}_{i\pm1/2}$ is the solution to the Riemann problem at the cell boundary, discussed in the following.

Riemann problem

A Riemann problem is the discontinuity induced by discretising an initial value problem governed by conservation equations, as for example the problem above (this paragraph follows Toro, 1999). There are different solvers available for exact solutions or approximations. The chosen solver in this thesis was the HLLC approximate Riemann solver (Toro et al., 1994). This solver distinguishes between three different waves, the fastest, the slowest and the middle wave indicated by $S_{\mathrm{R}}, S_{\mathrm{L}}, S_*$, expanding from the cell boundary. The limits are determined by subtracting, or adding the maximal sound speed c_{s}:

$$S_{\mathrm{L}} = \min\{u_{x,\mathrm{L}}, u_{x,\mathrm{R}}\} - \max\{c_{\mathrm{s,L}}, c_{\mathrm{s,R}}\}, \tag{1.53}$$

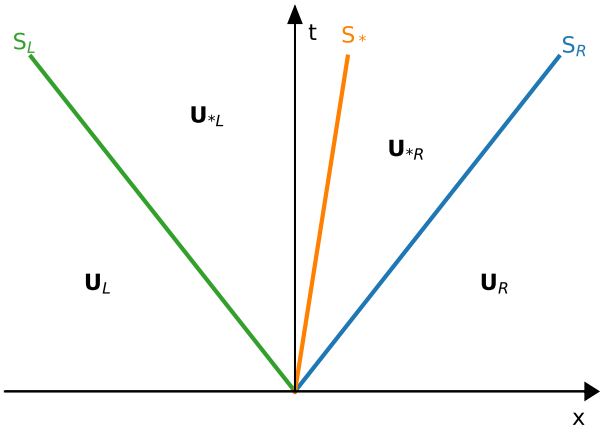

Figure 1.10: The different wave speeds S_L, S_*, and S_R as a function of time (y-axis) starting off at the cell boundary $x = 0$. Depending on the location of the cell boundary $x/t = 0$ in comparison to the travelling waves, $\mathbf{U}$ is calculated differently.

$$S_\mathrm{R} = \max\{u_{x,\mathrm{L}}, u_{x,\mathrm{R}}\} + \max\{c_{\mathrm{s.L}}, c_{\mathrm{s,R}}\}. \tag{1.54}$$

Whereas the middle wave is given according to Batten et al. (1997) by:

$$S_* = \frac{P_\mathrm{R} - P_\mathrm{L} + \rho_\mathrm{L} u_{x,\mathrm{L}}(S_\mathrm{L} - u_{x,\mathrm{L}}) - \rho_\mathrm{R} u_{x,\mathrm{R}}(S_\mathrm{R} - u_{x,\mathrm{R}})}{\rho_\mathrm{L}(S_\mathrm{L} - u_{x,\mathrm{L}}) - \rho_\mathrm{R}(S_\mathrm{R} - u_{x,\mathrm{R}})}. \tag{1.55}$$

A schematic illustration is given in Figure 1.10. It shows the spatial extension on the x-axis and the time on the y-axis, $x = 0$ is the boundary with the discontinuity. Here, R and L refer to the right and left sides of the boundary. Depending on the location of the cell boundary ($x/t = 0$) in reference to the waves different values for $\mathbf{U}$ are chosen as indicated in the graphic. The flux at the boundary is then selected depending on the direction of the travelling waves:

$$\mathbf{F}^{hllc}_{i+1/2} = \begin{cases} \mathbf{F}_\mathrm{L} & \text{for } 0 \leq S_\mathrm{L} \\ \mathbf{F}_{*\mathrm{L}} = \mathbf{F}_\mathrm{L} + S_\mathrm{L}(\mathbf{U}_{*\mathrm{L}} - \mathbf{U}_\mathrm{L}) & \text{for } S_\mathrm{L} \leq 0 \leq S_* \\ \mathbf{F}_{*\mathrm{R}} = \mathbf{F}_\mathrm{R} + S_\mathrm{R}(\mathbf{U}_{*\mathrm{R}} - \mathbf{U}_\mathrm{R}) & \text{for } S_* \leq 0 \leq S_\mathrm{R} \\ \mathbf{F}_\mathrm{R} & \text{for } 0 \geq S_\mathrm{R} \end{cases} \tag{1.56}$$

Adaptive mesh refinement

In Astrophysical simulations, the phenomenon one wants to investigate is often on a much smaller scale than the simulation volume. Therefore, using a uniform grid with the necessary spatial resolution is often computationally too expensive or even not feasible. To circumvent this, adaptive mesh refinement (AMR) can be used (Berger & Oliger, 1984; Berger & Colella, 1989). The idea is to only refine the grid in the area of interest and simulate the other parts with a lower resolution. There are different methods available for the refinement, for example, refining certain cells or whole blocks. For the cell-by-cell

approach, one starts off with a grid of the lowest resolution subdividing all cells that fulfil the refinement criterion. This criterion can be diverse, in this thesis we used a density cut. Thus, all cells above a certain density get refined, such that the filament and its cores are better resolved than the surrounding medium. Refinement means halving the box in each direction, which refers to subdividing the cell into eight cells in 3D. This process can be repeated recursively, leading to several refinement levels. Hence, each level leads to an increase in resolution by two. In RAMSES a 'tree-based AMR' is used referring to the employed data structure. It works similarly, giving some additional constraints on the refinement of neighbouring cells to induce a smooth transition between levels (for more details see Teyssier, 2002). During the simulation, the refinement criterion is tracked to adjust the grid during every timestep due to the change in density distribution. This makes it possible to simulate several orders of magnitude in one simulation.

Figure 1.11: Patch of the ORION nebula. The filamentary structure inside is much more complex than the usual cylindrical one. Tuning fork-like split-ups can be observed. (Picture credit: ESO/H. Drass/ALMA (ESO/NAOJ/NRAO)/A. Hacar, CC BY 4.0)

1.4 Structure of the thesis

Observations of the interstellar medium show much more complex structures than the theoretically assumed cylindrical-shaped filaments. A good example is given in Figure 1.11 where you see the Orion star-forming region. Several filaments, e. g. the one at the left border of the image, show a characteristic tuning fork-shaped split-up. One explanation of such a structure is the merging of two isolated cylindrical filaments. In Chapter 2 I will discuss under which conditions filaments can merge since the merger has to be faster than the overall collapse of the filament. In the follow-up Paper (Chapter 5) we find that these tuning fork-like structures can indeed be created by the merger of filaments and some indications of merges are found in the observations of LDN 1641-North in the star-forming region Orion.

The lifetime of a filament is not only a constraining parameter in our studies about the merging of filaments but also for their evolution and fragmentation. Since there is no hydrostatic solution for the main axis of a filament, all filaments are in the process of collapsing. In Chapter 3 I show how isolated filaments collapse and present a model to describe this process, which explains the collapse time of filaments found empirically by Clarke & Whitworth (2015).

As already described in Section 1.2.2 the collapse of a filament induces the edge effect. It is a long-debated topic in the community since the edge effect is expected by theory but rarely observed. Fragmentation happens more often inside the filament than at the edges. In Chapter 4 I show that a certain density gradient at the end can slow down the edge effect significantly such that perturbations can grow faster.

Finally, I will give an outlook on an example of using machine learning to speed up hydrodynamic simulations. For simulating the heating and cooling correctly, a chemical network is needed. This depends significantly on the attenuation of UV irradiation from outside. One of the computationally expensive steps is the calculation of these attenuation factors. In the summer project (Chapter 6) I did at the Flat Iron Institute (New York City, USA), we set up a neural network to determine the attenuation factors for a given density distribution. The algorithm captures the overall structures well and the next step would be to improve the description of small scales and the high-density structures.

Chapter 2

Paper I – Merging filaments I: A race against collapse

Elena Hoemann, Stefan Heigl and Andreas Burkert, 2021, *Monthly Notices of the Royal Astronomical Society*, 507, 3486-3494

The interstellar medium is characterised by an intricate filamentary network which exhibits complex structures. These show a variety of different shapes (e. g. junctions, rings, etc.) deviating strongly from the usually assumed cylindrical shape. A possible formation mechanism are filament mergers which we analyse in this study. Indeed, the proximity of filaments in networks suggests mergers to be rather likely. As the merger has to be faster than the end dominated collapse of the filament along its major axis we expect three possible results: (a) The filaments collapse before a merger can happen, (b) the merged filamentary complex shows already signs of cores at the edges or (c) the filaments merge into a structure which is not end-dominated. We develop an analytic formula for the merging and core-formation timescale at the edge and validate our model via hydrodynamical simulations with the adaptive-mesh-refinement-code RAMSES. This allows us to predict the outcome of a filament merger, given different initial conditions which are the initial distance and the respective line-masses of each filament as well as their relative velocities.

Keywords: stars:formation – ISM:kinematics and dynamics – ISM:structure

2.1 Introduction

The cold interstellar medium (ISM) is characterised by elongated cylindrical density enhancements, known as filaments. Filaments are observed over many different scales, from $> 100\,\mathrm{pc}$ length like in Nessie (Goodman et al., 2014; Mattern et al., 2018), over other infrared dark clouds (IRDC) (Perault et al., 1996; Alves et al., 1998; Egan et al., 1998; Hennebelle et al., 2001; Peretto & Fuller, 2009; Miettinen & Harju, 2010), down to the current detection limits of order of (sub-)pc scales (Molinari et al., 2010; Arzoumanian et al., 2011; Hacar et al., 2013; Schmiedeke et al., 2021). However, a clear understanding of their formation, evolution and collapse still remains an open question, although it has been known that they are a key step in the star formation process.

Initial studies already revealed a close connection between filamentary structure and star formation (Schneider & Elmegreen, 1979). Moreover, due to the Herschel dust observations (André et al., 2010, 2014; Arzoumanian et al., 2019) combined with ground based molecular line observations (Hacar & Tafalla, 2011; Kainulainen et al., 2016; Yuan et al., 2020) a much broader picture could be manifested in the last years. For example, most prestellar cores are found in supercritical filaments (Könyves et al., 2015; André et al., 2010) despite the fact that cores could also form by fragmentation of subcritical structures (Nagasawa, 1987; Fischera & Martin, 2012; Heigl et al., 2016; Gritschneder et al., 2017; Chira et al., 2018).

In low density environments, like in Taurus (Hacar et al., 2013), as well as inside dense regions, e. g.in Orion (Hacar et al., 2018), small fialmentary substructure was observed insdie the large filaments. Thus, Tafalla & Hacar (2015) proposed a formation mechanism called 'fray and fragment'. The large filamentary structure is created due to an encounter of two gas fronts. Inside the filament velocity coherent structures form, which they called 'fibers' these were also shown to be forming in turbulent, self-gravitating simulations (Moeckel & Burkert, 2015; Clarke et al., 2017). However, Smith et al. (2014) also see fibers perpendicular to a filament, thus they proposed that these are not a product of filament fragmentation but rather accreted from the surrounding gas. Either way, this results in a dense filamentary network in which stars are supposed to form. The close proximity suggests that interactions between the fibers/filaments could occur and impact the further evolution of the region.

In addition, observations show much more complex structures than the normally considered cylindrical shaped filaments. For example, in the substructure of the Orion integral filament, Hacar et al. (2018) found networks of small scale filaments where a common pattern appears to be the tuning-fork shape. These filaments reveal a split up of the single string into two components. Furthermore, even more complex configurations can be found, as e. g. ring-like objects (closed filaments). The origin of these geometrical shapes could be related to the dynamics of the interstellar gas which is then of major importance for the physics of fragmentation and thus the early phase of stellar formation.

A scenario of tuning fork formation from an elliptical sheet in the context of the Orion A cloud has been proposed by Hartmann & Burkert (2007). However, we explore a different formation mechanism: The merging of two cylindrical shaped filaments originally in hydrostatic equilibrium. It is an important mechanism to increase the density of a filament significantly and eventually trigger star formation. The fact, that in some observations multiple velocity components were detected inside a single filament (Hacar

et al., 2013; Yuan et al., 2020) could be a remnant of our scenario, as the filaments involved can retrain information about the merger in their intrinsic velocity field. Both Nakamura et al. (2014) (Serpens South) and Frau et al. (2015) (Pipe Nebula) have indeed detected signatures of colliding filaments and Fukui et al. (2021) stated that cloud-cloud collisions should lead to subsequent filament mergers. Nevertheless, theoretical work on the conditions of such a merger is currently very limited.

However, the collapse timescale along the main axis of a filament limits the possibility of filament merging. Filaments collapse by the so called 'edge effect' (Bastien, 1983). Because the acceleration at the edges of the filaments is strongest (Burkert & Hartmann, 2004), matter is piled up and forms cores at the ends (see observations by e. g. Dewangan et al., 2019; Bhadari et al., 2020; Yuan et al., 2020; Cheng et al., 2021). These then move into the centre while accreting the material on the way inwards and finally, fusing into one core and destroying the filament. Considering the case of filament mergers, this results in two competing timescales: the collapsing timescale of a filament (Toalá et al., 2011; Pon et al., 2012; Clarke & Whitworth, 2015) versus the filament-filament merging timescale. A comparison of these two timescales enables us to determine under which conditions a filament can merge before the collapse destroys it. Since not all observed tuning-forks show signs of an end dominated collapse it is also interesting to investigate on which timescale cores could form at the ends, to get a more accurate idea of initial conditions required to form such structures. Thus, we explore analytic models for merging and edge effect formation timescales to explore the parameter space for merging filaments, initially in hydrostatic equilibrium.

This paper is organised as follows: After an overview over the basic principles which were applied in our analysis (Section 2.2), the simulation framework is introduced (Section 2.3). The main part of the work focuses on the calculation of the merging (Section 2.4) and edge effect formation timescales (Section 2.5), each validated by simulations, respectively. This leads to the initial conditions under which mergers can take place, discussed in Section 2.6. Finally, the results are discussed in Section 2.7 and conclusions are drawn in Section 2.8.

2.2 Basic Principles

We consider filaments to be isothermal gas cylinders in hydrostatic equilibrium, a model which has been investigated by Stodólkiewicz (1963) and Ostriker (1964). Both found that the radial profile follows:

$$\rho(r) = \rho_c \cdot \left[1 + \left(\frac{r}{H}\right)^2\right]^{-2} \tag{2.1}$$

H is the scale height, given by:

$$H^2 = \frac{2c_s^2}{\pi G \rho_c} \tag{2.2}$$

with ρ_c being the central density of the filament, c_s the sound speed which is $0.19\,\mathrm{km\,s^{-1}}$ for $T = 10\,\mathrm{K}$ and a mean molecular weight of 2.36 as in Fischera & Martin (2012). We constrain the radius by the external pressure of the ISM, as the observed filaments do

not extend to infinity (Fiege & Pudritz, 2000). This external pressure $P_{\rm ext}$ then sets the boundary density $\rho(R) = \rho_b$ of the filament such that it is in pressure equilibrium with the surrounding $P_{\rm ext} = P_b$ which gives the filament a finite radius.

A characterising quantity of the filament is the so called line-mass, the mass per length:

$$\mu = \frac{M}{L} \tag{2.3}$$

The solution with the largest stable line-mass is then given by integrating the Ostriker-profile until infinity. For even larger line-masses the filament will collapse due to gravity as no hydrostatic solutions exist. This is called the critical line-mass $\mu_{\rm crit}$. Considering the values mentioned above leads to:

$$\mu_{\rm crit} = \left(\frac{M}{L}\right)_{\rm crit} = \frac{2c_s^2}{G} \approx 16.4\,{\rm M}_\odot\,{\rm pc}^{-1} \tag{2.4}$$

To define the criticality of a filament, the parameter f was introduced (Fischera & Martin, 2012) as the ratio of the filament line-mass to the critical line-mass:

$$f = \frac{\mu}{\mu_{\rm crit}} \tag{2.5}$$

which allows to connect the central and boundary density:

$$\rho_b = \rho_c \cdot (1-f)^2 \tag{2.6}$$

Analogous the radius of the filament is given by:

$$R = H\left(\frac{f}{1-f}\right)^{1/2} \tag{2.7}$$

Considering now that filaments in the ISM have a finite length, they will collapse along their major axis under self-gravity, when there are no other external influences (Keto & Burkert, 2014). The acceleration along such a filament of uniform density ρ and length l was investigated by Burkert & Hartmann (2004) and is given by:

$$a = -2\pi G\rho\left[2z - \sqrt{\left(\frac{l}{2}+z\right)^2 + R^2} + \sqrt{\left(\frac{l}{2}-z\right)^2 + R^2}\right] \tag{2.8}$$

where z is the coordinate along the filaments main axis, with $z = 0$ at the symmetry point. The acceleration shows a strong increase at the filament's edges. This leads to end-dominated collapse and to core formation at the ends of the filament, the so called 'edge effect' which, finally, destroys the filament. The lifetime of a filament is then given by the time it takes to collapse into a single core. As already mentioned, there exist several investigations of this collapse timescale (Toalá et al., 2011; Pon et al., 2012), the latest by Clarke & Whitworth (2015), which is given by:

$$t_{\rm col} = \frac{0.49 + 0.26\,A}{\sqrt{G\rho}} \tag{2.9}$$

Here, $A = l/(2R)$ is the aspect ratio and ρ its average density $\mu/(\pi R^2)$.

2.3 Simulation Setup

We also compare our analytic approach to simulations which were executed using the adaptive-mesh-refinement code RAMSES, developed by Teyssier (2002). It solves the Euler Equations in their conservative form by using a second-order Gudonov solver. We applied the MUSCL (Monotonic Upstream-Centered Scheme for Conservation Laws, van Leer, 1979), the HLLC-Solver (Harten-Lax-van Leer-Contact, Toro et al., 1994) and the MC slope limiter (monotonized central-difference, van Leer, 1979). The grid applied in our simulations varied from level 7, $(128)^3$ cells (4.7×10^{-3} pc - 11.7×10^{-3} pc depending on the box size), to level 9, $(512)^3$ cells (1.2×10^{-3} pc - 2.9×10^{-3} pc), such that the external medium is only resolved with low resolution while the filament itself is resolved with the highest one. As an example, a simulation as performed for Section 2.4 has a resolution of 44 cells along the filaments diameter at its highest contraction and above 100 for its initial configuration. In order to resolve the hydrodynamical processes the filaments were resolved with a minimum of ~ 20 cells.

Two different types of simulations were carried out to verify the merging and edge effect formation timescales. The initial physical conditions used in each case are described in the corresponding section. Nevertheless, all simulations were carried out in the same environment, which means with the same boundary density of $\rho_b = 1.92\times10^{-20}\,\mathrm{g\,cm^{-3}}$ which equals 4.9×10^3 particles per cm^3, a rather high value to recreate a surrounding as in Orion. Given f this also sets the central density via Equation 2.6. This resembles the situation where all filaments are embedded in the same surrounding medium, constrained by the same outside pressure. However, tests showed that variations in the external pressure does not have a major influence on the result of the simulation. The external density was set to $\rho_{\mathrm{ext}} = 3.92\times10^{-23}\,\mathrm{g\,cm^{-3}}$, in pressure equilibrium to the filament, in order to minimise accretion effects and to ensure that the relative velocities of filaments are subsonic with respect to the external medium.

2.4 Merging timescale

In this section the merging process of two filaments is described in detail. This includes the calculation of the merging timescale and the determination of the trajectory.

In order to derive the merging timescale, two infinite filaments with according line-masses of μ_1 and μ_2 are considered to be in a parallel configuration of initial distance d_0, as depicted in Figure 2.1 in the first snapshot.

The relative gravitational acceleration on both filaments respectively is given by

$$a_G = -\left(\mu_1 + \mu_2\right)\frac{2G}{d} \tag{2.10}$$

which results in the following relative velocity, with v_0 being the initial relative velocity of the filaments:

$$v = -\sqrt{4G\left(\mu_1 + \mu_2\right)\log\left(\frac{d_0}{d}\right) + v_0^2} \tag{2.11}$$

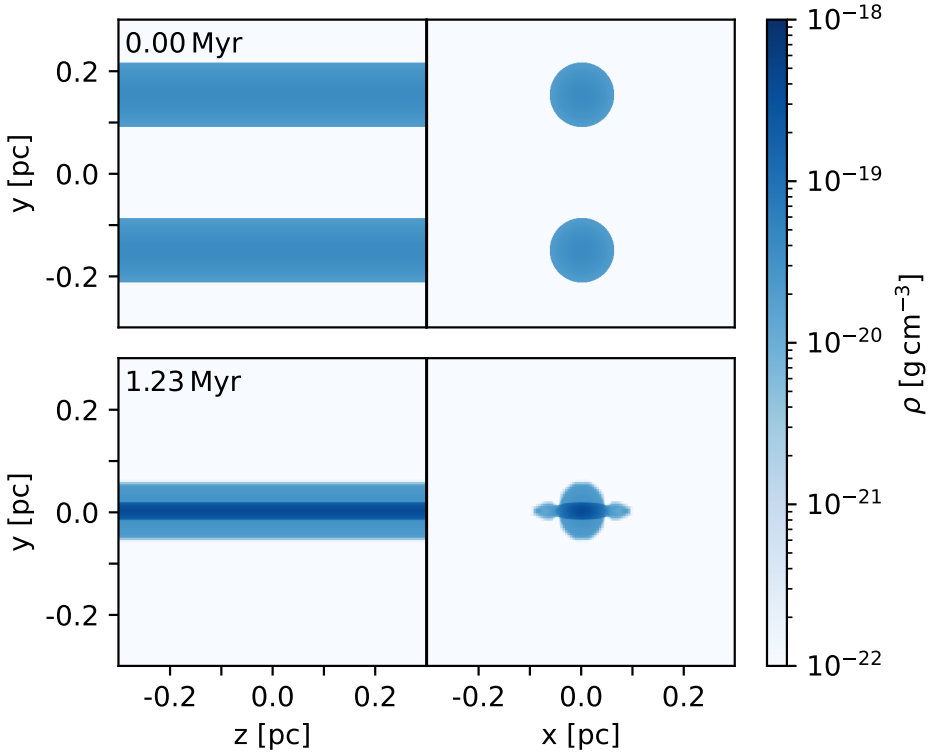

Figure 2.1: Density slices of a 'standard' simulation done in this work $f_1 = f_2 = 0.3$ of merging filaments. In the first row the initial condition ($t = 0.00\,\mathrm{Myr}$) and in the second row the time of final configuration ($t = 1.23\,\mathrm{Myr}$) is displayed. The left hand side shows the the filament elongated in z direction and initially separated in y direction (z/y). On the right hand side the slice is given in x/y-direction to see the whole dimensionality of the simulation.

Integration from the initial separation d_0 to d results in the time needed for the filaments to reach the distance d (derivation in Appendix 2.8):

$$t = \sqrt{\frac{\pi}{G(\mu_1+\mu_2)}} \cdot \frac{d_0}{2} \cdot \exp\left(\frac{v_0^2}{4G(\mu_1+\mu_2)}\right) \cdot \left[\mathrm{erf}\left(\sqrt{\log\left(\frac{d_0}{d}\right) + \frac{v_0^2}{4G(\mu_1+\mu_2)}}\right) - \mathrm{erf}\left(\frac{v_0}{\sqrt{4G(\mu_1+\mu_2)}}\right)\right] \tag{2.12}$$

with $\mathrm{erf}(x)$ being the Gauss error function. In the limit of d approaching zero, which means that the filaments overlap completely, the merging time can be approximated:

$$\begin{aligned} t_{\mathrm{merge}} &= \lim_{d\to 0} t \\ &= \sqrt{\frac{\pi}{G(\mu_1+\mu_2)}} \cdot \frac{d_0}{2} \cdot \exp\left(\frac{v_0^2}{4G(\mu_1+\mu_2)}\right) \\ &\quad \cdot \left[1 - \mathrm{erf}\left(\frac{v_0}{\sqrt{4G(\mu_1+\mu_2)}}\right)\right] \end{aligned} \tag{2.13}$$

If the filaments are initially at rest, $v_0 = 0$, the merging time reduces to:

$$t_{\text{merge}} = \sqrt{\frac{\pi}{G(\mu_1 + \mu_2)}} \cdot \frac{d_0}{2} \tag{2.14}$$

For $v_0 = 0$ the trajectory, distance of the filaments depending on time, is then given by solving Equation 2.12 for d:

$$d(t) = d_0 \cdot \exp\left[-\text{erfinv}\left(2\sqrt{\frac{G(\mu_1 + \mu_2)}{\pi}}\frac{t}{d_0}\right)^2\right] \tag{2.15}$$

with $\text{erfinv}(x)$ being the inverse error function.

In order to validate these results, we execute simulations of filament mergers with different line-masses and initial velocities. The simulation box has a scale of $(0.6\,\text{pc})^3$. The initial condition is given in Figure 2.1 in the first row: the left hand side shows a density slice in z-y direction and the right hand side a density slice in x-y direction, in order to display the full dimensionality. We present two points in time, the initial condition $t = 0.0\,\text{Myr}$ and the merged filaments, in this example $t = 1.23\,\text{Myr}$. The filaments have their major axis along the z-axis which has periodic boundary conditions in order to create an infinitely long filament. They are initially separated by $d_0 = 0.3\,\text{pc}$ in y-direction. The boundary in y and x direction were chosen to be open. During the simulation the two filaments fall into each others potential and merge. To exclude that accretion has major effects on the simulation we varied the external density ($\rho_{\text{ext}} = 3.92 \times 10^{-24}\,\text{g}\,\text{cm}^{-3}$) but no influences on the merger were observed.

A comparison of theoretical and simulated distance evolution of the two filaments for different merging constellations is given in Figure 2.2. The theoretical distance prediction is depicted in blue for different line-masses. In contrast, the black dots represent the distances obtained from simulations by determining the distance of the centre of mass of the two filaments. The gray dashed line indicates the time the filaments start to overlap. The simulations (black dots) show a very good agreement to the theoretically predicted values (blue line). The orange square represents the merging time determined from simulations, which should be compared to the zero point of the trajectories. The merging point of the simulation was considered to be the time where the merged filament recovers the radius of the initial filaments, in this case the two initial filaments totally overlap and share the same centre of mass ($d = 0$). For the merger with different line masses and thus different radius, we used the mean of the filaments radius instead. In all cases we get a good agreement between the model and the simulated values.

In order to confirm that the model correctly reproduces the merging time's velocity and line-mass dependence, we also performed a parameter study. The results are shown in Figure 2.3. The different coloured lines are the solutions to Equation 2.13 for different initial velocities. The symbols show the corresponding merging time of the simulation, which is in good agreement with the predictions. Both, the dependence on the summed line-mass, as well as on the initial relative velocity of the two filaments, v_0, are reproduced very well in our simulations.

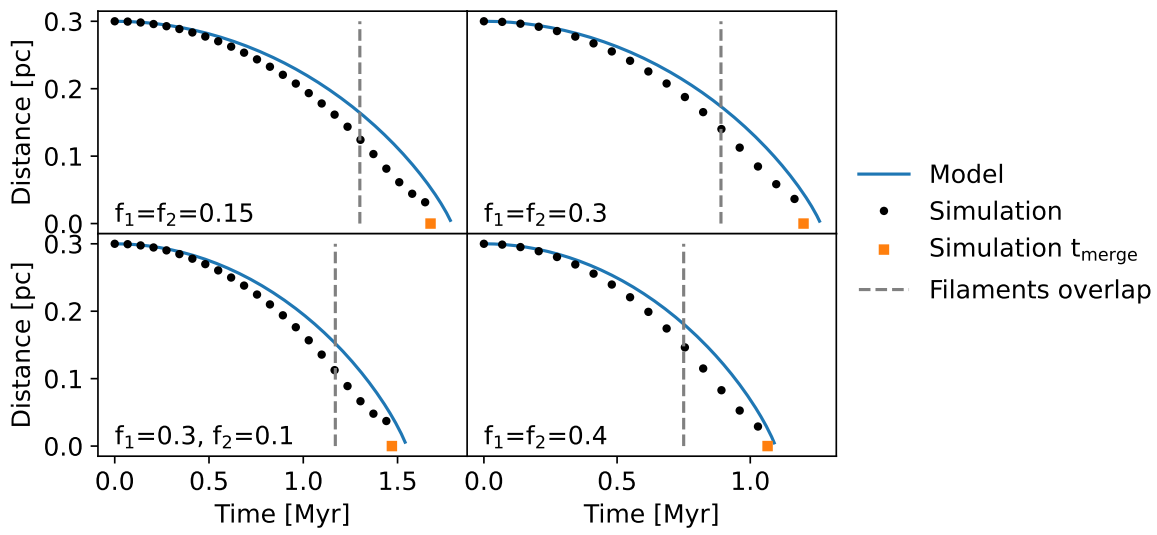

Figure 2.2: Validation of the trajectory of merging filaments with four different constellations of line-masses (f_1, f_2 are given in the bottom left corner). The blue curve shows the trajectory given by Equation 2.15, the black dots indicate the centre of mass distance of the filaments. The grey dashed line represents the moment when the filaments start to overlap. The orange square gives the simulation's merging time. Given the simplicity of the analytical approach we consider this a good agreement between the values from simulation (dots) and the model.

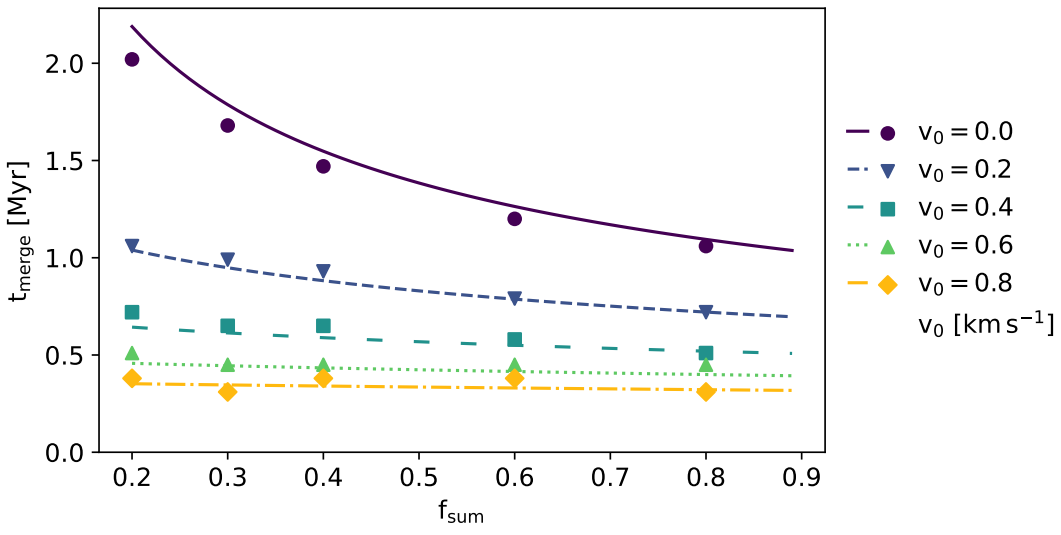

Figure 2.3: Validation of the merging timescale depending on the sum $f_{\mathrm{sum}} = f_1 + f_2$ (f being the critciality defined in Equation 2.5). The different coloured lines show Equation 2.13 for different converging initial velocities but fixed $d_0 = 0.3\,\mathrm{pc}$. The values from the simulation are displayed as symbols in the corresponding colour.

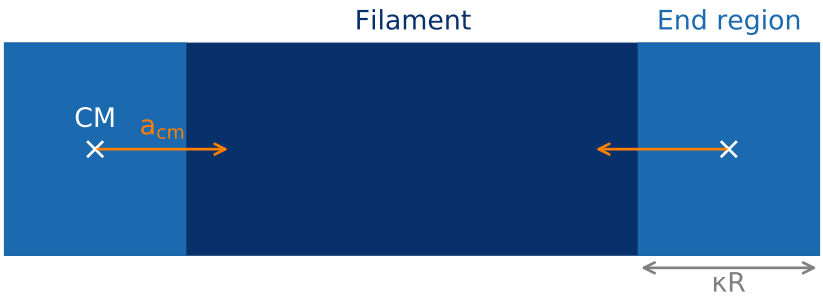

Figure 2.4: Schematic drawing of a face-on filament. With two end regions of size κR (light blue areas) which accumulate the mass. The centre of mass of the end regions is marked with white crosses. Here the acceleration $a_{\rm cm}$ is indicated by the orange arrow.

2.5 Edge effect formation timescale

If we consider now a more realistic setup with finite filaments a second effect comes into play: the gravitational collapse of the filaments along their major axis. This leads to the important question of which process is faster, the merger or the edge effect. The collapse time was already investigated by Clarke & Whitworth (2015) which we discussed in Section 2.2. However, as not all observed tuning-forks show signs of the edge effect we want to investigate on what timescale cores are formed at the edges which we will call the edge effect formation timescale $t_{\rm edge}$. This can give us constraints on the initial conditions of the merged filaments.

We consider the filament to have two end regions, similar to Yuan et al. (2020). A simple scheme is given in Figure 2.4 where these end regions are marked with light blue color. They are considered to be the zone where the end clump will evolve. The total acceleration of this region is approximated to be the acceleration of the end regions centre of mass (a_{CM}), indicated by the white cross with attached orange arrow depicting the acceleration. For the right edge, where the centre of mass is located at $z = \frac{l}{2} - \frac{\kappa R}{2}$, it is given by Equation 2.8, for $l \gg R$:

$$a_{\rm CM} \approx -\pi G \rho R \left(\sqrt{\kappa^2 + 4} - \kappa \right) \tag{2.16}$$

The constant value of their extension κR is afterwards fitted to the simulations. In case of a spherical end region one would expect its size to be $2R$, thus $\kappa = 2$. The acceleration can be considered as constant in time as long as $l \gg R$ holds, because the most time dependent parameter (length l) cancels out. We assume the end region to accumulate all the mass which it encounters during the collapse:

$$M(t) = M_0 + \frac{1}{2} a_{\rm CM} t^2 \cdot \mu_0 \tag{2.17}$$

This leads to the time dependent line-mass of the end region:

$$\mu(t) = \frac{\kappa R + \frac{1}{2} a_{\mathrm{CM}} t^2}{\kappa R} \cdot \mu_0 \tag{2.18}$$

The timescale of interest is the time needed for the end region to get supercritical:

$$f(t) = \frac{\mu(t)}{\mu_{\mathrm{crit}}} \stackrel{!}{=} 1 \tag{2.19}$$

with μ_{crit} the critical line-mass. From here we are able to calculate the timescale needed for the filament to accumulate supercritical end regions:

$$t_{\mathrm{edge,1.0}} = \sqrt{\left(\frac{1}{f} - 1\right) \frac{2\kappa R}{|a_{\mathrm{CM}}|}} \tag{2.20}$$

$$= \sqrt{\frac{(f-1)^2}{f} \cdot \frac{2}{\pi G \rho_b \left(\sqrt{1 + (2/\kappa)^2} - 1\right)}} \tag{2.21}$$

In the context of filament mergers, another interesting timescale is the time necessary for the edges to be above a criticality of $f = 0.5$. If there is a symmetrical merger the end regions of both filaments will overlap and thus if both end regions have a criticality of 0.5 they immediately become supercritical. The timescale in this case is given by:

$$t_{\mathrm{edge,0.5}} = \sqrt{\left(\frac{1}{f} - 2\right) \cdot \frac{1 - f}{\pi G \rho_b \left(\sqrt{1 + (2/\kappa)^2} - 1\right)}} \tag{2.22}$$

This simple approach does not consider ram pressure contributions from the gas inside the filament. Clarke & Whitworth (2015) showed that this effect was important when determining the overall collapse timescale of the filament. Following their semi-analytical model we found ram pressure to be only significant in the late stages of filament collapse and has only minor influences on the edge formation timescale. However for low mass filaments ($f \sim 0.1$), having long edge formation timescales, this could get essential. Thus, we excluded all filaments with $f < 0.2$ from our analysis.

In addition, we also validated our results with simulations. We set up a filament in a box with a size of 1.5 pc and open boundary conditions. Thus, the filaments had a finite length of approximately 1.3 pc. We used an exponential cutoff for the filaments edge following $[1 + \exp(-100 \cdot (0.4 - z^2))]^{-1}$. However, tests of different edges with sharp and soft cutoffs showed no influence on the simulated collapse time. The initial and final conditions are presented in Figure 2.5. The upper panel shows the density slices in z/y-direction at $t = 0$ and $t = t_{\mathrm{edge,1.0}}$ and the bottom panel depicts the corresponding line-mass dependency along the z-axis. In the beginning, the filament has a uniform criticality of $f = 0.3$ and we determine $t_{\mathrm{edge,1.0}}$ when the line-mass in the cores at the edge exceeds the limit of $f = 1.0$ for the first time, as shown in the dashed black line in Figure 2.5. From the figure, the large density and line-mass enhancements at the edges are obvious. The large volume of the box was chosen such that the condition $l \gg R$ holds. Therefore, the acceleration discussed in Section 2.2 can be considered constant. We set

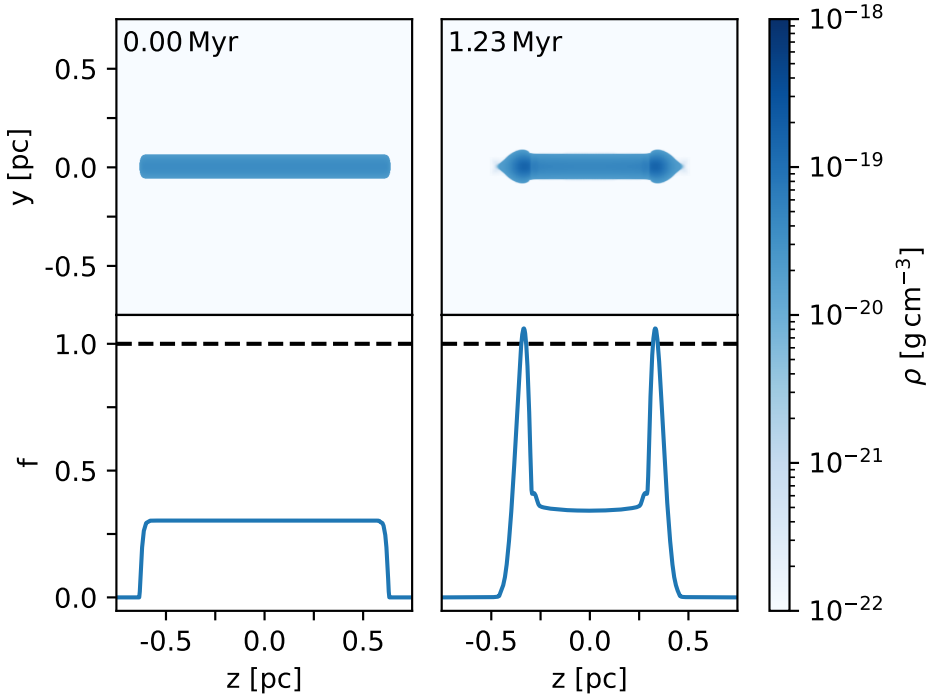

Figure 2.5: Top: Density slices of a 'standard' simulation with $f = 0.3$ to determine the edge formation timescale are presented in z-y direction. Bottom: The criticality (Eq. 2.5) of the filament along the z-axis is displayed. Left panel: The initial condition ($t = 0.00\,\mathrm{Myr}$) of the simulation. Right panel: A snapshot after 1.23 Myr where the cores reach a criticality above 1 and thus start to collapse.

a fixed boundary density of $\rho_b = 1.92 \times 10^{-20}\,\mathrm{g\,cm^{-3}}$ and adjusted the central density (Equation 2.6) as before. The external density was again set to $\rho_{\mathrm{ext}} = 3.92 \times 10^{-23}\,\mathrm{g\,cm^{-3}}$.

Figure 2.6 shows the theoretical models (lines) of the edge effect formation timescale depending on f in comparison to the values determined by our simulations (symbols). Model 0.5 (blue dashed line and squares) gives the timescale needed for a filament to form cores at the edges with core criticality $f = 0.5$. Model 1.0 (green solid line and dots) shows the timescale to grow cores with $f = 1.0$. The size of the end region κR was fitted to the simulation data and the parameters are provided in the legend of the plot. As expected the deviation from $\kappa = 2$ is small which considers a spherical end region. By inserting all constants (κ,G,π) and using Equation 2.6 we have found a simple empirical relation that fits these cases very well:

$$t_{\mathrm{edge,1.0}} = \sqrt{\frac{1.69 \times 10^{-20}\,\mathrm{g\,cm^{-3}}}{f\rho_c}}\,\mathrm{Myr} \tag{2.23}$$

Thus, the edge effect formation time only depends on the central density and the criticality of the filament. As Equation 2.23 agrees well with the simulations we will use it for the early collapse in order to constrain our initial conditions for a merger.

To compare the formation of the edges to the general core formation inside a filament due to perturbations the two timescales are depicted in Figure 2.7. Following the analysis done in Heigl et al. (2020) the time dependent criticality of an infinitely long filament

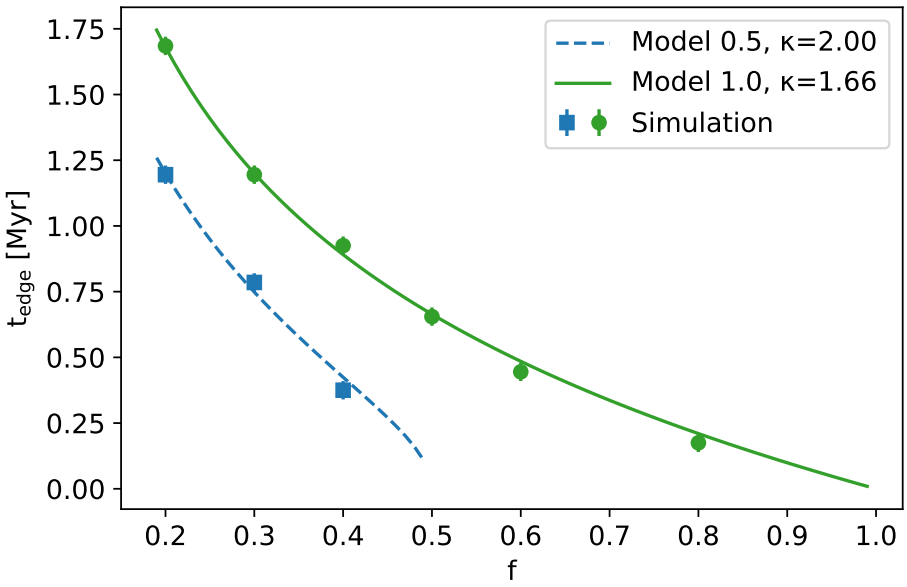

Figure 2.6: The edge effect formation timescale of the model as function of the initial f (lines, Eq. 2.5) in comparison to the simulation (symbols) is given. Green represents the model with maximum $f_{\max} = 1.0$ and blue $f_{\max} = 0.5$. The size of the corresponding end region κ is fitted to the simulation data, the fit values are given in the legend. Both models show excellent agreement to the simulation.

with perturbations of strength ϵ and growth timescale of the dominant mode τ_{dom} is given by:

$$f_{\max}(t) = f\left[1 + \epsilon \cdot \exp\left(\frac{t}{\tau_{\mathrm{dom}}}\right)\right] \stackrel{!}{=} 1 \tag{2.24}$$

Again, we consider a core to be formed for f reaching a value of 1 which leads to a core formation timescale due to perturbations of:

$$t_{\mathrm{pert}} = \tau_{\mathrm{dom}} \log\left[\left(\frac{1}{f} - 1\right)\frac{1}{\epsilon}\right] \tag{2.25}$$

The perturbation strength ϵ was set to 0.09 according to observations by Roy et al. (2015) and τ_{dom} was calculated using the fourth-order polynomial function presented in Fischera & Martin (2012) (Appendix E) based on Nagasawa (1987). Figure 2.7 show the resulting collapse timescale due to perturbations depending on the initial criticality as orange dashed line ($\epsilon = 0.09$, light orange shaded region shows $0.01 < \epsilon < 0.17$ as reference) and in comparison the timescale of the edge effect (Equation 2.20) as solid green line. Both timescales depend on the boundary density which was set to $\rho_b = 1.92 \times 10^{-20}\,\mathrm{g\,cm^{-3}}$, the same as in our simulations. Although the absolute timescale varies when changing ρ_b the trend stays the same: Below values of $f < 0.7$ the formation of the edge effect is faster than the core formation timescale, above perturbations could grow faster.

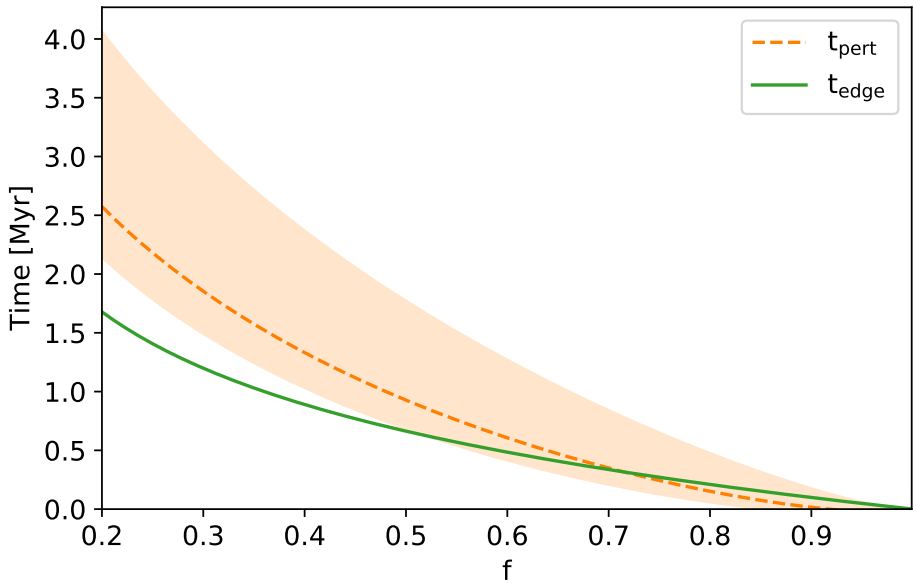

Figure 2.7: The core formation timescale (orange dashed line) for a perturbation strength of 0.09 (light orange shaded region $0.01 < \epsilon < 0.17$) depending on the initial line mass (Eq. 2.5) in comparison to the edge formation (green solid line). Both timescales depend on the boundary density $\rho_b = 1.92 \times 10^{-20}\,\mathrm{g\,cm^{-3}}$. But the plot is self-similar for different ρ_b. For $f < 0.7$ the edge effect is faster than perturbations grow inside the filament, for more massive filaments perturbations could form slightly before the edges start to collapse.

2.6 Parallel merger

2.6.1 Initial conditions

With the analytic formulation of the merging and edge effect timescales it is now possible to calculate the conditions for the merging of two filaments without a dominant 'edge effect'. In order to do so, we calculate the time difference between the merger (Equation 2.13) and the edge effect (Equation 2.23) as function of the sum $f_{\mathrm{sum}} = f_1 + f_2$ the initial distance and the initial velocity:

$$\Delta t = t_{\mathrm{edge},1.0} - t_{\mathrm{merger}} \tag{2.26}$$

The result is given in Figure 2.8. In the top panel Δt (colour scale) is given as function of distance and f_{sum}. Here, only $f_1 = f_2$ was considered. Otherwise, only the edge effect timescale of the heavier filament plays a role. In the lower panel it is given for $f_1 = f_2 = 0.3$ depending on distance and the initial velocity. The negative (red) values belong to the regime where the filament forms cores faster than it can merge. Below the white line, which indicates the point where the timescales are equal, a merger is possible before the filaments from cores (blue regime). The dashed blue line gives the timescale needed for the filaments to form overdensities with values of $f = 0.5$. Thus, the merged filament is immediately supercritical if these regions overlap. The merger of two filaments is limited by the grey dashed dotted line which is given by $t_{\mathrm{col}} = t_{\mathrm{merger}}$ (Equation 2.9, with a representative aspect ratio of $A = 8$) whereas the grey shaded region gives the

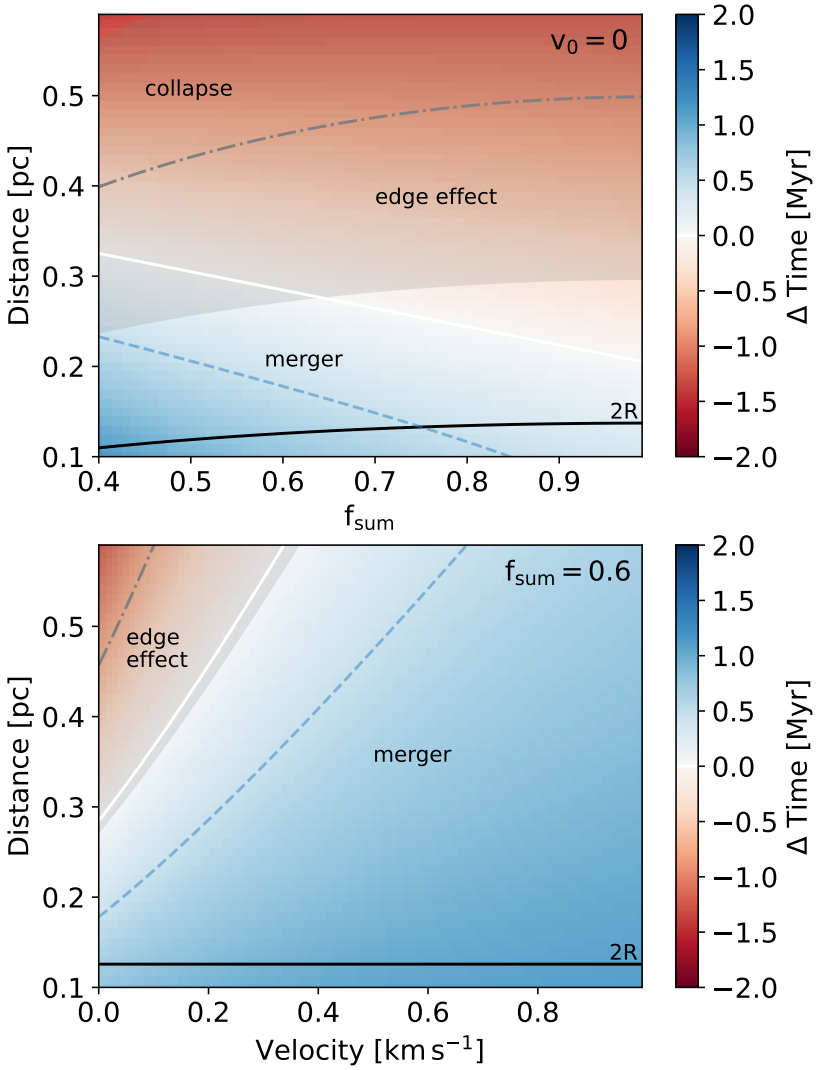

Figure 2.8: Time difference Δt (Equation 2.26) between merging and edge effect timescale for different initial conditions. The top panel shows the summed line-mass (Eq. 2.5) and distance of the two filaments (with $v_0 = 0$). The lower panel shows the distance and velocity for $f_{\mathrm{sum}} = 0.6$. The white line indicates the conditions where the merging time equals the core-formation time at the edges. The dashed blue line indicates the initial distance for which filaments have enough time to form over densities of $f = 0.5$ before merging. Thus, if the over-densities overlap supercritical regions are immediately created in the merged filament. The black line indicates two times the radius of the initial filament. Below this line filaments already overlap in the beginning. The region between the white and the black line (and more distinct the blue dashed line) give initial conditions where the filament merger is possible without forming supercritical regions. A converging initial velocity makes a mergers without supercritical densities more probable. The dashed dotted grey line gives the $t_{\mathrm{col}} = t_{\mathrm{merger}}$, Equation 2.9 (Clarke & Whitworth, 2015), with an aspect ratio of $A = 8$ (the grey shaded area gives the condition for $4 < A < 12$), above this we would expect a filament to collapse faster than it can merge.

times for $4 < A < 12$. Above this line the filament collapses faster than it can merge. Thus, no merger is possible in that regime. The black line indicates the size of two times the radius of the initial filament. Below these values the filaments are already overlapping initially. Therefore we are only interested in the area above. In summary, for a symmetric merger of initially resting filaments, filaments initially have to lie between the black and the dashed blue lines (for overlapping end regions) or solid white lines (for not overlapping end regions) in order to merge before collapse of the end cores which appears rather unlikely. In the lower panel Δt is depicted as function of velocity and distance for filaments of $f_1 = f_2 = 0.3$. In this case a much wider range of distances is allowed for filament mergers, as the window widens up with increasing velocity. This is also the case for other summed line-masses, as depicted in Appendix 2.8 for $f_{\mathrm{sum}} = 0.4$ and $f_{\mathrm{sum}} = 0.8$. In general, the influence of the initial velocity is much stronger for lighter than for more massive filaments. Nevertheless, having a convergent initial velocity makes a merger much more probable.

This shows that only symmetric filaments with certain initial conditions merge before the edge effect takes over: The distances between the filaments have to be small ($< 0.4\,\mathrm{pc}$) and their converging relative velocities have to be high ($> 0.3\,\mathrm{km\,s^{-1}}$). Conditions found among small scale filaments, as for example the sub-pc spacing is found in Taurus (Hacar et al., 2013) and relative velocities greater than $0.3\,\mathrm{km\,s^{-1}}$ in Orion (Hacar et al., 2018).

2.6.2 Simulation of parallel merges

By choosing the right initial conditions a merger without supercritical cores can be simulated. An example is given in Figure 2.9 where a lateral shift of the two filaments ensures that the edge regions do not overlap. The initial conditions are shown in the left panel as density slice (top) and criticality (bottom). The filaments have a critciality of $f = 0.2$ each, a relative velocity of $v_0 = 0.4\,\mathrm{km\,s^{-1}}$ and an initial distance of $d_0 = 0.2\,\mathrm{pc}$. Corresponding to Figure 2.10 (left hand side) the filaments should merge without forming supercritical regions which is what happens (see Figure 2.9 bottom right). Because of the shift, two density peaks seem to evolve at the points where the edge overlaps with the other filament which could be a mechanism to form cores away from the edge of the new filament. Additionally, due to the shift, angular momentum is injected into the system which could generate accretion discs. We will explore these processes in details in a subsequent paper.

2.7 Discussion

In this study we focused on the merging behavior of parallel aligned filaments. This is of course a special case which seems rather unlikely at first glance. Although the merging time was calculated for the parallel case, it should also give a good first approximation for inclined filaments.

We simulated isothermal filaments without feedback, turbulence and winds. This isolated scenario could be linked to a young and quiet surrounding. Nevertheless, investigations by Hacar et al. (2018) already showed that the large scale feedback has no significant influence on the statistical properties of the fibers/filaments in Orion when

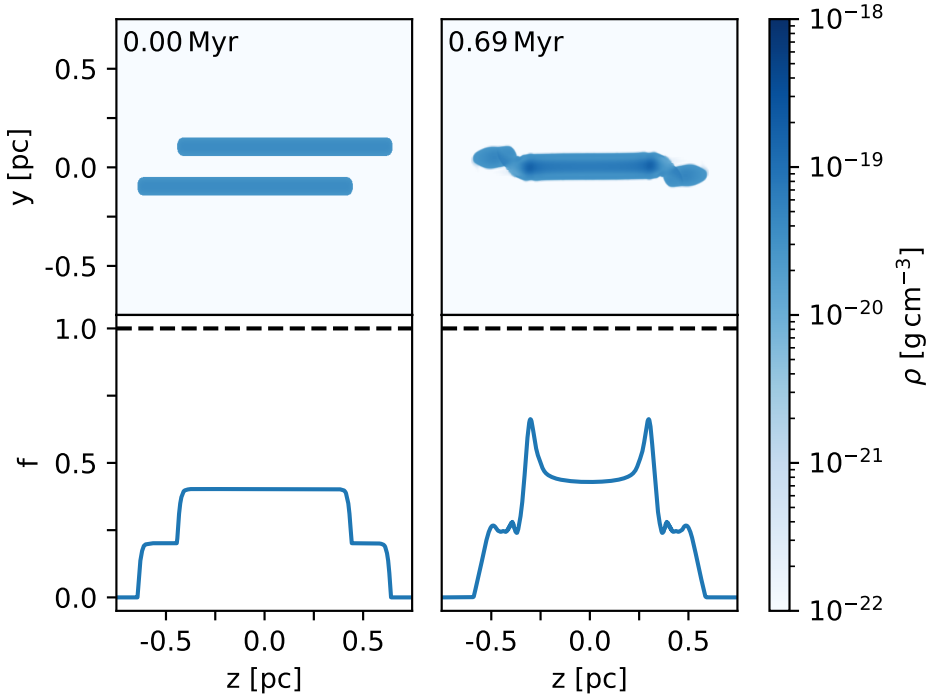

Figure 2.9: Same arrangement as in Figure 2.5. Two filaments with a critciallity (Eq. 2.5) of $f = 0.2$, $d_0 = 0.2\,\mathrm{pc}$ and $v_0 = 0.2\,\mathrm{km\,s^{-1}}$ are simulated with a translation along the z-axis. As expected they merge without creating supercritical regions.

comparing regions with low and high feedback. Thus, we do not expect large deviations for our model due to feedback.

We saw that the probability for filaments to merge is much higher for filaments with relative initial velocities. Hacar et al. (2013) already detected relative velocities up to $2.4\,\mathrm{km\,s^{-1}}$in filaments of L1495/B213. However, if the initial velocity of the filaments is not oriented along their connecting line but with an inclination α, too high velocities could lead to the escape of the filament out of the gravitational potential. The velocity necessary to escape the gravitational attraction is given by the escape velocity. For a configuration similar to the ones we simulated the escape velocity is of the order of $\sim 1\,\mathrm{km\,s^{-1}}$. Filaments with higher velocities will only merge if their trajectories cross which is only the case for small angles. This results in a rather low probability for filaments to merge with relative velocities higher than the escape velocity. Further investigations have to show what else constrains relative velocities of merging filaments. Furthermore, high relative velocities could also destroy the filaments in the process of the merger.

We limited the effects of accretion by simulating a low density environment. Accretion could affect both the merging and collapse timescale as it increases the filament line-mass, exerts a ram pressure and induces turbulence in the filaments (Clarke & Whitworth, 2015; Heigl et al., 2018, 2020).

The filaments were set-up as idealized cylinders with a constant line-mass. However, density gradients inside the filaments can influence the local merging timescale, according to Equation 2.13 the merging time is shorter for larger f. This effect can lead to even more complex structures. Imagine a density minimum in the center of the filaments

(along the z-axis): the ends of the filaments would merge first and ring like structures could from. Moreover, also the timescale and behavior of the edge effect would change since density enhancements are already present in the filament.

2.8 Conclusions

We provide an analytic model to describe both, the merger of filaments and the first phase of filament collapse due to the 'edge effect'. Simulations show that the used approximations are reasonable and fit the predictions well. To conclude, the main points are as follows:

As the timescale of merging and collapsing filaments are of the same order of magnitude, the initial conditions determine how the resulting structure would look like. Three different outcomes are possible: The resulting filament has no supercritical cores at the edges, the edge effect dominates the resulting structure or the filaments collapse entirely before they can merge. The outcome mostly depends on the initial velocity, the initial line-mass and the initial distance of the filaments. For high velocities ($> 0.3\,\mathrm{km\,s^{-1}}$) and small distances ($< 0.4\,\mathrm{pc}$) the probability for a symmetric filament merger is highest.

Acknowledgements

This research was supported by the Excellence Cluster ORIGINS which is funded by the Deutsche Forschungsgemeinschaft (DFG, German Research Foundation) under Germany's Excellence Strategy – EXC-2094 – 390783311. We thank the CAST group and especially Alvaro Hacar for helpful discussions and comments, Nir Mandelker for the help on the Ramses boundary conditions and the anonymous referee for the productive feedback.

Appendix

2.A Solving the velocity integral

To calculate the merging time the ODE $\frac{\mathrm{d}d}{\mathrm{d}t} = v$ (velocity is given by Equation 2.11) has to be solved, with initial condition $t_0 = 0$

$$t = -\int_{d_0}^{d} \frac{\mathrm{d}d'}{\sqrt{4G(\mu_1+\mu_2)\log\left(\frac{d_0}{d'}\right) + v_0^2}} \tag{2.27}$$

Substitution $u = \frac{d_0}{d'}$, $\frac{\mathrm{d}u}{\mathrm{d}d'} = -\frac{d_0}{d'^2} = -\frac{u^2}{d_0}$

$$t = \int_1^{d_0/d} \mathrm{d}u\, \frac{d_0}{u^2} \left(4G(\mu_1+\mu_2)\log(u) + v_o^2\right)^{-\frac{1}{2}} \tag{2.28}$$

Substitution $x = \sqrt{4G(\mu_1+\mu_2)\log(u) + v_0^2}$

$$\frac{\mathrm{d}x}{\mathrm{d}u} = \frac{2G(\mu_1+\mu_2)}{u\sqrt{4G(\mu_1+\mu_2)\log(u) + v_0^2}} \tag{2.29}$$

$$u = \exp\left(\frac{x^2 - v_0^2}{4G(\mu_1+\mu_2)}\right) \tag{2.30}$$

Inserting this, with $v_1 = \sqrt{4G(\mu_1+\mu_2)\log(\frac{d_0}{d}) + v_0^2}$:

$$t = \frac{d_0}{2G(\mu_1+\mu_2)} \int_{v_0}^{v_1} \mathrm{d}x \ \exp\left(-\frac{x^2 - v_0^2}{4G(\mu_1+\mu_2)}\right) \tag{2.31}$$

Substitution $h = \frac{x}{\sqrt{4G(\mu_1+\mu_2)}}$, $\frac{\mathrm{d}h}{\mathrm{d}x} = \frac{1}{\sqrt{4G(\mu_1+\mu_2)}}$

$$t = \frac{d_0}{\sqrt{G(\mu_1+\mu_2)}} \exp\left(\frac{v_0^2}{4G(\mu_1+\mu_2)}\right) \cdot \int_{v_0/\sqrt{4G(\mu_1+\mu_2)}}^{v_1/\sqrt{4G(\mu_1+\mu_2)}} \mathrm{d}h \ \exp\left(-h^2\right) \tag{2.32}$$

$$= \sqrt{\frac{\pi}{4G(\mu_1+\mu_2)}} d_0 \exp\left(\frac{v_0^2}{4G(\mu_1+\mu_2)}\right) \left[\mathrm{erf}\left(\frac{\sqrt{4G(\mu_1+\mu_2)\log\left(\frac{d_0}{d}\right) + v_0^2}}{\sqrt{4G(\mu_1+\mu_2)}}\right) - \mathrm{erf}\left(\frac{v_0}{\sqrt{4G(\mu_1+\mu_2)}}\right)\right] \tag{2.33}$$

Finally, the time it takes to get from d_0 to a certain d is given by (which is the resulting Equation 2.12):

$$t = \sqrt{\frac{\pi}{G(\mu_1+\mu_2)}} \cdot \frac{d_0}{2} \cdot \exp\left(\frac{v_0^2}{4G(\mu_1+\mu_2)}\right) \cdot \left[\mathrm{erf}\left(\sqrt{\log\left(\frac{d_0}{d}\right) + \frac{v_0^2}{4G(\mu_1+\mu_2)}}\right) - \mathrm{erf}\left(\frac{v_0}{\sqrt{4G(\mu_1+\mu_2)}}\right)\right] \tag{2.34}$$

2.B Initial conditions for filament mergers depending on velocity

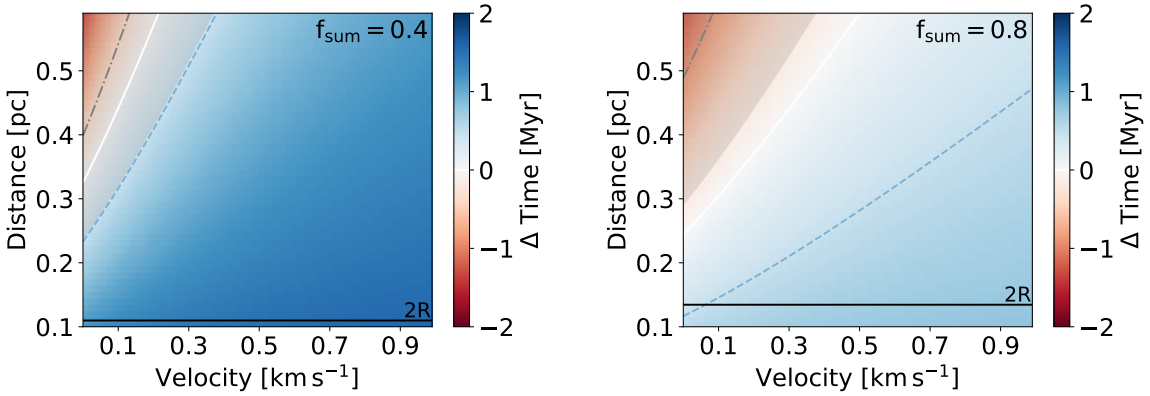

Figure 2.10: Δt as defined in Equation 2.26 depending on diastance and velocity for different cirtialities $f_{\mathrm{sum}} = 0.4$ and $f_{\mathrm{sum}} = 0.8$ (a more detailed description is given in Figure 2.8). This shows that in both cases an initial velocity makes a merger more probable. Though, the influence on the lower line mass filament is stronger.

Chapter 3

Paper II – Filament collapse: A two phase process

Elena Hoemann, Stefan Heigl and Andreas Burkert, 2023, *Monthly Notices of the Royal Astronomical Society*, 521, 5152–5159

Using numerical simulations, we investigate the gravitational evolution of filamentary molecular cloud structures and their condensation into dense protostellar cores. One possible process is the so called 'edge effect', the pile-up of matter at the end of the filament due to self-gravity. This effect is predicted by theory but only rarely observed. To get a better understanding of the underlying processes we used a simple analytic approach to describe the collapse and the corresponding collapse time. We identify a model of two distinct phases: The first phase is free fall dominated, due to the self-gravity of the filament. In the second phase, after the turning point, the collapse is balanced by the ram pressure, produced by the inside material of the filament, which leads to a constant collapse velocity. This approach reproduces the established collapse time of uniform density filaments and agrees well with our hydrodynamic simulations. In addition, we investigate the influence of different radial density profiles on the collapse. We find that the deviations compared to the uniform filament are less than 10%. Therefore, the analytic collapse model of the uniform density filament is an excellent general approach.

Keywords: stars:formation – ISM:kinematics and dynamics – ISM:structure

3.1 Introduction

Observations show that the interstellar medium (ISM) is dominated by filamentary structure. Filaments are the cylindrical and cold density enhancements of the molecular ISM. They have been found in very different environments from large scales (more than 100 pc) like infrared dark clouds (Goodman et al., 2014; Mattern et al., 2018) down to small, (sub-) parsec scales (Molinari et al., 2010; André et al., 2010; Hacar et al., 2013; Schmiedeke et al., 2021) at the current detection limit. It is well established that filaments in the ISM are the places where star-formation happens (Schneider & Elmegreen, 1979), since most of the prestellar cores are found within these dense, cold environment (Arzoumanian et al., 2011; Könyves et al., 2015). However, there remain many open questions about their creation, evolution and fragmentation.

A particular example is the so called 'edge effect'(Bastien, 1983): The acceleration along a finite filament due to its self-gravity has a strong increase at its edges because of its elongated structure (Burkert & Hartmann, 2004; Hartmann & Burkert, 2007; Li et al., 2016). Thus, the collapse leads to a pile-up of matter in the end regions. This effect has been studied theoretically (Rouleau & Bastien, 1990; Arcoragi et al., 1991; Bastien et al., 1991; Hanawa et al., 1994) and has been detected in several observational studies (e.g. Zernickel et al., 2013; Kainulainen et al., 2016; Dewangan et al., 2019; Bhadari et al., 2020; Yuan et al., 2020; Cheng et al., 2021). Since there is no hydrostatic solution for the end of a long filament which could prevent the edge effect, it is expected to occur quite often. In contrast, Seifried & Walch (2015) showed that filaments with an initial inner density enhancement collapse centrally. A similar setup was investigated by Keto & Burkert (2014) for short filaments with axis ratio of 3:1. They find that the resulting core shows complex pattern of sonic oscillations. Although, such density distributions are not observed in low line-mass filaments (Roy et al., 2015), the oscillations in cores have been detected (Redman et al., 2006; Aguti et al., 2007). In addition, there has been a recent study by Heigl et al. (2021) where the edge effect is suppressed in a filament forming in a colliding flow, however, not every filament shows signs of accretion. Thus, the edge effect is expected to happen much more often than it is detected.

Understanding the edge effect is crucial for setting a limit for filament lifetimes because the collapse timescale is given by the time on which the two end regions collapse into a single point. Collapse times have been calculated by Toalá et al. (2011); Pon et al. (2012) and Clarke & Whitworth (2015). However, they all rely on the acceleration of uniform density filaments as calculated by Burkert & Hartmann (2004), a density profile which is neither observed nor theoretically expected.

The aim of this study is to get a more accurate impression of the longitudinal collapse of a filament and its corresponding collapse timescale. Therefore, we present an analytical model to calculate the evolution of the collapse and to explain the collapse timescale found in Clarke & Whitworth (2015). We used a simple approach consisting of two phases: an accelerated one, dominated by gravitational free fall, which turns into a collapse with constant velocity at the point where ram pressure sets in. Additionally, the influences of the filament's radial profile are analyzed, which has only minor contributions. Thus, the two phase model of collapse and force equilibrium for a uniform density filament can be used in general to determine collapse timescales of observed filaments.

The paper is organized as follows: After introducing the basic principles of filaments

in hydrostatic equilibrium (Section 3.2), the theoretical background of the edge effect is introduced (Section 3.3). The simulation is discussed in Section 3.4. In Section 3.5 the two phase collapse model of a uniform density filament is derived and in Section 3.6 we show a comparison of different profiles and their influence on the collapse time. The results are discussed in Section 3.7 and conclusions are drawn in Section 3.8.

3.2 Filaments in hydrostatic equilibrium

Following Stodólkiewicz (1963) and Ostriker (1964) a filament in hydrostatic equilibrium has the following radial density distribution:

$$\rho(r) = \rho_c \left[1 + \left(\frac{r}{H}\right)^2\right]^{-2} \tag{3.1}$$

with ρ_c being the central density. H is the scale height, given by

$$H^2 = \frac{2c_\mathrm{s}^2}{\pi G \rho_c}, \tag{3.2}$$

G being the gravitational constant and c_s the sound speed ($0.19\,\mathrm{km\,s^{-1}}$ for a temperature of 10 K and a mean molecular weight of 2.36, compare Fischera & Martin, 2012). Filaments in the ISM do not extend until infinity since they are constrained by an external pressure P_ext. This cuts off the filament at pressure equilibrium between the boundary pressure P_b and the external pressure $P_\mathrm{b} = P_\mathrm{ext}$ at density ρ_b. Its line-mass is given by

$$\mu = \frac{M}{l} \tag{3.3}$$

the mass M divided by the filaments length l. Integrating the hydrostatic profile until infinity gives the maximal line-mass for which a hydrostatic solution of the density profile exists and above which filaments collapse radially (Fischera & Martin, 2012). The critical value for $T = 10\,\mathrm{K}$ is

$$\mu_\mathrm{crit} = \frac{2c_\mathrm{s}^2}{G} \approx 16.4\,\mathrm{M_\odot\,pc^{-1}}. \tag{3.4}$$

The criticality is then given by the fraction of the actual line-mass to critical line-mass:

$$f = \frac{\mu}{\mu_\mathrm{crit}}. \tag{3.5}$$

Thus, a filament is considered supercritical when it exceeds $f = 1$ where no hydrodynamic solution can be found and the filament would start to collapse radially. Together with the central density the cirticality determines the boundary density

$$\rho_\mathrm{b} = \rho_\mathrm{c}(1 - f)^2 \tag{3.6}$$

and the corresponding filament radius R

$$R = H \left(\frac{f}{1-f}\right)^{1/2}. \tag{3.7}$$

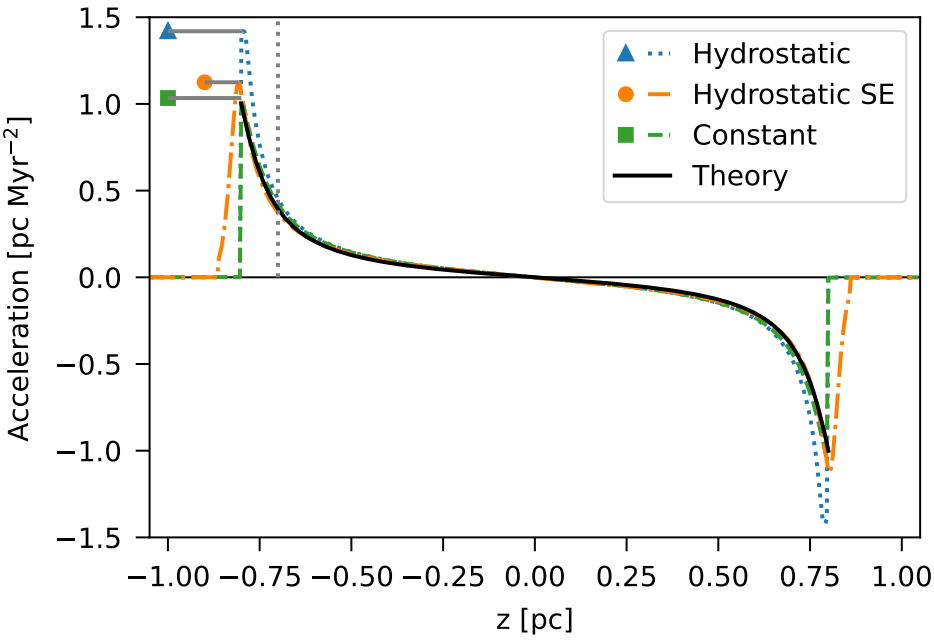

Figure 3.1: Acceleration along a filament with $A = 8$, $R = 0.10\,\mathrm{pc}$, $f = 0.7$ at its radial centre $r = 0$. The black line shows the analytical solution of a uniform density filament given by Equation 3.8 (Burkert & Hartmann, 2004). The coloured lines show the numerical determined accelerations for various density profiles: The constant density filament is given in dashed-green, the hydrostatic filament in dotted-blue, and the hydrostatic filament with soft edges hydrostatic SE (Equation 3.10) in dashed-dotted orange. At the end of the filament the acceleration is profile dependent and thus, deviates from the theoretical prediction. However, inside the filament and especially at the approximated center of mass of the end region (marked by the grey dotted line) the theoretical approximation fits well for all profiles.

3.3 Edge effect

Although there exists a hydrostatic solution for the radial profile of a filament (as discussed in Section 3.2), for the z-direction there are only solutions for elongated cores (Lizano & Shu, 1989; Tomisaka, 1991; Cai & Taam, 2010). This means there is no hydrostatic solution for the main axis of a filament with a considerable large aspect ratio $A = l/(2R)$. Thus, there is no possible profile for which the filament's end is stable. Therefore, it is expected that every isolated filament with finite length should collapse along its axis. The acceleration along the z-axis of a cylindrical filament with uniform density distribution (at r=0) was already investigated by Burkert & Hartmann (2004)

$$a = -2\pi G\bar{\rho}\left[2z - \sqrt{\left(\frac{l}{2}+z\right)^2 + R^2} + \sqrt{\left(\frac{l}{2}-z\right)^2 + R^2}\right], \tag{3.8}$$

with $\bar{\rho}$ being the uniform density and z being the position along the filament. An example of the acceleration is given by the black solid line in Figure 3.1. The steep increase in acceleration leads to a pile-up of matter in clumps forming at the ends of the filament. These move inward and finally merge in the center. This end dominated

collapse is what is called the 'edge effect' (Bastien, 1983). Of course the two end points can collapse gravitationally when they reach their local Jeans mass. In this case however, the protostellar cores will continue to move inwards until stellar feedback will become active. We do not model the effects of stellar feedback as it is beyond the scope of this paper and concentrate on the primary effect of gravitational collapse. Here we focus on the motion along the z-axis neglecting the compression by self-gravity in the x-y plane. We however explore different density structures in the x-y plane and demonstrate that the evolution in the z-direction is to first approximation independent of this detail. The acceleration at the exact end of the filament for $L \gg R$ can be approximated by:

$$a = \pm 2\pi G \bar{\rho} R. \tag{3.9}$$

This shows that the acceleration at the end of a filament is independent of its length.

In Figure 3.1 the acceleration for different profiles, measured in the simulations, is also depicted in comparison to the theoretical expectation. The acceleration of a constant density filament is shown in green, which matches the theoretical expected values. The hydrostatic filament, given by the blue dotted line, experiences a similar acceleration inside the filament. However, the maximum acceleration at the exact end of the filament is larger, as indicated by the grey horizontal line, marked with the blue triangle. The filament has a sharp cut at the end to match the cut-off of the uniform density filament. However, more soft edges (orange), defined as

$$\rho_{\rm end}(r, z) = \rho(r) \mathrm{sech}\left(2\frac{|z| - l/2}{H}\right)^2 \tag{3.10}$$

for $|z| > l/2$, had only minor influences, besides lowering the acceleration at the exact end. The grey dotted line is situated one radius away from the end inside the filament, which was used in Hoemann et al. (2021) as centre of mass of the end region. At this position the variations are negligible for all three cases.

As already mentioned, there is no hydrostatic solution for a cylinder with a finite length and considerably large aspect ratio, thus it is theoretically expected that every cylindrical filament should experience the edge effect. Although there are some observations of the edge effect (Zernickel et al., 2013; Kainulainen et al., 2016; Dewangan et al., 2019; Bhadari et al., 2020; Yuan et al., 2020; Cheng et al., 2021), in most cases no overdensities are detected at the end of filaments. This leads to a big puzzle: What suppresses the edge effect? A possible scenario is presented in Heigl et al. (2021) where the filament is formed by a constant radial accretion and the end regions are continuously fed with new material. Therefore, no real edge effect occurs. Nonetheless, an accretion flow is only detected seldom. It also has been shown that density fluctuations in the centre can lead to a central collapse mode (Seifried & Walch, 2015). However, the fluctuations need to be rather large, about a factor of three, which is normally not detected (Roy et al., 2015). Whether the edge effect is likely to be observed depends on its timescale. As in the case of filaments with small axis ratios, the collapse happens so fast that one hardly observes this phase. The complex, long-wavelength sonic oscillations of protostellar cores could then be the only detectable signature of this collapse phase (Keto & Burkert, 2014). This and the question whether one can prevent the edge effect requires a more detailed understanding of filament collapse which is the aim of this study.

We already demonstrated in an earlier work (Hoemann et al., 2021) that the timescale of the edge effect is dominated by the filament's criticality and its central density. This is the time needed to form self-gravitating cores, defined as a local over-density with $f > 1$, at the edge of a filament:

$$t_{\rm edge} = \sqrt{\frac{1.69 \times 10^{-20} \mathrm{g\,cm^{-3}}}{f \rho_{\rm c}}}\,\mathrm{Myr}. \tag{3.11}$$

In order to describe the overall collapse time, i.e. the time when the two end regions merge, several different approaches have been made: Toalá et al. (2011); Pon et al. (2012); Clarke & Whitworth (2015). The most recent one by Clarke & Whitworth (2015) found a description of the collapse time for long filaments fitting SPH simulations:

$$t_{\rm col} = \frac{0.49 + 0.26A}{\sqrt{G\bar{\rho}}} \tag{3.12}$$

where A represents the aspect ratio $A \equiv l/(2R) \gtrsim 2$. They also found that the core reaches a terminal velocity after about 1 Myr of acceleration due to ram pressure. The detected terminal velocities showed nearly no dependence on the aspect ratio.

However, a detailed analytic derivation of the collapse time (Equation 3.12) has not yet been achieved.

3.4 Simulating the filament collapse

In order to validate our analytic study, we performed hydrodynamic simulations with the adaptive-mesh-refinement code RAMSES (Teyssier, 2002). The Euler equations are solved in their conservative form by using a second-order Gudonov solver. We utilized the MUSCL (Monotonic Upstream-Centered Scheme for Conservation Laws, van Leer, 1979), the HLLC-Solver (Harten-Lax-van Leer-Contact, Toro et al., 1994) and the MC slope limiter (monotonized central-difference, van Leer, 1979).

We simulated filaments with different density profiles, characterized by their aspect ratio A (length divided by twice the radius), their radius R and their criticality f. We used a grid refinement between level 7 (128^3 cells) and level 9 (512^3 cells) with open boundary conditions. Since the boxes were chosen to be 0.5 pc bigger than the inserted filament, we had a resolution outside the filament (low refinement) of 3.90×10^{-2} pc - 1.02×10^{-2} pc and inside (high refinement) from 9.8×10^{-3} pc to 2.5×10^{-3} pc. The outside density was set to $\rho_{\rm ext} = 3.92 \times 10^{-23}\,\mathrm{g\,cm^{-3}}$(equivalent to 10 particles per $\mathrm{cm^3}$) in pressure equilibrium to the boundary of the filament, to have no influence of accretion effects. Because we are only interested in the longitudinal collapse and want to suppress radial contributions, radial velocities were set to zero (see Section 3.5 for further discussion).

An example simulation is shown in Figure 3.2 (upper panel) with a radius of $R = 0.05$ pc, a criticality of $f = 0.5$ and an aspect ratio of $A = 12$. The time evolution of the length can be traced by two values: distance between two peaks in the line-mass distribution (location of the end clump, 'Peak', dashed line) or the actual end of the filament where the line-mass drops below a third of the initial value ('Edge', dotted line), as indicated in the subplot of the filament at $t = 0.48$ Myr. The mean is given by the red dots, whereas the coloured area depicts the range between 'Edge' and 'Peak'.

Surprisingly, the position of the core (dashed line in the upper panel of Figure 3.2) follows a rather linear trend which is caught up by the outer end (small dotted line) over time. This indicates that there are two distinct phases in the collapse of a filament. The first part can be interpreted as a free fall as explored in Hoemann et al. (2021) which defines the epoch of formation of edge cores, namely that the edge cores become supercritical. At some point the acceleration is counterbalanced by the ram pressure experienced by the edge and a uniform movement sets in, which was already observed by Clarke & Whitworth (2015) in their Figure 4a. This is also the trend seen in our simulation, see Figure 3.2 lower panel. There, green dots represent the gravitational force and the orange squares show the force due to ram pressure. The gravitational force is calculated by the gravitational acceleration output from the simulation and the mass of the end clump, whereas the ram pressure force was estimated by $\Delta v^2 \rho S$ for a each cell with S being the face area of the cell in this case, Δv the velocity difference between neighbouring cells and ρ the density in the given cell. The arrows show the deviation within 15 cells ahead of the core, the square represents the highest value and the end of the arrow the average. Although the determination of the ram pressure is uncertain, which is depicted by the large arrow, the graph supports the idea of a two phase collapse.

With the equilibrium of forces a simple model can be established describing the collapse of a filament in two phases, given in the following section.

3.5 Collapse of a uniform density filament

Consider the simple case of a uniform density filament, where the acceleration along the main axis is well described by Equation 3.8. A simple approach can be used to calculate the collapse of a filament.

During the filament collapse the end core accumulates the swept up mass and, thus the mass increase of the core can be determined by

$$\frac{\mathrm{d}M}{\mathrm{dt}} = \rho S v \tag{3.13}$$

with M the mass of the core, ρ the density, S the face area of the core and v its velocity (here we assume that the swept up gas is at rest). The core's equation of motion is governed by the gravitational self-acceleration at the filament's end which we denote as a:

$$\frac{\mathrm{d}(Mv)}{\mathrm{dt}} = Ma \tag{3.14}$$

using the product rule we get to

$$v\frac{\mathrm{d}M}{\mathrm{dt}} + M\frac{\mathrm{d}v}{\mathrm{dt}} = Ma. \tag{3.15}$$

Using the mass increase defined above:

$$M\frac{\mathrm{d}v}{\mathrm{dt}} + \rho S v^2 = Ma. \tag{3.16}$$

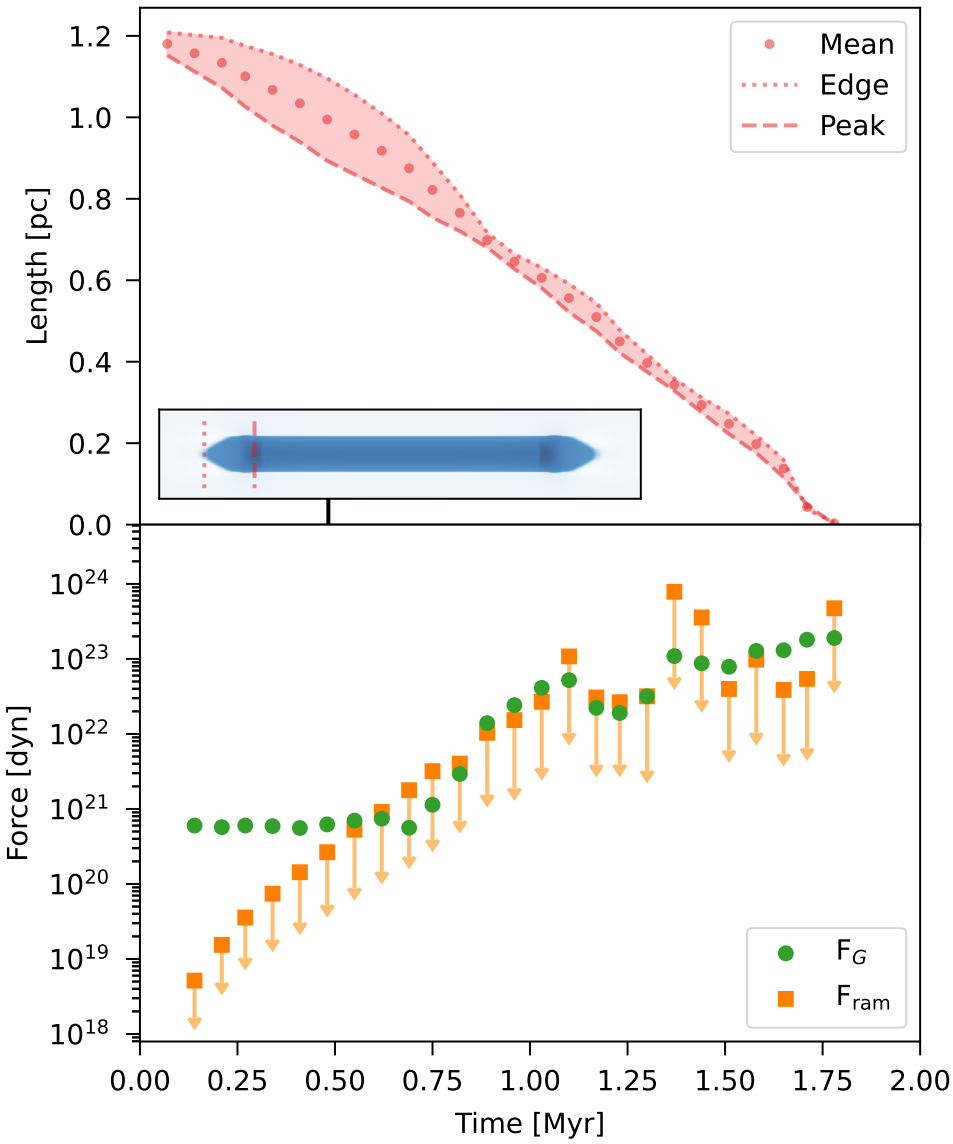

Figure 3.2: Length and force evolution of a hydrostatic filament with $A = 12$, $R = 0.05\,\mathrm{pc}$, $f = 0.5$.
Upper panel: The dotted red line depicts the evolution of the edge (where the line-mass decreases by a factor of three). The dashed red line follows the density peak. The mean is given by the red dots. The two positions are depicted by the small snapshot of the simulation in the left lower corner at $t = 0.48\,\mathrm{Myr}$. In the following plots the outer lines (dotted, dashed) are only represented by the shaded region.
Lower panel: The gravitational force, that the core experiences, is shown by the green dots, and the ram pressure acting against the collapse, is depicted as orange squares. First, the collapse is dominated by the gravitational force, which is counterbalanced by the ram pressure later on. The determination of the ram pressure is difficult in that case. Thus, the marker depicts the highest ram pressure value and the end of the arrow the mean value in the direct surrounding of the filament.

Already Clarke & Whitworth (2015) saw that a terminal velocity is reached after a certain time and also our simulations show a linear collapse in the later stages. Thus, the collapse is divided into two parts: the accelerated part, where only the gravitational self-acceleration of the filament plays a role and the phase where the force equilibrium sets in and the core experiences a constant velocity. We assume the transition between the two phases to occur on a short time scale so that it can be described as a sharp phase transformation at turning time t_{turn} where $\mathrm{d}v/\mathrm{dt} \approx 0$, which leads to:

$$\rho S v^2 \approx Ma \tag{3.17}$$

This results in a proportionality between the ram pressure force on the left hand side and the gravitational force on the right hand side

$$F_{\mathrm{ram}} \propto F_{\mathrm{G}} \tag{3.18}$$

after the turning time. This seems reasonable, since Figure 3.2 shows the correlation between gravity and ram pressure after the turning time.

Since the gravitational acceleration a at the edge (Equation 3.8) is independent of its length, a constant acceleration can be used. Thus, at the turning time t_{turn} the core has reached a velocity of $v = at_{\mathrm{turn}}$. Considering that the gas inside the filament is nearly at rest, while being swept up, this is exactly the velocity difference which produces the ram pressure after t_{turn}. Assuming that the density ratio between the swept up material and the core is always similar at force equilibrium leads to

$$(at_{\mathrm{turn}})^2 S\bar{\rho} \propto aSz\bar{\rho} \tag{3.19}$$

$$\Rightarrow \qquad t_{\mathrm{turn}} \propto \sqrt{\frac{z}{a}} \tag{3.20}$$

with z the size of the end region, which should be close to $2R$ assuming a symmetrical end region, and S the face area of a slice of the filament. Using this and κ as constant of proportionality, which is fitted to the simulation afterwards, results in:

$$t_{turn} = \kappa\sqrt{\frac{2R}{a}}. \tag{3.21}$$

The acceleration is given by Equation 3.8. Assuming that the end region is nearly symmetric the acceleration should be determined at $a\left(-\frac{l_0}{2} + \frac{z}{2}\right)$ (l_0 being the initial length of the filament), analogous to the determination of t_{edge} in Hoemann et al. (2021):

$$a\left(-\frac{l_0}{2} + \frac{z}{2}\right) = \alpha 2\pi G\bar{\rho}R \tag{3.22}$$

with α being a constant which also will be fitted to the simulation afterwards.

Now, the time evolution of the length of the filament can be given by

$$l(t) = \begin{cases} l_0 - at^2 & \text{for } t < t_{\mathrm{turn}} \\ l_0 + at_{\mathrm{turn}}^2 - 2at_{\mathrm{turn}}t & \text{for } t \geq t_{\mathrm{turn}} \end{cases} \tag{3.23}$$

and the collapse time is defined as $l(t) = 0$:

$$t_{\rm col} = \frac{l_0}{2at_{\rm turn}} + \frac{1}{2}t_{\rm turn} \tag{3.24}$$

$$= \left(\frac{l_0}{2R\kappa} + \kappa\right) / \sqrt{\alpha 4\pi G\bar{\rho}}. \tag{3.25}$$

Using the aspect ratio A, given by $A = l_0/(2R)$, leads to

$$t_{\rm col} = \left(\frac{1}{\kappa}A + \kappa\right) / \sqrt{\alpha 4\pi G\bar{\rho}}. \tag{3.26}$$

This is then the collapse time of a uniform density filament assuming the two phase model.

In order to validate our approach and to fit κ and α we performed hydrodynamic simulations as described in Section 3.4. The influence of the different density profiles will be discussed in the next section, however, the collapse time agreed within 10% between the simulations with uniform density and hydrostatic filaments. Since the hydrostatic profile is more realistic we used it in the following analysis. Furthermore, we suppressed radial motions to prevent the filament to collapse radially because here we want to study the longitudinal collapse independently, influences are discussed in the next paragraph. The simulated filaments are defined by the aspect ratio A, the radius R and the criticality f. The parameter space was covered as follows $f \in \{0.3, 0.5, 0.7\}$, $A \in \{8, 12, 15\}$, $R \in \{0.05\,\mathrm{pc}, 0.10\,\mathrm{pc}, 0.15\,\mathrm{pc}\}$. We limited the simulations to those which were collapsed after a runtime of 4 Myr which is on the order of estimated filament lifetimes of a few Myr (André et al., 2014). Besides, we did simulations with $f \in \{0.1, 0.9\}$ but they sometimes show a different behavior than the other filaments, as for low line-mass filaments the edge cores accelerate to the centre faster then the real edge and thus a second pair of edge cores evolves and for large line-mass filaments material is swept up in the center which leads to an additional central core (also seen in Seifried & Walch, 2015). We thus had in total 17 simulations for evaluation, displayed in Figure 3.3. The filament was considered as collapsed when the two density peaks merged and the aspect ratio of the filaments fell below 1. Each panel shows one of the parameters varied in the simulations on the x-axis and the collapse time on the y-axis. The second and third parameter are then plotted in different colours and styles, as indicated by the legends. The marker represent the simulated values. The lines show the fitted model. For clarity, not all simulations are plotted in one image. The model fits the simulated values very well for all configurations, with $\kappa = 1.22$ and $\alpha = 0.69$. The collapse time is then given by:

$$t_{\rm col} = \frac{0.42 + 0.28A}{\sqrt{G\bar{\rho}}} \tag{3.27}$$

$$= \frac{0.74R + 0.25l_0}{\sqrt{G\mu}}. \tag{3.28}$$

Besides small changes in the fitting factors this simple approach is also in agreement and explains Equation 3.12 by Clarke & Whitworth (2015).

Since we wanted to study the collapse along the main axis of the filament, the radial velocity was artificially set to zero to prevent the radial collapse. This was especially

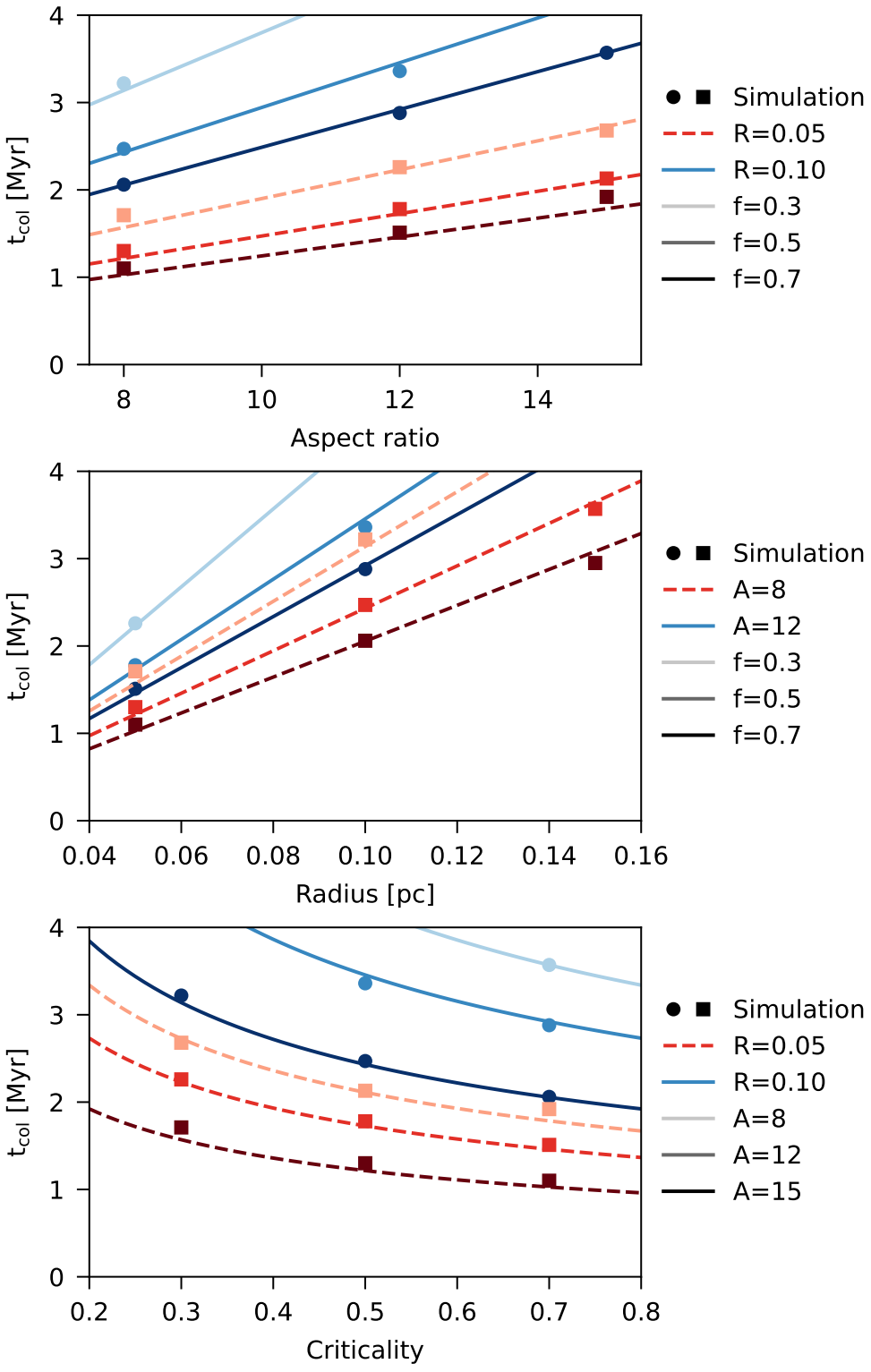

Figure 3.3: Results of the parameter study to determine κ and α for Equation 3.24. Several simulations were carried out varying f, R and A. The markers (dots and squares) show the collapse time of the simulation. The lines show the model for different parameters determined by colour and style. The model fits the simulations for $\kappa = 1.22$ and $\alpha = 0.69$.

Table 3.1: Comparison of collapse times determined in simulations with radial velocities $t_{\mathrm{col},v_r\neq 0}$ and without $t_{\mathrm{col},v_r=0}$. The time difference between the two simulations is given by Δt, whereas a time step in the simulation takes 0.07 Myr.

f	R [pc]	A	$t_{\mathrm{col},v_r=0}$ [Myr]	$t_{\mathrm{col},v_r\neq 0}$ [Myr]	Δt [Myr]
0.3	0.05	12	2.26	2.26	0.00
0.5	0.05	12	1.78	1.71	0.07
0.7	0.05	12	1.51	1.44	0.07

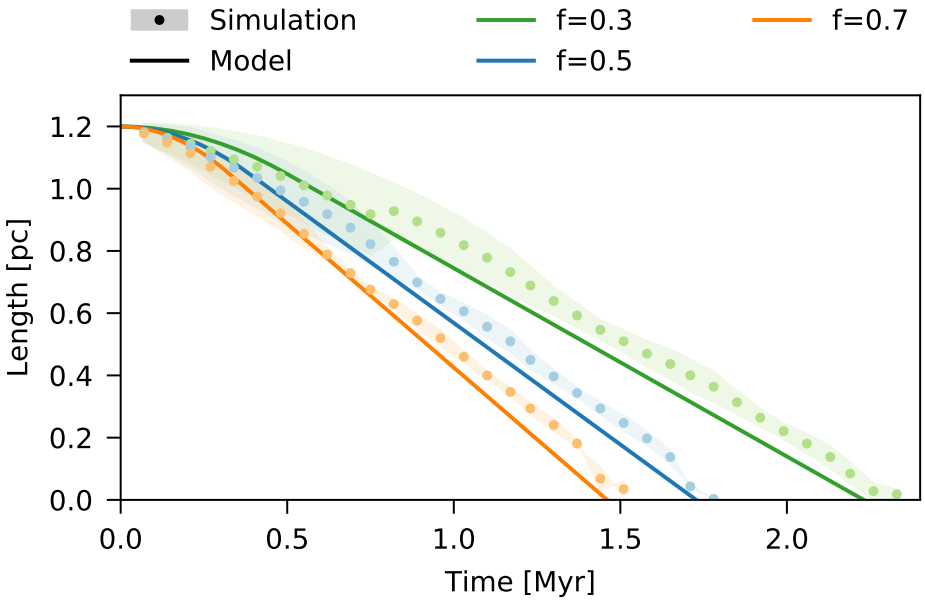

Figure 3.4: Comparison of the two phase model (solid lines, $A = 12$ and $R = 0.05\,\mathrm{pc}$) to the simulation values (light coloured as in Figure 3.2). The filled area shows the region between the edge off the filament and its peak in the simulation, the mean is given by the dots. Different criticalities are displayed in different colours. The model reproduces the simulated collapses very well.

necessary for filaments having other profiles than the hydrostatic one. As these are not in hydrostatic equilibrium they would collapse or expand radially to adjust to the equilibrium profile. However, to show that the radial collapse itself has only minor influences on the collapse, we performed hydrodynamic simulations including also radial velocities perpendicular to the long axis. The results are depicted in Table 3.1. As the cores start to collapse we included sink particles and define the time they need to reach the centre as the collapse timescale. As seen in Table 3.1, the deviations between the simulations with and without radial velocity is at maximum one output and can be neglected. Thus, the suppression of radial velocities has no influence on the longitudinal collapse time of a filament.

Not only does the model reproduce the collapse times accurately but it also describes the collapse itself as shown in Figure 3.4 where the length evolution of filaments with different criticalities are depicted. The shaded areas and the dots represent the simulation and the solid lines represent the corresponding model, as described in Figure 3.2. In this

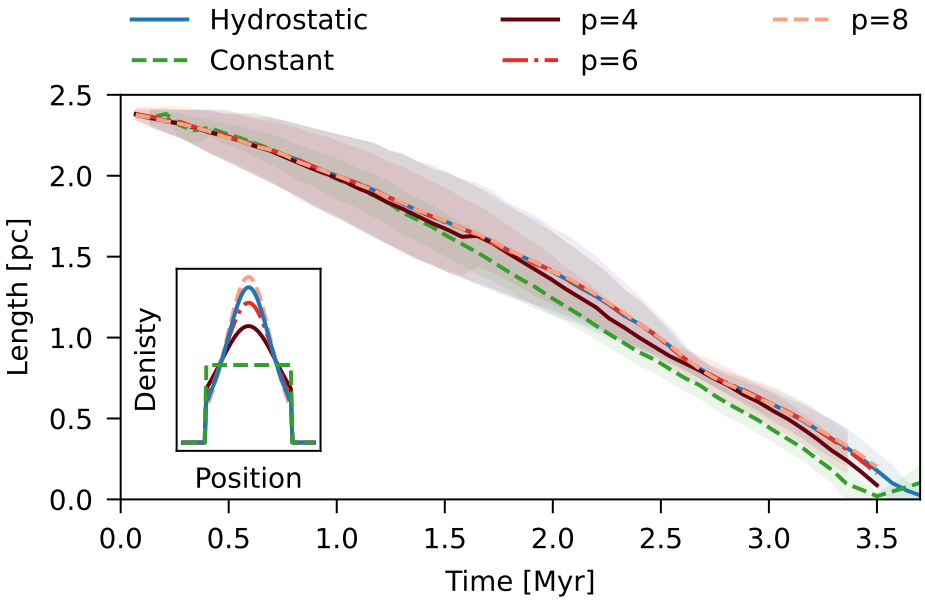

Figure 3.5: Length evolution for filaments with different radial density profiles with $A = 8, R = 0.15\,\mathrm{pc}$ and $f = 0.5$. The hydrostatic profile is given in blue, Equation 3.1, and steeper/flatter profiles according to Equation 3.29 are given in shades of red with corresponding exponent p. In comparison the constant density profile is depicted in green. The shaded areas again show the difference between the core and the actual end of the filament. A comparison of the radial densities of the corresponding profiles is given in the subplot on the left hand side.

example the aspect ratio was chosen to be $A = 12$ and the radius to be $R = 0.05\,\mathrm{pc}$. In all cases the simulation is very well reproduced by the model. The small underprediction is explained in the following section.

All in all, the two phase model describes the collapse and the corresponding collapse time well and reproduces the empirical formula from Clarke & Whitworth (2015).

3.6 Influence of different profiles

For the above analysis we assumed uniform density filaments since there is an analytical expression for the acceleration along a filament. Assuming a hydrostatic equilibrium, from a theoretical point of view we would expect to detect filaments with a hydrostatic profile which results in a r^{-4} density profile in the outskirts. Although centrally peaked density profiles are observed in filaments their profile is flatter than the hydrostatic one, about r^{-2} (Lada et al., 1999; Arzoumanian et al., 2011; Palmeirim et al., 2013; Cox et al., 2016). Thus, in the following we investigate the influence of different profiles on the collapse of a filament.

Figure 3.1 already shows that different radial profiles lead to different accelerations at the end of the filament. In order to check whether this has any kind of influence on the collapse time, we performed simulations with diverse density profiles. An example is given in Figure 3.5. All filaments have the same initial condition in terms of $A = 8$, $R = 0.15\,\mathrm{pc}$

and $f = 0.5$. The hydrostatic profile, given in blue, follows the density distribution for a filament in hydrostatic equilibrium (see Equation 3.1). The label 'Constant' means that the filament has a uniform density, represented by the green dashed line. The others follow a flatter or steeper profile than the hydrostatic one, a Plummer-like profile:

$$\rho(r) = \rho_{\mathrm{c}} \left[1 + \left(\frac{r}{H'}\right)^2\right]^{-p/2}, \tag{3.29}$$

with H' being:

$$H'^2 = \frac{2c_s^2}{\pi G \bar{\rho}} \tag{3.30}$$

and $\bar{\rho}$ the average density of the filament. The power-law index p was varied in the range between four and eight. The central density is adjusted such, that the overall filament has a criticality of $f = 0.5$. All filaments have a very similar time evolution (see Figure 3.5). However, a trend can be seen: Filaments with a flatter density distribution seem to collapse faster than filaments with a steeper density distribution. This is counterintuitive because the acceleration at the edge is larger for filaments with a more peaked profile (see Figure 3.1). We also see this trend in simulations with different parameters (in terms of f, A and R). However, the effect seems to be always smaller than 10%. Thus, the approximation of the acceleration of a uniform density filament seems to be accurate enough.

In order to understand why the hydrostatic filament collapses slower compared to the filament with the constant density distribution, we look at their velocity evolution in the simulation given in Figure 3.6. Three different examples are shown and their parameters are indicated in the upper left corner. The blue solid line indicates the velocity evolution of the hydrostatic filament, whereas the green dashed line depicts the uniform density case. Especially for lower line-mass filaments with f=0.3 and f=0.5 the velocity evolves differently for the two cases. Assuming the two phase model, a linear increase of velocity followed by a terminal velocity is expected as shown by the light green dashed line. It is a reasonable approximation of the simulated velocity for a constant density profile. However, for the hydrostatic case, there are strong deviations before reaching the final terminal velocity predicted by the model. An intermediate terminal velocity is reached. This can be explained by the strong density increase in the centre for a peaked profile, as can be seen in the box on the lower right side. Since the density inside is much higher, this induces a stronger ram pressure, and thus an earlier phase transition to an intermediate terminal velocity. We assume an approximation by a stacked profile would be more fitting, consisting of two constant density filaments, a more dense inner region and a diffuse outer region as indicated by the grey dotted line in the profile plot. The inner density is determined by the central density ρ_c, whereas the outer density is the boundary density ρ_b, the density cut is chosen such that the filament has the same criticality and radius as the other profiles. First the inner dense region collapses which reaches a terminal velocity rather fast but after a certain time the more diffuse outer region collapses onto the core and adds the momentum to get to the final terminal velocity. This effect delays the collapse for a short amount of time, and thus a systematic trend is seen that uniform density filaments collapse faster than hydrostatic ones. Because the deviations in the simulations were always below 10%, the effect is negligible.

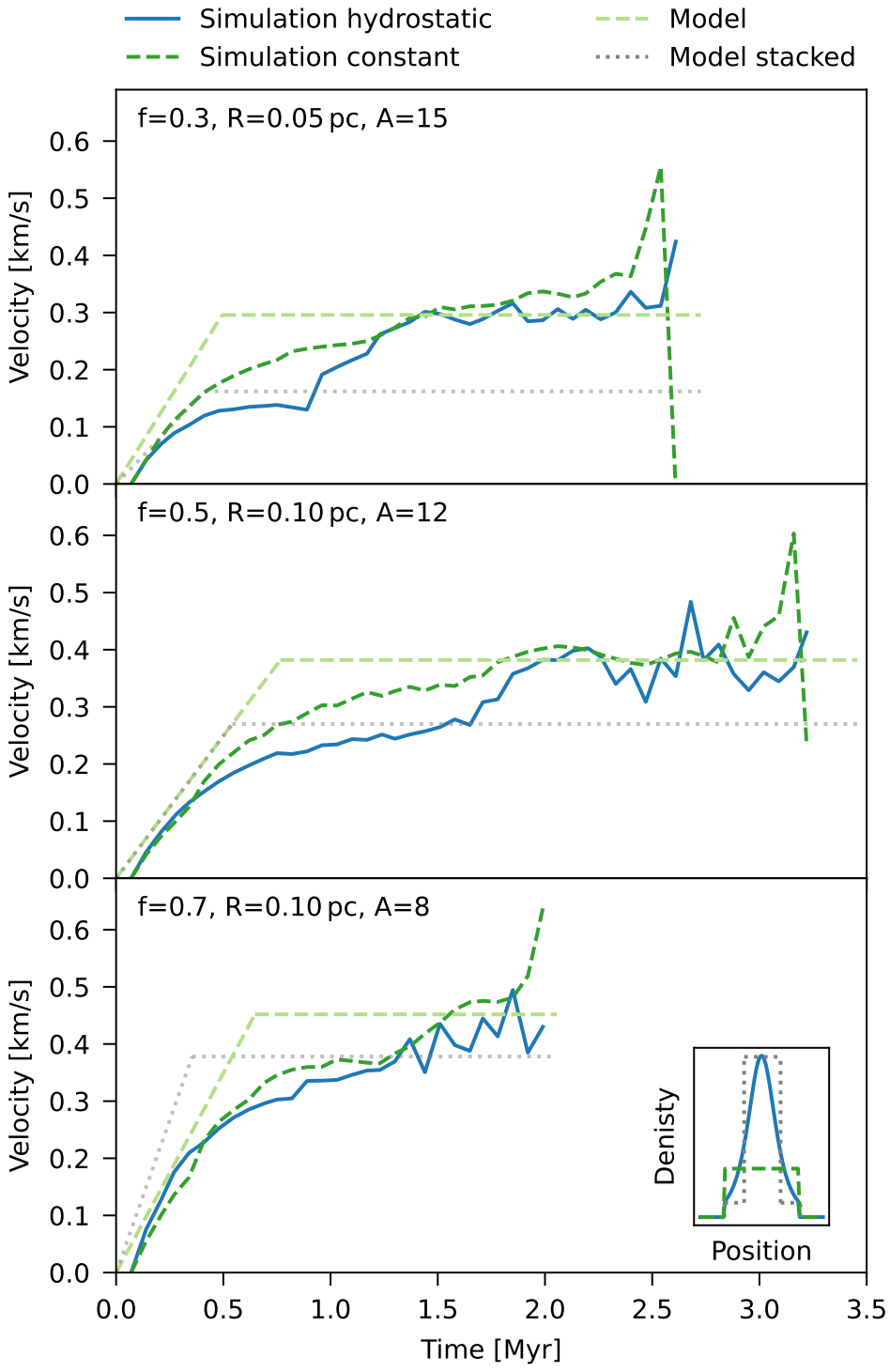

Figure 3.6: Velocity evolution for filaments with three different sets of parameters indicated in the left upper corner. Each graph compares the velocity evolution for the hydrostatic (blue solid line) and constant (green dashed line) velocity profile with the model (light green dashed line) and for a model with a stacked density distribution (grey dotted line). The profiles are depicted in the lower right corner.

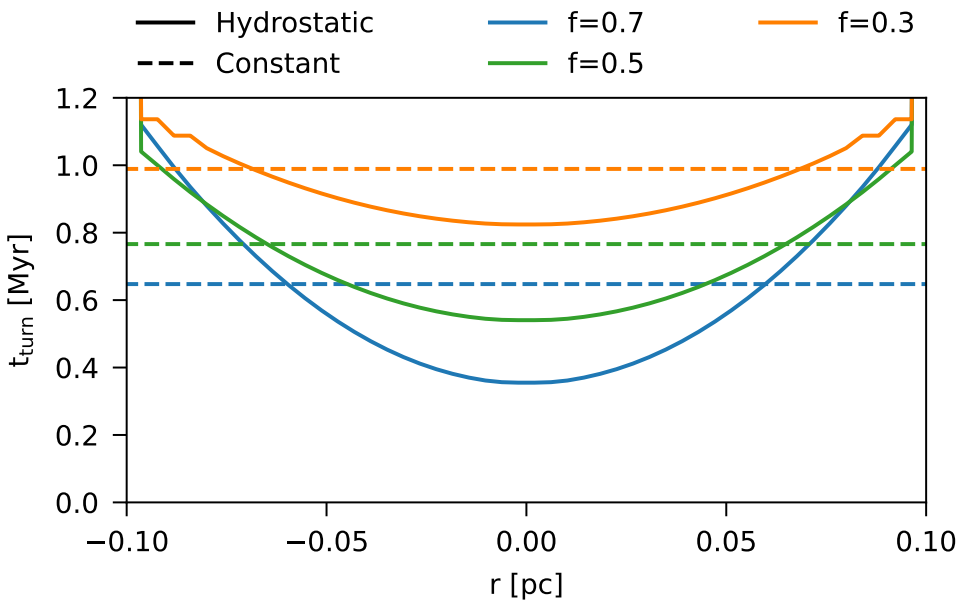

Figure 3.7: The radial dependency of the turning time for different criticalities. The dashed line represents a constant density distribution whereas the solid line shows the turning time of a hydrostatic profile. The used parameters are $A = 8$ and $R = 0.1\,\mathrm{pc}$.

This effect is depicted for different criticalities in Figure 3.7. Since the turning time only depends on the density, it is constant for a uniform density filament (depicted by the dashed line), whereas the hydrostatic filaments show a radially dependent turning time. Although the constant profile gives a good median, it is only an approximation.

Summing up, since the deviations for different filament profiles are small in simulations, it is sufficient to use the uniform density model in general as a good approximation of the collapse timescale.

3.7 Discussion

During this analysis several approximations have been made to describe the complex collapse of a filament. We will discuss in the following how these affect the presented results and give an example application of our model.

During the overall collapse the edge effect is not the only way of creating cores inside the filament. Perturbations can grow inside also leading to collapsing regions. For a hydrostatic filament the timescale on which perturbations form cores inside the filament is given by the perturbation timescale

$$t_{\mathrm{pert}} = \tau_{\mathrm{dom}} \log\left[\left(\frac{1}{f} - 1\right)\frac{1}{\epsilon}\right], \tag{3.31}$$

which was already given by Equation 25 in Hoemann et al. (2021). τ_{dom} is the dominant fragmentation mode, which was calculated following Appendix E in Fischera & Martin (2012), compare Nagasawa (1987); Heigl et al. (2020). In the following we adopt a perturbation strength of $\epsilon = 0.09$, based on the observations of Roy et al. (2015). Figure

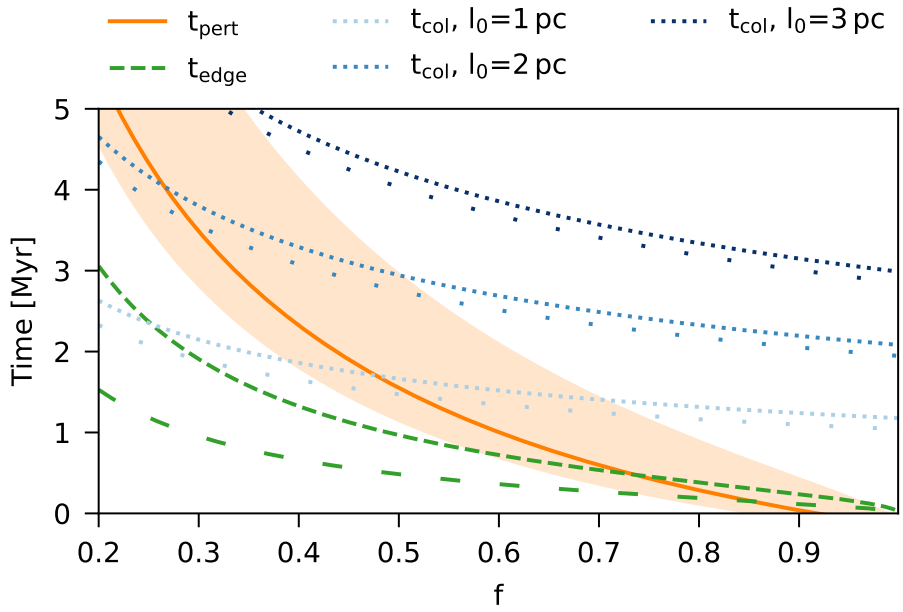

Figure 3.8: Comparison of different timescales in dependence of the criticality f. The edge effect formation timescale visualized in dashed green for $R = 0.1\,\mathrm{pc}$ (Equation 3.11, and the loosely dashed line for $R = 0.05\,\mathrm{pc}$), perturbation timescale in orange (Equation 3.31, in the shaded area the perturbation strength is varied) and the collapse timescale in dotted blue (Equation 3.24). Varying initial filament lengths are given by different shades of blue. The dotted lines show the collapse time for $R = 0.1\,\mathrm{pc}$ and the sparsely dotted lines for R=0.05 pc.

3.8 shows the perturbation timescale (orange solid line, the light orange region depicts $0.01 < \epsilon < 0.17$) in comparison to the edge effect formation timescale (Equation 3.11; dashed solid line for $R = 0.1\,\mathrm{pc}$ and loosely dashed for $R = 0.05\,\mathrm{pc}$) and the collapse timescale for $R = 0.1\,\mathrm{pc}$ in dotted lines and $R = 0.05\,\mathrm{pc}$ in the loosely dotted lines for different lengths l_0. For low line-mass filaments with small aspect ratios A a dominant edge effect can be expected, whereas for filaments with larger line-masses, perturbations grow faster. The edge effect, leading to dense cores on both ends of the filament, should however be visible in all cases.

In this study we considered that the initial density distribution does not change along the filament. However, if we vary the density, different collapse modes can be expected. For example Seifried & Walch (2015) found that a density enhancement of factor three leads to a 'centralized collapse' mode.

Since the presented model provides the length evolution of a filament, the age of a filament can be determined if the original length can be estimated. Taking into account the total mass of the filament and that the density in the inner part of the filament stays mostly constant, the length can be extrapolated. Using the current length, the age can then be determined by rearranging Equation 3.23:

$$t = \begin{cases} \sqrt{\frac{l_0 - l(t)}{\alpha 2\pi G \bar{\rho} R}} & \text{for } t < t_{\mathrm{turn}} \\ \left(\frac{l_0 - l(t)}{\kappa 2R} + \kappa \right) / \sqrt{\alpha 4\pi G \bar{\rho}} & \text{for } t \geq t_{\mathrm{turn}} \end{cases}, \tag{3.32}$$

considering that the edges are the only cores inside the filament, because the model does not account for other perturbations.

Summing up, the presented model has limitations due to its approximations but it gives a good estimate of the collapse time and the length evolution, especially for low line-mass and short filaments.

3.8 Conclusion

We show that the longitudinal collapse of a uniform density filament is a two step process. In the first phase, the filament accelerates until the turning time where the ram pressure counterbalances the gravitational acceleration and a terminal velocity is reached. This leads to a simple analytic model describing the length evolution and the resulting collapse time which explains the established empirical equation by Clarke & Whitworth (2015). For filaments with a peaked density distributions, the radial dependence of the turning time leads to the fact that the final terminal velocity is reached later. However, we find that all tested profiles are nevertheless well described by the collapse of a uniform density filament because the deviations are small. Since the collapse timescale is long in comparison to the edge effect formation and the perturbation timescale, it is unlikely that filaments collapses before forming cores. Thus, the edge effect is expected to dominate in low line-mass filaments whereas for large line-mass filaments perturbations can grow on a similar timescale.

Acknowledgements

We thank the anonymous referee for the detailed comments improving the quality of the paper. This research was supported by the Excellence Cluster ORIGINS which is funded by the Deutsche Forschungsgemeinschaft (DFG, German Research Foundation) under Germany's Excellence Strategy - EXC-2094 - 390783311. We thank the CAST group for helpful discussion and comments.

Chapter 4

Paper III – Filament fragmentation: Density gradients suppress end dominated collapse

Elena Hoemann, Stefan Heigl and Andreas Burkert, 2023, *arXiv e-prints*, arXiv:2307.11162, accepted for publication in *Monthly Notices of the Royal Astronomical Society*

The onset of star formation is set by the collapse of filaments in the interstellar medium. From a theoretical point of view, an isolated cylindrical filament forms cores via the edge effect. Due to the self-gravity of a filament, the strong increase in acceleration at both ends leads to a pile-up of matter which collapses into cores. However, this effect is rarely observed. Most theoretical models consider a sharp density cut-off at the edge of the filament, whereas a smoother transition is more realistic and would also decrease the acceleration at the ends of the filament. We show that the edge effect can be significantly slowed down by a density gradient, although not completely avoided. However, this allows perturbations inside the filament to grow faster than the edge. We determine the critical density gradient for which the timescales are equal and find it to be of the order of several times the filament radius. Hence, the density gradient at the ends of a filament is an essential parameter for fragmentation and the low rate of observed cases of the edge effect could be naturally explained by shallow gradients.

Keywords: stars:formation – ISM:kinematics and dynamics – ISM:structure

4.1 Introduction

Observations show that the molecular interstellar medium is pervaded by filaments (Schneider & Elmegreen, 1979; André et al., 2010; Arzoumanian et al., 2013; André et al., 2014). They are key in understanding the formation of stars since prestellar cores are mainly found within these cold, dense, filamentary structures (Arzoumanian et al., 2011; Könyves et al., 2015). They span several orders of magnitude (Hacar et al., 2023) from hundreds of parsecs in length down to the sub-parsec regime (Molinari et al., 2010; André et al., 2010; Hacar et al., 2013; Goodman et al., 2014; Mattern et al., 2018; Schmiedeke et al., 2021). Besides their obvious connection to star formation, there still remain many open questions on the formation, evolution and collapse of filaments.

Particularly the formation of cores and their consequent collapse is interesting since this is the stage of early star formation. For isolated filaments, fragmentation is supposed to happen via two competing processes: the edge effect (Bastien, 1983; Burkert & Hartmann, 2004; Pon et al., 2012) and the growth of perturbations (Stodólkiewicz, 1963; Nagasawa, 1987; Fischera & Martin, 2012). The edge effect consists of creating cores at the ends of the filament during the overall filament collapse. Since there is no density distribution for which the filament is in hydrostatic equilibrium along its main axis, it will collapse longitudinally due to self-gravity. This gravitational acceleration has a sharp increase in the end regions of the filament, and thus matter is swept up at the ends which forms a core and collapses after accumulating enough mass (Burkert & Hartmann, 2004; Hartmann & Burkert, 2007; Li et al., 2016). Contrary to this theoretical expectation, such pronounced ends are rarely observed (Zernickel et al., 2013; Kainulainen et al., 2016; Dewangan et al., 2019; Bhadari et al., 2020; Yuan et al., 2020; Cheng et al., 2021), which leads to the question of why we do not observe end-dominated filaments more often.

For magnetised, disc-like clouds the formation of an outer ring is the pendant to the edge effect. Li (2001) already found that the creation of a ring is correlated to the profile of the disc and the sound speed. However, for filaments Seifried & Walch (2015) showed that an initial density peak in the centre of the filament leads to a centrally-dominated collapse instead of an end-dominated one. In case of short filaments with aspect ratios of 3:1 the longitudinal collapse was also investigated by Keto & Burkert (2014). They showed that for low line-masses the filament collapses longitudinally into a central core that begins to go through a complex pattern of oscillations. Although such a longitudinal collapse has not yet been confirmed by observations (Roy et al., 2015) the predicted oscillations of the resulting cores are (Redman et al., 2006; Aguti et al., 2007). In addition, Heigl et al. (2022) showed that a filament created by a constant inflow region can suppress the edge effect. The constant inflow region rebuilds the filament during the overall filament collapse leading to a density gradient in the end region. This gradient leads to a decrease in the acceleration at the end of the filament which slows down the creation of the edge effect. Although not all filaments are expected to have such high and constant accretion, a smooth transition from the filament end into the surrounding medium is expected. This raises the question of whether a gradient at the end of the filament can stop the edge effect and if so, under which condition.

In general, cores are much more often detected inside filaments. These can form due to the growth of density perturbations. Although the expected spacing of the cores due to perturbation theory (Nagasawa, 1987; Larson, 1985; Inutsuka & Miyama, 1992;

Gehman et al., 1996; Hosseinirad et al., 2017) is mostly not observed, several filaments with regularly spaced cores were detected (Tafalla & Hacar, 2015; Zhang, Guo-Yin et al., 2020).

In this paper, we show that the edge effect itself cannot be stopped by any density profile at the end region of the filament. However, the collapse can be slowed down by a density gradient, such that perturbations can grow faster inside the filament. This is a natural explanation why filaments rarely show an edge effect. We present an analytic model for the conditions under which the edge should be dominant and under which conditions perturbations can grow faster and confirm it by numerical simulations.

The paper is organized as follows: First, the basic principle of hydrostatic filaments, the edge effect and perturbations are discussed in Section 4.2. Then we argue why the edge effect can never be avoided completely in Section 4.3. The derivation of the critical density gradient for which perturbations within the filament grow faster than at the edge is presented in Section 4.4, followed by the validation by simulations in Section 4.5. Finally, the results are discussed and conclusions are drawn in Sections 4.6 & 4.7.

4.2 Basic principles

4.2.1 Hydrostatic filaments

Considering filaments as isothermal cylinders, a hydrostatic solution for the radial profile was already found by Stodólkiewicz (1963) and Ostriker (1964):

$$\rho(r) = \rho_\mathrm{c} \left[1 + \left(\frac{r}{H}\right)^2\right]^{-2} \tag{4.1}$$

with H the scale height:

$$H^2 = \frac{2c_\mathrm{s}^2}{\pi G \rho_\mathrm{c}} \tag{4.2}$$

and c_s being the sound speed ($0.19\,\mathrm{km\,s^{-1}}$for a mean molecular weight of 2.36 and a temperature of 10 K), G the gravitational constant and ρ_c the central density of the filament. The filament is radially constrained by the pressure equilibrium between the boundary pressure and the external pressure $P_\mathrm{ext} = P_\mathrm{b}$. Its line-mass is given by its overall mass divided by its length:

$$\mu = \frac{M}{l}. \tag{4.3}$$

Integrating the density distribution radially until infinity results in the maximum line-mass for which a hydrostatic solution exists, given by

$$\mu_\mathrm{crit} = \frac{2c_\mathrm{s}^2}{G} \approx 16.4\,\mathrm{M_\odot\,pc^{-1}}, \tag{4.4}$$

above which all filaments would start to collapse radially. The value is calculated for 10 K. The criticality f is then the ratio of the actual line-mass divided by the critical line-mass

$$f = \frac{\mu}{\mu_\mathrm{crit}}. \tag{4.5}$$

The radial boundary density of the filament can be calculated by

$$\rho_{\rm b} = \rho_{\rm c}(1-f)^2 \tag{4.6}$$

and the radius of this boundary is given by

$$R = H\left(\frac{f}{1-f}\right)^{1/2}. \tag{4.7}$$

4.2.2 Edge effect

Since there is no hydrostatic solution for the density distribution along the main axis of a filament, the filament is expected to collapse longitudinally. The acceleration along a filament due to its self-gravity was already investigated by Burkert & Hartmann (2004):

$$a = -2\pi G\bar{\rho}\left[2z - \sqrt{\left(\frac{l}{2}+z\right)^2 + R^2} + \sqrt{\left(\frac{l}{2}-z\right)^2 + R^2}\right]. \tag{4.8}$$

with $\bar{\rho}$ the mean density and z the position along the filament. The steep increase of a at the end leads to a large velocity inwards along the main axis and as a result to a pileup of matter in these regions. The resulting clumps will begin to collapse onto themselves when they reach the critical line mass. At the same time, the end clumps still move inwards towards the centre of the filament, destroying the filament (Bastien, 1983; Toalá et al., 2011; Pon et al., 2012; Clarke & Whitworth, 2015). This is the so-called edge effect (Burkert & Hartmann, 2004). In an earlier paper (Hoemann et al., 2021) we investigated on which timescale the ends of a filament are formed:

$$\begin{aligned} t_{\rm edge} &= \sqrt{\left(\frac{1}{f}-1\right)\frac{2\kappa R}{|a_{\rm cm}|}} \\ &= \sqrt{\frac{1.69\times10^{-20}\,{\rm g\,cm^{-3}}}{f\rho_{\rm c}}}\,{\rm Myr} \end{aligned} \tag{4.9}$$

with $\kappa = 1.66$ and $a_{\rm cm}$ being the acceleration of the centre of mass of the filaments end region $a_{\rm cm} = a(l/2 - \kappa R/2)$. In the beginning, the two cores move in free fall and then are slowed down by ram pressure (Hoemann et al., 2022). With this two-phase approach, the longitudinal collapse timescale of a filament can be determined (Clarke & Whitworth, 2015; Hoemann et al., 2022)

$$t_{\rm col} = \frac{0.42+0.28A}{\sqrt{G\bar{\rho}}} \tag{4.10}$$

$$= \frac{0.42+0.28A}{\sqrt{\bar{\rho}/1.50\times10^{-20}\,{\rm g\,cm^{-3}}}}\,{\rm Myr}, \tag{4.11}$$

with $A = L/2R$ being the aspect ratio and $\bar{\rho}$ the mean density of the filament. This is now the overall collapse time, the timescale on which the two end cores move to the centre.

Although the edge effect is predicted by theory, it is only rarely observed (Zernickel et al., 2013; Kainulainen et al., 2016; Dewangan et al., 2019; Bhadari et al., 2020; Yuan et al., 2020; Cheng et al., 2021). This raises the question of why we do not observe the edge effect in most cases. However, most of the former theoretical studies were done with a sharp density cut-off at the ends of the filament which influences the acceleration in the end region. A smoother density gradient could influence and weaken the edge effect significantly allowing perturbations to grow faster. This is what we will investigate in the next sections.

4.2.3 Perturbations

In competition to the edge effect, line-mass perturbations within the filament can also grow. Here we characterize a perturbation of the line-mass by

$$f(z) = f_0 \left[1 + \epsilon \cos\left(\frac{2\pi z}{\lambda_{\rm dom}}\right)\right], \tag{4.12}$$

with f_0 the unperturbed line-mass and z the coordinate along the filament. $z = 0$ corresponds to the centre of the perturbation. ϵ is the perturbation strength which is observed to be typically 0.09 (Roy et al., 2015) and $\lambda_{\rm dom}$ is the dominant fragmentation length (see Fischera & Martin, 2012, Appendix E)

$$\lambda_{\rm dom} = \left(6.25 - 6.89f^2 + 9.18f^3 - 3.44f^4\right) FWHM_{\rm cyl} \tag{4.13}$$

using the full width at half maximum of the cylindrical filament $FWHM_{\rm cyl}$. Following a perturbation analysis (Nagasawa, 1987) the timescale can now be determined on which such a perturbation would grow into a collapsing core (compare Heigl et al., 2020; Hoemann et al., 2021)

$$t_{\rm pert} = \tau_{\rm dom} \log\left[\left(\frac{1}{f} - 1\right)\frac{1}{\epsilon}\right]. \tag{4.14}$$

Here $\tau_{\rm dom}$ denotes the dominant growth timescale, which can be determined with Fischera & Martin (2012), Appendix E

$$\tau_{\rm dom} = \left(4.08 - 2.99f^2 + 1.46f^3 + 0.40f^4\right) / \sqrt{4\pi G \rho_{\rm c}}. \tag{4.15}$$

Since most of the cores are found within filaments (Arzoumanian et al., 2011; Könyves et al., 2015), this is expected to be one of the most important channels for core formation, theoretically.

4.3 The inevitable edge effect

In former theoretical studies (e.g. Clarke & Whitworth, 2015; Hoemann et al., 2021), filaments are often considered to have a sharp edge, thus, a hard cut-off at the ends of the filament which makes analytic predictions possible (Burkert & Hartmann, 2004). However, a more realistic setup would be a smooth transition to the surrounding gas. Such a density gradient would lead to a decrease in acceleration at the ends of the filament.

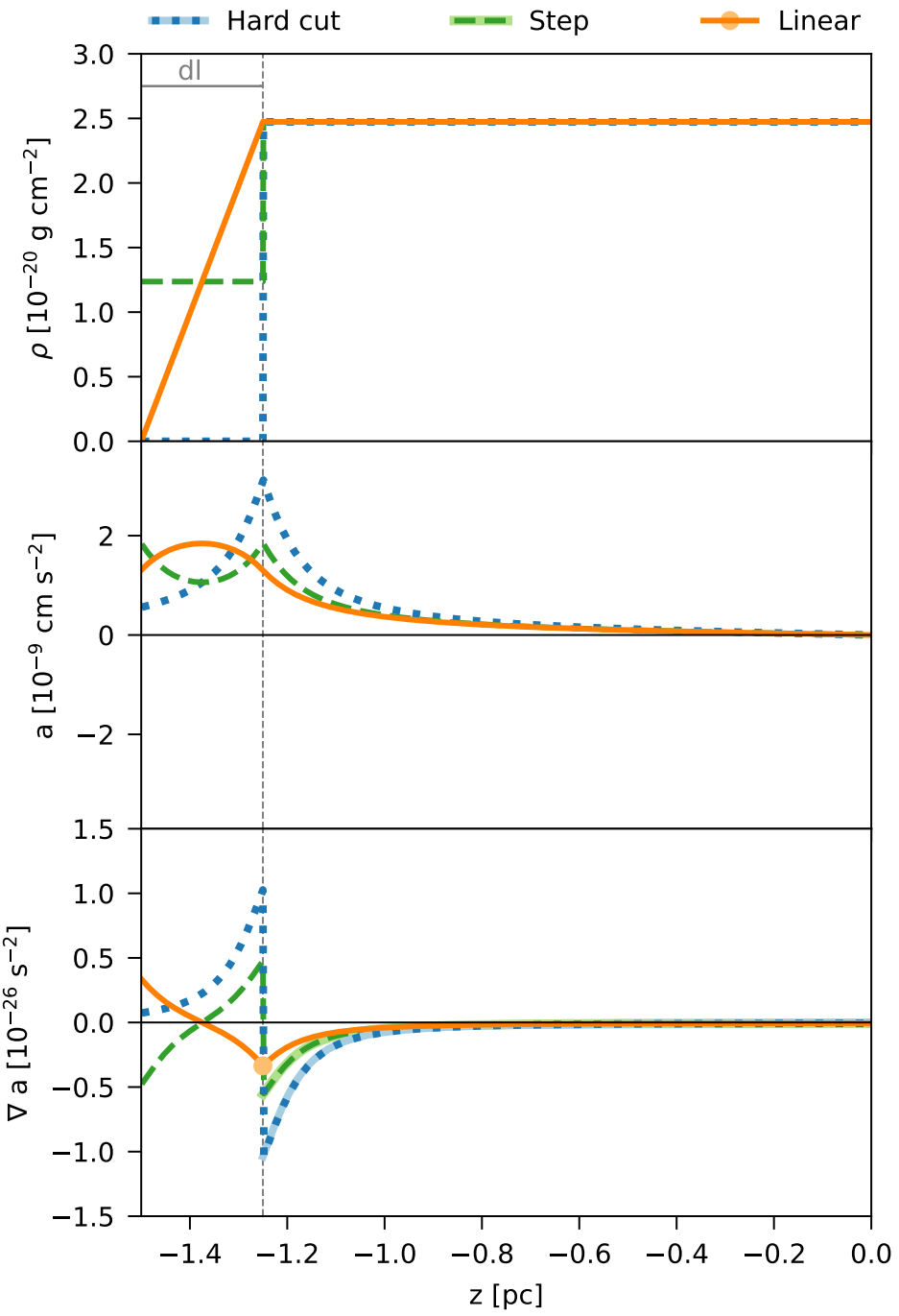

Figure 4.1: The top row shows the density distribution along the z-axes for three different profiles: A hard cut-off, where the density goes directly to zero after the filament ends, in dotted blue; A step for which the density is cut in half after the end and drops to zero at the edge of the end region, shown in dashed green; A linear end is depicted in orange, where the density transitions more smoothly into the surrounding. In the second row, the corresponding numerically determined acceleration is given and in the last row its gradient. For the gradient, the lighter colours depict the analytic solution which fits the numeric solution well.

The change in acceleration due to the end profile of the filament is depicted in Figure 4.1. The top row shows three simple density distributions. The hard cut-off is depicted as a blue dotted line. Here the density drops immediately to the external density at the end of the filament, which is often used for analytic approaches. The green dashed line shows a step edge, where the density halves at the filaments end and only drops to the external density at the edge of the end region. A linear end is given by the solid orange line. In this case, after the end of the filament the density decreases linearly to the external density. We consider the external density to be negligible and set it to zero, to make analytic predictions comparable. The second row depicts the acceleration for each of the profiles and the last row shows the gradient of the acceleration respectively. The acceleration of the hard cut-off can also be determined by Equation 4.8. The calculation was done numerically, but the lines and markers in lighter colours in the last row show the analytical expectation, described in more detail in the following, which fits the numerical solutions.

Differentiating Equation 4.8 leads to the gradient for the hard cut-off, shown in light blue in the lower plot in Figure 4.1 (derivation Appendix 4.7):

$$\nabla a_{\mathrm{cut}} = 2\pi G\rho \left[\frac{l/2+z}{\sqrt{(l/2+z)^2+R^2}} + \frac{l/2-z}{\sqrt{(l/2-z)^2+R^2}} - 2 \right]. \tag{4.16}$$

For the step function, which is depicted in light green, considering of outside material leads to:

$$\begin{aligned} \nabla a_{\mathrm{step}} = &- 2\pi G\rho \Bigg[-\frac{1}{2}\frac{l/2+z}{\sqrt{R^2+(l/2+z)^2}} - \frac{1}{2}\frac{l/2-z}{\sqrt{R^2+(l/2-z)^2}} + 2 \\ &- \frac{1}{2}\frac{l/2+dl+z}{\sqrt{R^2+(l/2+dl+z)^2}} - \frac{1}{2}\frac{l/2+dl-z}{\sqrt{R^2+(l/2+dl-z)^2}} \Bigg] \end{aligned} \tag{4.17}$$

dl donates the length of the additional end region, given in Figure 4.1. The derivation can be found in Appendix 4.7. For the linear density distribution at the end, we calculated the gradient of the acceleration only for the filament end since this is the region of interest (derivation in Appendix 4.7):

$$\nabla a_{\mathrm{lin}} = 2\pi G\rho \left[\frac{\sqrt{R^2+dl^2}}{dl} - \frac{R}{dl} + \frac{l}{\sqrt{R^2+l^2}} - 2 \right]. \tag{4.18}$$

We checked the limits for consistency. Case 1: $dl \to 0$ reproduces the gradient for the hard cut-off:

$$\lim_{dl\to 0} \nabla a_{\mathrm{lin}} = 2\pi G\rho \left[\frac{l}{\sqrt{R^2+l^2}} - 2 \right] \tag{4.19}$$

and case 2: $dl \to \infty$ has to be zero since it would be an infinite long filament, thus also $l \to \infty$

$$\lim_{dl,l\to\infty} \nabla a_{\mathrm{lin}} = 0. \tag{4.20}$$

Altogether, the important parameter for the collapse of a filament is the amount of acceleration in the end region, which can be weakened by a smooth density transition. However, every density gradient will at least cause a small peak in the gradient of the acceleration, as can be seen in Equation 4.18. Thus, during the filament collapse the formation of an edge effect will always be triggered. The amount of acceleration determines how fast the edge grows:

$$t_{\rm edge} \propto \frac{1}{\sqrt{a}}. \tag{4.21}$$

Therefore, the edge effect can be slowed down by a density gradient at the end, reducing the acceleration in this region. However, the collapse timescale of a filament scales with the same dependence on a:

$$t_{\rm col} \propto \frac{1}{\sqrt{a}} \tag{4.22}$$

which means that if the filament encounters an edge effect with a cut-off, it also encounters an edge effect with any end profile before collapsing, because collapse and edge effect are slowed down by the same amount. Thus, a gradient cannot stop the edge effect, it can just slow it down.

However, there is also a third effect, the growth of perturbations, which plays an important role which we consider in the next section.

4.4 Critical density gradient

As was shown in the previous section, the edge effect cannot be stopped, but it can be slowed down. The question is, under with circumstances is the slowdown sufficient to make perturbations grow faster than the edge effect. In contrast to the overall collapse timescale, the timescale on which perturbations grow is independent of the acceleration at the ends. Thus, even if the acceleration at the ends is low, perturbations grow nevertheless. Hence, if perturbations grow faster than the end cores, we do not expect to see a dominant edge effect.

To get a criterion for which perturbations would grow faster than the edge effect, we consider a simple geometry: a linear transition from the filament to the outside medium as depicted by the orange line in Figure 4.1 in the first row. We want to determine the density gradient ρ/dl at which perturbations grow as fast as the edge effect $t_{\rm edge} = t_{\rm pert}$ as indicated in Figure 4.2. The dashed line shows the perturbation timescale (Equation 4.12) and the solid line is the edge effect formation, given by Equation 4.9 using the centre of mass acceleration at the end of a filament for a linear density gradient:

$$\begin{aligned} a_{\rm cm} = -2\pi G\rho \Bigg[& \sqrt{\frac{\kappa^2}{4}+1}\frac{\kappa R^2}{4dl} - \frac{R^2}{2dl}\tanh^{-1}\left(\frac{-\kappa/2}{\sqrt{\kappa^2/4+1}}\right) \\ & - \left(\frac{1}{2}+\frac{\kappa R}{4dl}\right)\sqrt{R^2+\left(dl+\frac{\kappa R}{2}\right)^2} + \frac{1}{2}dl \\ & + \frac{R^2}{2dl}\tanh^{-1}\left(-\frac{dl+\kappa R/2}{\sqrt{(dl+\kappa R/2)^2+R^2}}\right) - l \end{aligned}$$

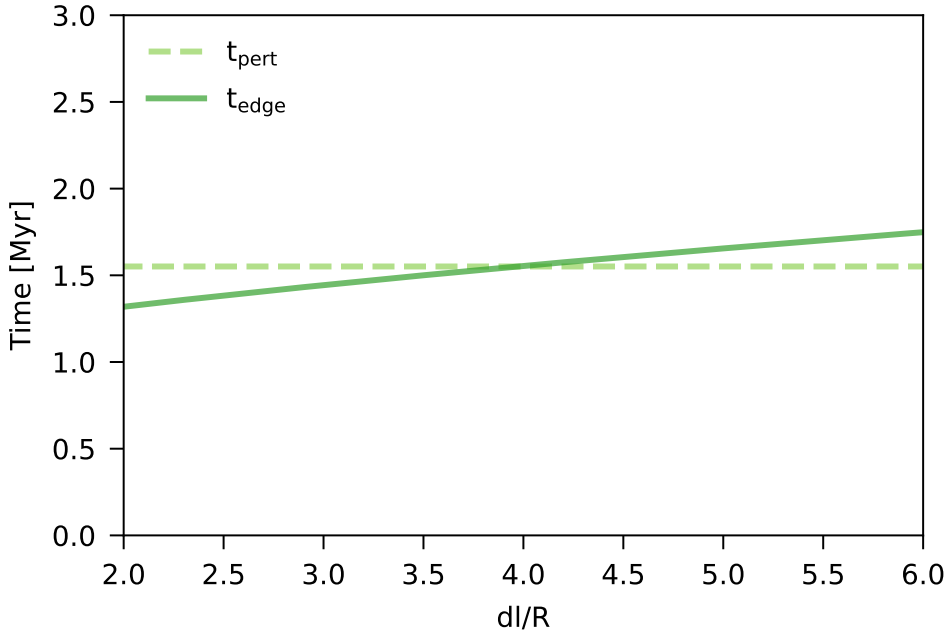

Figure 4.2: Comparison of the perturbation timescale (Equation 4.14), depicted by the dashed, light green line, with the edge effect formation timescale (Equation 4.9 and 4.8), shown by the darker solid, green line.

$$+\kappa R + \sqrt{R^2 + \left(l - \frac{\kappa R}{2}\right)^2}\Bigg]. \tag{4.23}$$

The derivation of this equation is provided in Appendix 4.7 and is valid for filaments with $l - \kappa R/2 \gg R$, thus filaments with large aspect ratios. The crossing point of the lines indicates the gradient where both effects grow on the same timescale. The determination of this crossing point is not straightforward. Therefore, we use Taylor approximations to determine the critical density gradient.

In the first step, we do a Taylor expansion of the acceleration at the end of the filament (Equation 4.23) around $dl = 0$ with Mathematica:

$$a \approx G\pi\rho\left[aR + bdl\right], \tag{4.24}$$

with free (a, b) parameters which are fitted to the numeric values at the end of the section. Inserting this into the edge effect formation timescale leads to:

$$t_{\mathrm{edge}} \approx \sqrt{\left(\frac{1}{f} - 1\right)\frac{2\kappa R}{G\pi\rho(aR + bdl)}}. \tag{4.25}$$

We did another Taylor expansion around $dl = 0$ for the last multiplier:

$$\frac{1}{\sqrt{(aR + bdl)}} \approx \sqrt{\frac{1}{aR}} - \frac{1}{2}\left[\left(\frac{1}{aR}\right)^{3/2} b\right] dl. \tag{4.26}$$

Inserting this into the edge effect formation timescale leads to:

$$t_{\mathrm{edge}} \approx \sqrt{\left(\frac{1}{f} - 1\right)\frac{2\kappa R}{G\pi\rho}}\left[\sqrt{\frac{1}{aR}} - \frac{1}{2}\frac{b}{(aR)^{3/2}} dl\right]. \tag{4.27}$$

Now the critical density gradient can be determined solving

$$t_{\rm edge} \stackrel{!}{=} t_{\rm pert} \tag{4.28}$$

for dl/R:

$$\frac{dl}{R} \approx -\frac{2a^{3/2}}{b}\left[t_{\rm pert}\sqrt{\frac{fG\pi\rho}{(1-f)2k}} - \frac{1}{\sqrt{a}}\right] \tag{4.29}$$

$$\approx \alpha\sqrt{\frac{G\pi\rho f}{(1-f)}}\tau_{\rm dom}\log\left(\frac{1-f}{f\epsilon}\right) - \beta. \tag{4.30}$$

The approximation of the critical gradient is presented in Figure 4.3, upper panel, for different aspect ratios indicated by the shaded grey lines for a perturbation strength of $\epsilon = 0.09$ which is the observed value (Roy et al., 2015). The filament's aspect ratio A belonging to the various line is given in the subscript. Our model only holds for long filaments, thus, the solution converges for large values of A. Parameters $\alpha = 4.22$ and $\beta = 8.17$ were fitted to the numeric values for a large aspect ratio ($A = 2000$) given as the black dots. The numerical values are well reproduced by the approximation. Filaments below the critical gradient would be expected to show a pronounced edge effect, whereas filaments above the line would grow perturbations on a similar timescale or faster. This shows that for filaments with a criticality greater than 0.7, we would expect perturbations to always grow faster. In the lower panel, we present the critical gradient for different perturbation strengths ϵ. The grey line indicates the observed value of $\epsilon = 0.09$ (Roy et al., 2015), which is also used to demonstrate the convergence of the solution. The blue lines present less dominant perturbations whereas the red curves depict the critical gradient for stronger perturbations. As expected for lower perturbations smoother gradients are needed to suppress the edge effect. In addition, the stronger perturbations shift the line-mass f above which all filaments would be dominated by perturbations to lighter filaments and to heavier filaments for the less perturbed filaments.

For validation, we compare the crossing point of $t_{\rm edge}$ and $t_{\rm pert}$ (see Figure 4.2) to the approximation of the edge effect formation timescale given by Equation 4.27 in Figure 4.4. As in Figure 4.2, the dashed line denotes $t_{\rm pert}$, the solid line $t_{\rm edge}$ for a filament with linear density gradient and the dotted line its approximation $t_{\rm edge,approx}$, given by Equation 4.25. The criticality is varied in the top row, the radius in the middle and the length in the last one, respectively indicated by different colours. As we used the approximation to determine the critical gradient the approximation has to be valid for the intersections, which fits well for the presented cases.

Altogether, the density gradient at the end of the filament leads to a decrease in acceleration, thus, there also has to be a critical acceleration which is needed in a certain setup to have dominant end cores. This can be calculated without any additional approximations using the same ansatz as before and solving for the acceleration:

$$t_{\rm edge} \stackrel{!}{=} t_{\rm pert} \tag{4.31}$$

$$a_{\rm crit} = \left(\frac{1}{f} - 1\right)\frac{2\kappa R}{\tau_{\rm dom}}\log^{-2}\left(\left(\frac{1}{f} - 1\right)\frac{1}{\epsilon}\right). \tag{4.32}$$

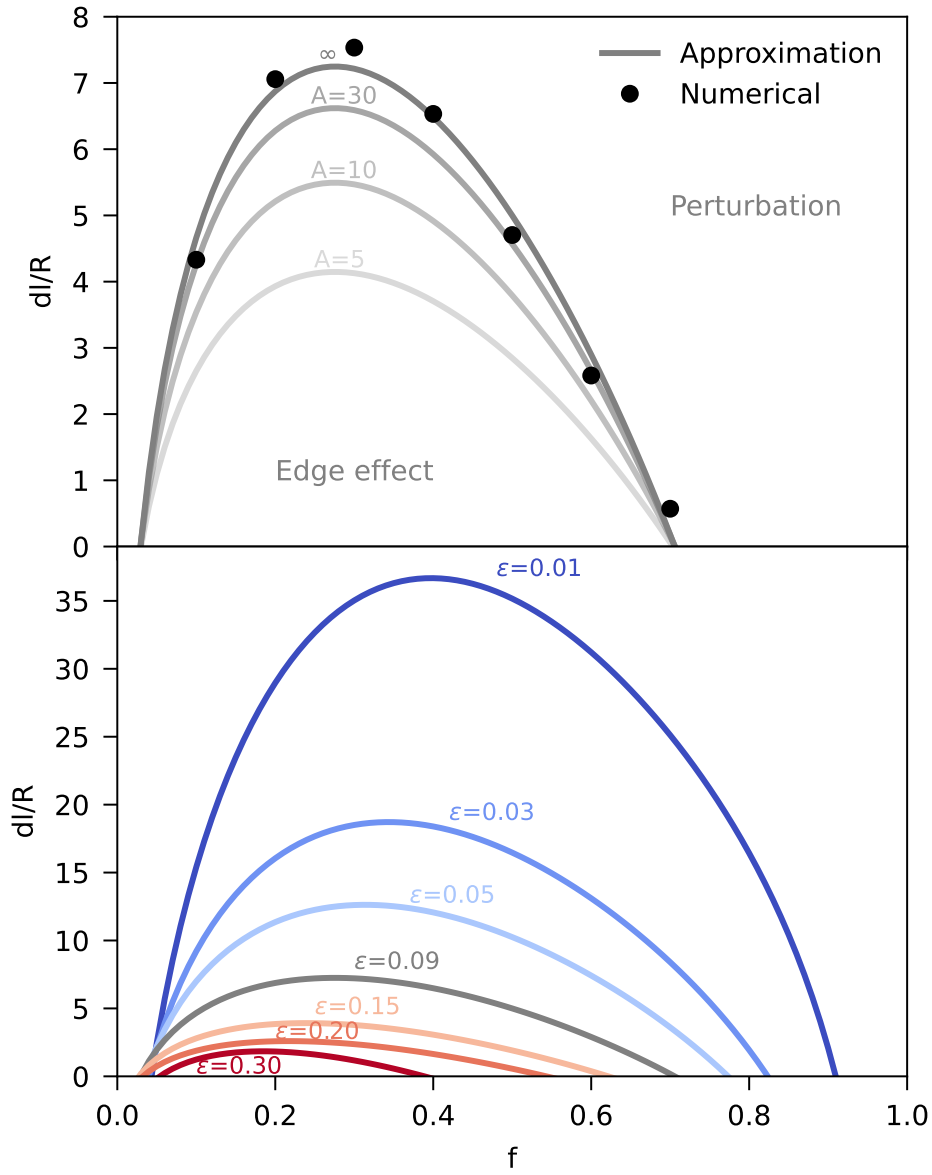

Figure 4.3: Top panel: The approximation of the critical gradient (Equation 4.30) is depicted for different criticalities in grey. The different shades depict solutions for different filament aspect ratios, indicated by the given number. The parameters (α, β) are fitted to the numerical solutions for a long filament ($R = 0.1\,\mathrm{pc}$, $l = 200\,\mathrm{pc}$), given by the black dots. Below the curve, a dominant edge effect is expected, whereas above the curve, perturbations grow faster, and thus no strong edge effect is expected.
Lower panel: The critical gradient is given for different perturbation strengths ϵ. The grey line shows the observed strength of $\epsilon = 0.09$ (Roy et al., 2015), in comparison in blue lower strength and in red stronger ones.

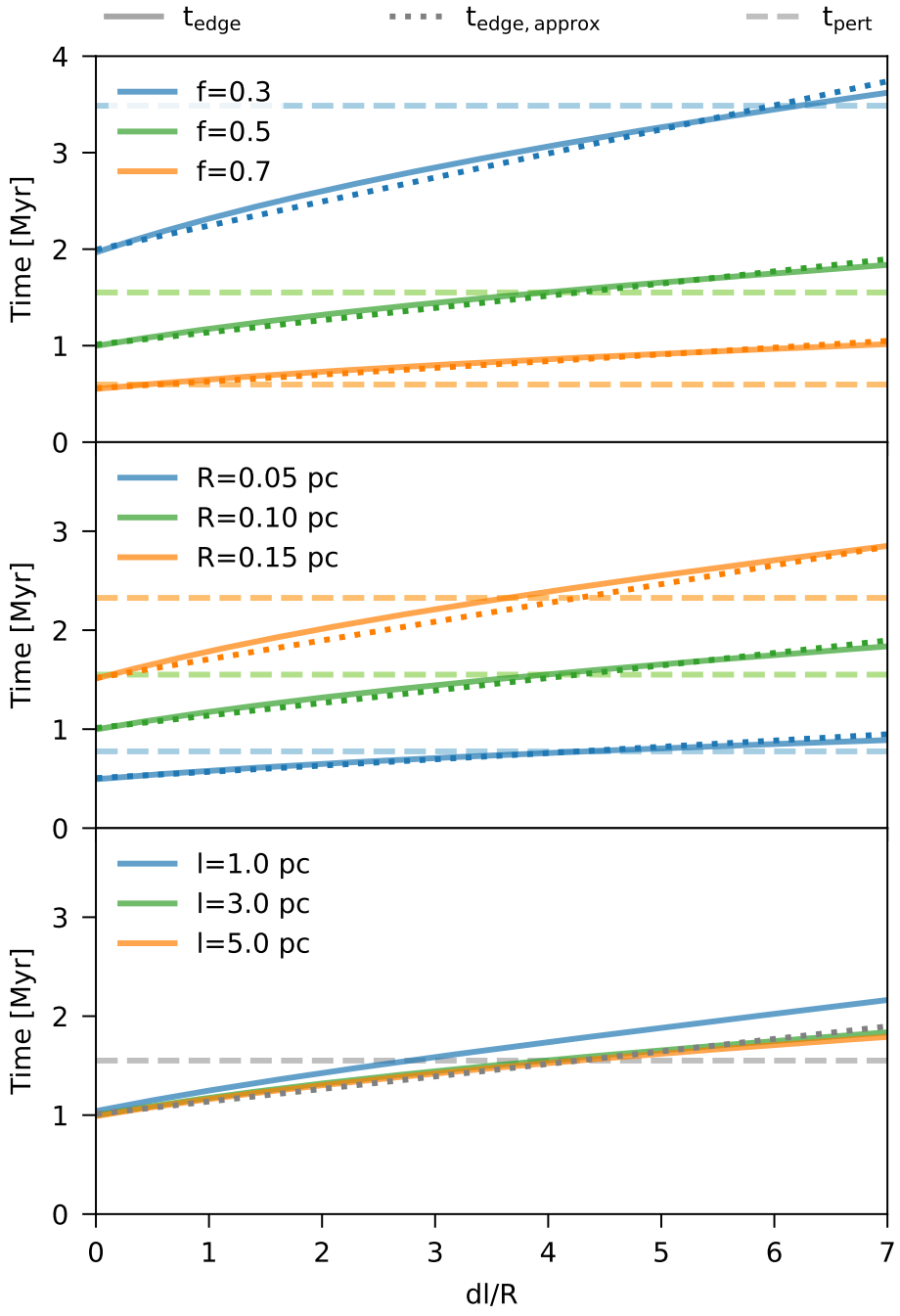

Figure 4.4: The same as Figure 4.2, but adding a comparison to the approximated edge effect time (Equation 4.27) with the dotted lines. In the first row, the dependency on criticality is depicted, in the second row on radius and in the last on the filament length. At the crossing points between t_{edge} and t_{pert} the approximation of the edge effect formation timescale is reasonable.

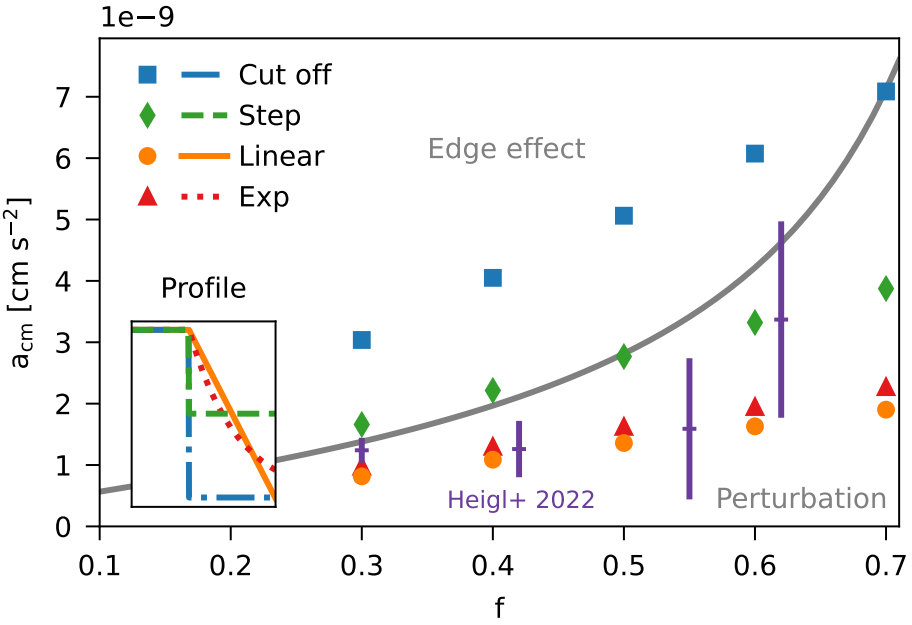

Figure 4.5: The grey line depicts the critical centre of mass acceleration (Equation 4.32) depending on criticality. The different markers give numeric results of the centre of mass acceleration of different filament end profiles given in the subplot. Above the grey line the edge effect is expected to be dominant, whereas below, perturbations would grow faster. In comparison, the violet crosses show the acceleration measured in the simulation by Heigl et al. (2022), where the edge effect was suppressed in agreement with our model. The used parameters were: $\epsilon = 0.09$, $R = 0.02\,\mathrm{pc}$, $l = 0.94\,\mathrm{pc}$, $dl/R = 9$.

An example is given in Figure 4.5 as a grey line for $\epsilon = 0.09$, $R = 0.02\,\mathrm{pc}$, $l = 0.94\,\mathrm{pc}$, $dl/R = 9$. The markers indicate the numerically determined acceleration of the centre of mass of the filament's end region for different profiles, indicated in the subplot. The violet crosses show the values of a simulation by Heigl et al. (2022) where the filament is created by a converging flow. While the filament starts to collapse material comes in at the filament's ends due to the constant inflow region. This creates a linear density gradient in the end region. Thus, it fits very well with our numeric solution for a linear end. Above the critical acceleration (grey line) an edge effect is expected whereas below perturbations should grow faster. Since the acceleration varies strongly in the end region, the determination from the simulation is error-prone, thus we show an error bar of the standard deviation 10 voxels ahead of the peak and behind. The linear and exponential profiles, which have a similar gradient, lie below the line for this specific example, whereas the hard cut-offs are expected to have dominant ends, especially for low line-masses. Since Heigl et al. (2022) did also not detect dominant end cores, it fits our results.

4.5 Validation by simulations

For validation, we performed isothermal hydrodynamic simulations with the adaptive mesh refinement code RAMSES (Teyssier, 2002). With a second-order Gudonov solver the Euler equations are solved in their conservative form using a MUSCL (Monotonic

Table 4.1: Results of the simulation "sim" in comparison to the expected result by the model "exp". "e" means simulations with dominant edge effect or "p" configurations where perturbations grow on the same timescale or faster. The edge effect and perturbation timescale, as determined in the simulation, are given in comparison to their expected values in brackets. An output timestep in the simulation takes $\Delta t = 0.1\,\mathrm{Myr}$. The length was always given by five times the dominant wavelength (Equation 4.13).

f	R [pc]	dl/R	t_{edge} [Myr]	t_{pert} [Myr]	exp	sim
0.5	0.1	10	1.76 (2.02)	1.57 (1.55)	p	p
0.5	0.1	6	1.47 (1.71)	1.57 (1.55)	p	p
0.5	0.1	2	1.18 (1.31)	1.57 (1.55)	e	e
0.5	0.05	6	0.78 (0.84)	0.78 (0.78)	p	p
0.3	0.05	10	1.27 (1.94)	1.67 (1.74)	p	e
0.3	0.1	10	2.55 (3.99)	3.14 (3.49)	p	e

Upstream-Centered Scheme for Conservation Laws, van Leer, 1979), the HLLC-Solver (Harten-Lax-van Leer- Contact, Toro et al., 1994) and the MC slope limiter (monotonized central-differenc, van Leer, 1979).

We set up filaments with perturbations in the line-mass as displayed in Figure 4.6. In the upper panel, a density slice through the filament is given and in the lower panels the according criticality and acceleration along the z-axes. The bending of the gradient in the end region is due to the cut off at boundary density, which will be discussed at the end of this section. Perturbations were inserted via Equation 4.12 going over into a flat region at the end, to not disturb the edge effect. At the filament end the linear transition into the surrounding density is depicted, in this case with a gradient of $dl/R = 6$. We cut the outermost peaks to not have an overlap between perturbations and the edge effect. Then, we varied the linear density gradient at both ends to validate the transition between perturbations and edge effect as given by Equation 4.30. We consider perturbations to be dominant if all cores collapse within a time span of 10% of each other, or the inner cores collapse first since then no pronounced edges can be detected. In contrast, the edge effect is considered to be dominating if the end cores collapse before the inner cores.

As a first test, we performed simulations for $f = 0.5$ and different gradients, given in Figure 4.7. Here we plot the criticality of the cores at the end f_{end} against the criticality of the cores formed from perturbations f_{pert}. Every marker is one output of the simulation in time-steps of $\Delta t = 0.1\,\mathrm{Myr}$ with $R = 0.1\,\mathrm{pc}$, $l = 0.3\,\mathrm{pc}$ and $f = 0.5$. For $dl/R = 10$ and $dl/R = 6$, both cores collapse within one time-step, thus, perturbations and edge effect collapse on the same timescale and no clear edge effect can be detected. Only for $dl/R = 2$ the edge effect collapses clearly faster than the perturbations which agrees with the fact that in this case a dominant edge core would be expected. This validates the critical gradient given in Figure 4.3 which predicts the transition between end core and perturbation domination for these parameters to be at $dl/R = 5$. Further validations for different parameters can be found in Table 4.1.

As a second test, we did simulations with smaller line-masses, given in Table 4.1. For low line-masses the predicted timescales for the edge effect deviate from the simulated ones. For large line-mass filaments this has only a minor impact on the prevalent fragmentation mode, however, for lighter filaments, the deviations are so strong that the edge

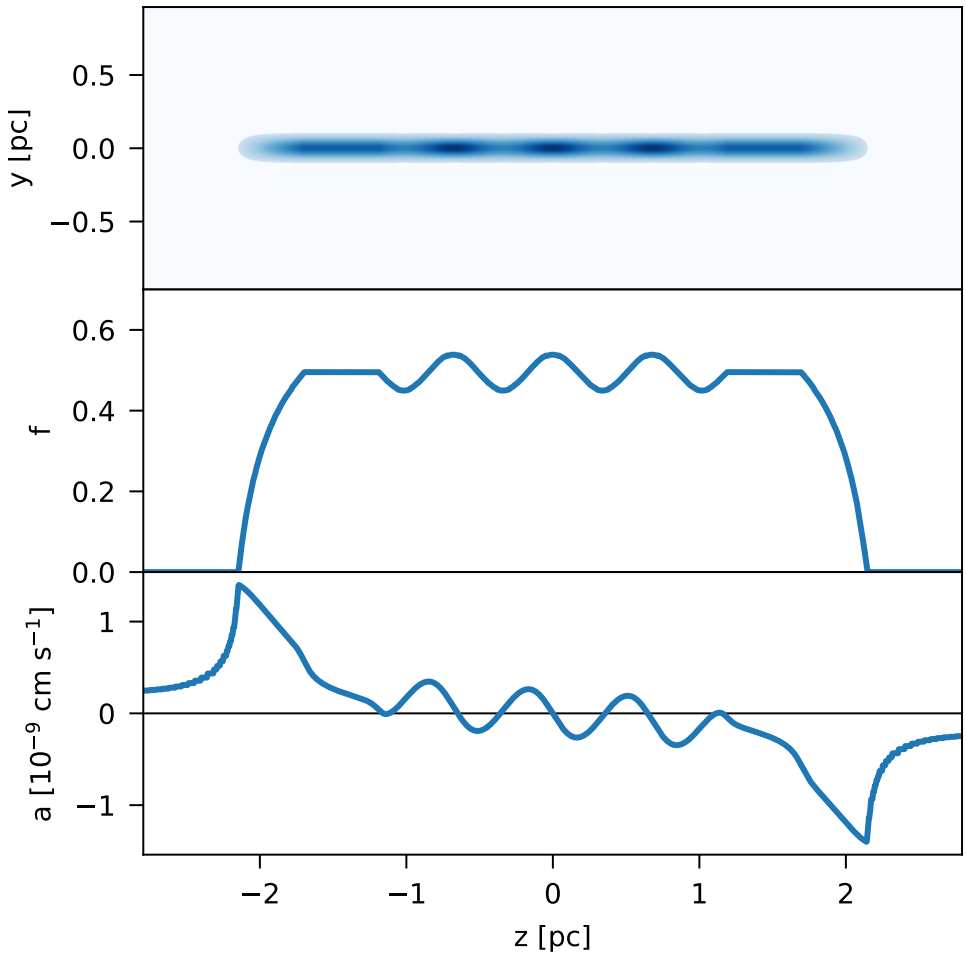

Figure 4.6: An exemplary simulation environment to validate the critical gradient, in this case with $R = 0.1\,\mathrm{pc}$, $f = 0.5$ and $dl/R = 6$. The upper part shows a section of a density slice, the second plot the criticality along the z-axes and the last one the gravitational acceleration along the z-axes. Inside the filament perturbations with $\epsilon = 0.09$ are set up followed by a flat profile in the end region and a linear density gradient, which in this example is $dl/R = 6$. Since there is a density cut to the ambient medium in the simulations at the filament boundary density ρ_b, the gradient is curved in the line-mass projection.

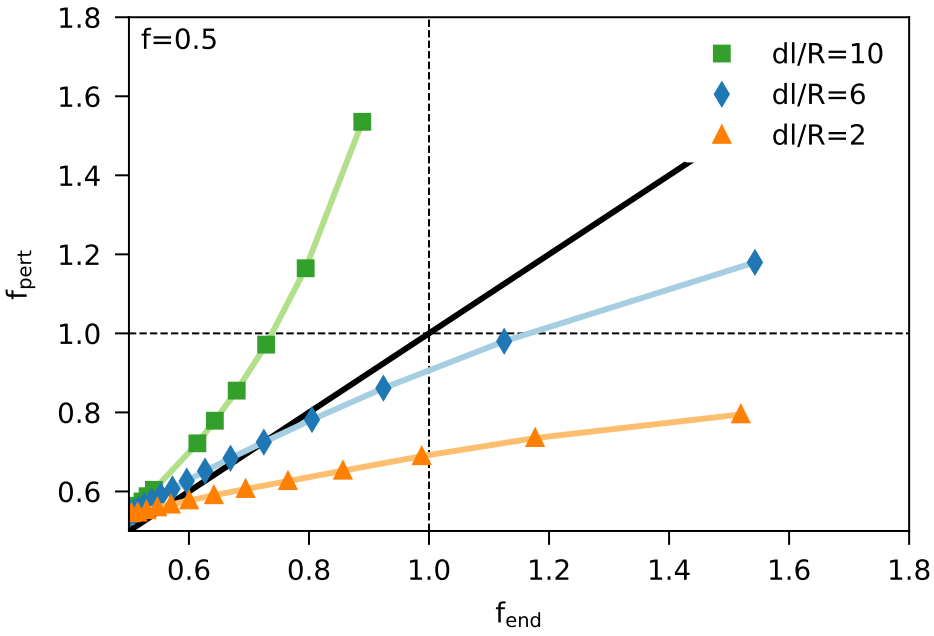

Figure 4.7: For simulations with $f = 0.5$, $R = 0.1\,\mathrm{pc}$ the evolution of the criticality for the end cores against the criticality of the perturbations are shown for 3 different gradients. All simulations start at $f_{\mathrm{pert}} = f_{\mathrm{edge}} = 0.5$ and move to larger maximal f-values with time. Each marker represents one simulation time-step ($\Delta t = 0.1\,\mathrm{Myr}$). Above the solid black line, perturbations grow faster in f than the edge. A clear edge effect can only be seen for $dl/R = 2$, for the others perturbations grow on similar timescales or faster, which fits the prediction.

effect is still dominant for density gradients above the critical one. This is due to the fact that we consider the density gradient to extend to zero in the analytic approach. However, we expect observed filaments to be constrained by an outside pressure. This is also the case in the simulations meaning that the gradient is cut off at a boundary density ρ_{b} which is in pressure equilibrium with the surrounding material (see Figure 4.9 dashed-dotted line). This leads to a loss in mass in the end region which increases the acceleration at the end and results in shorter collapse timescales than predicted. Since the acceleration can be considered constant during the edge formation, a deviation in acceleration has a stronger impact on longer timescales. Figure 4.8 shows an approximation of how a cut-off at the boundary density would influence the critical density gradient, given by the orange squares (the new acceleration used to determine t_{edge} is derived in Appendix 4.7 and given by Equation 4.63). This is only an approximation since a cut-off at the boundary density not only constrains the filament along its main axis but also reduces the radius gradually in the end region, as can be seen in Figure 4.6. This was not accounted for in the comparison of Figure 4.8. Thus, for low line-mass filaments, even shallower density gradients than predicted are necessary to suppress the edge effect. However, the linear gradient is a good first approximation, especially for filaments with $f \geq 0.4$.

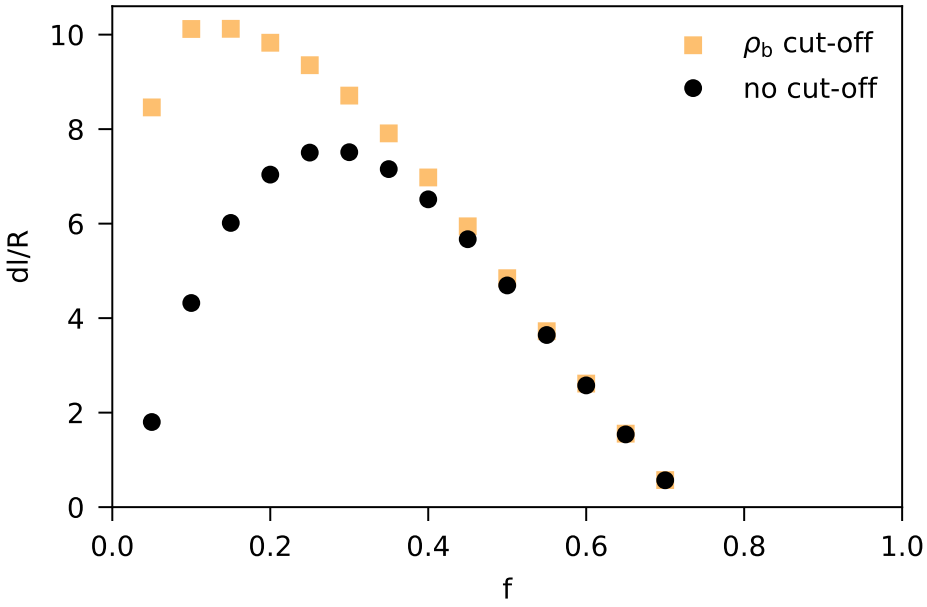

Figure 4.8: Critical gradient for a cut off at ρ_b given by the squares in light orange and the former solution without any cut off in comparison as black dots. For line-masses $f \geq 0.4$ the deviations are small. However, for lighter filaments, the estimation is not sufficient an much smoother gradients are necessary.

4.6 Discussion

For the calculation of the critical gradient, several approximations have been made. However, Figure 4.4 already showed a comparison between the numerical collapse times and the approximated collapse times. For the tested cases, which show a reasonable span over the parameter space of filaments the crossing point of the two timescales is approximated well. In addition, the determined curve of the critical gradient fits well with the numerically calculated curve (Figure 4.3). Although we observe a systematic deviation for filaments with lower aspect ratio A, which is expected due to the used approximation, the values do converge toward larger aspect ratios. However, the deviation is limited and can be interpreted as a transition region between the two effects. Thus, the approximations seem applicable to our case.

Whether the size of the end region dl is realistic is difficult to say. Although there are some observations of the line-mass distribution along filaments as Roy et al. (2015); Kainulainen et al. (2016); Cox et al. (2016); Yuan et al. (2020); Schmiedeke et al. (2021), the end region is often not displayed or not enough resolved to make a reasonable statement about the gradient. The best example is the observation of Barnard 5 by Schmiedeke et al. (2021). Here a clear linear trend is seen at the end of the filament. The declining region is of the order of $\sim 0.05\,\mathrm{pc}$, whereas the FWHM is $\sim 0.03\,pc$, thus, in this case, the end region is indeed bigger than the filament radius, which is needed for perturbations to be as fast as the edge effect in the parameter space we investigated. However, the filament is highly supercritical and thus, outside the range where our model is applicable. Further observations of filament end regions are necessary to make a reasonable comparison and

to test our prediction.

4.7 Conclusion

We showed that a density gradient at the end of a filament cannot stop the edge effect, since every kind of density gradient will cause a gradient in acceleration. The gradient will, however, only cause a weakening of the acceleration which leads to a longer edge effect formation timescale. But since the collapse timescale of a filament scales with the same respect to a the edge effect will take longer but will nevertheless occur before the collapse.

However, perturbations are independent of the acceleration at the end of the filament, and thus if the edge effect is slowed down significantly, perturbations can grow on similar timescales or even faster. Assuming the density gradient at the end of the filament to be linear, we presented the critical density gradient which is needed for perturbations to be dominant in the filament. For filaments beyond $f = 0.7$, perturbations always grow faster for the observed perturbation strength of 9% or larger. For lower line-mass filaments, an end region of several times the radius in length is needed to slow down the edge effect significantly, such that perturbations grow faster. However, deviations from the model are expected for $f < 0.4$ due to the approximations in the derivation of the critical gradient, where even shallower gradients would be needed. Altogether, density gradients at the end of the filament could be the reason, why the edge effect is only rarely observed. Observations are however needed to show whether such density gradients in end regions exist.

Acknowledgements

This research was supported by the Excellence Cluster ORIGINS which is funded by the Deutsche Forschungsgemeinschaft (DFG, German Research Foundation) under Germany's Excellence Strategy - EXC-2094 - 390783311. We thank the CAST group for the helpful discussion and comments, as well as the anonymous referee for the valuable feedback.

Appendix

4.A Derivation of the accelerations for different profiles and their gradients

Consider a uniform density distribution in the radial direction of the filament. The acceleration is determined by integrating over the density distribution:

$$a = G \int_0^R \mathrm{d}r \int_0^{2\pi} \mathrm{d}\theta \int_{\mathrm{Fil.}} \mathrm{d}z' \rho(z') \frac{r}{\sqrt{r^2 + z'^2}^2} \cos(\alpha) \tag{4.33}$$

$$= 2\pi G \int_0^R \mathrm{d}r \int_{\mathrm{Fil.}} \mathrm{d}z' \rho(z') \frac{r z'}{\left(r^2 + z'^2\right)^{3/2}} \tag{4.34}$$

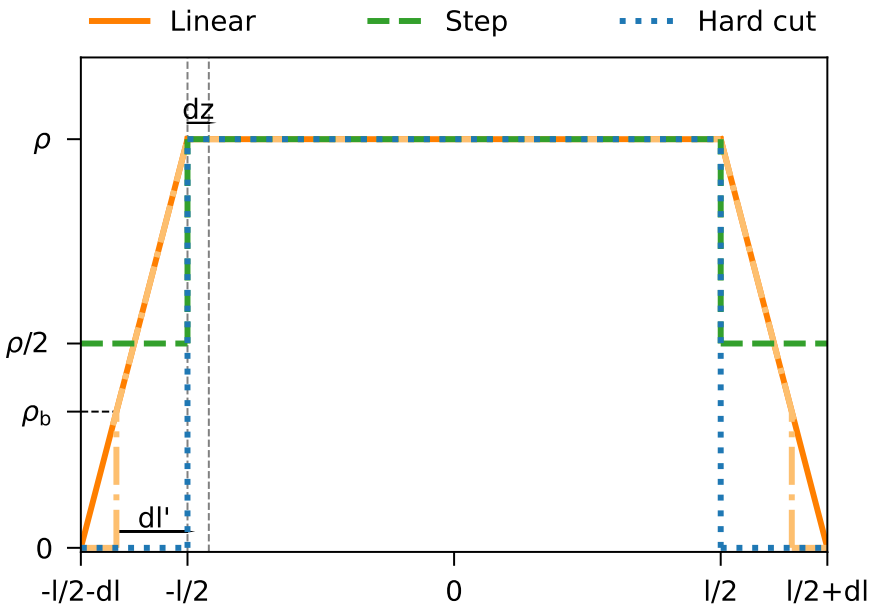

Figure 4.9: Schematic drawing of the density distribution for the three different configurations (linear, step and hard cut) of the end regions. In addition, the linear case with cut-off at the boundary density is indicated by the light orange dashed-dotted line.

Substitution $u = r^2$ $\frac{du}{dr} = 2r$

$$a = \pi G \int_0^{R^2} \mathrm{d}u \int_{\mathrm{Fil.}} \mathrm{d}z' \rho(z') \frac{z'}{(u + z'^2)^{3/2}} \tag{4.35}$$

$$= -2\pi G \int_{\mathrm{Fil.}} \mathrm{d}z' \rho(z') \left[\frac{z'}{\sqrt{R^2 + z'^2}} - \frac{z'}{\sqrt{z'^2}} \right]. \tag{4.36}$$

Since this function is not continuous at $z = 0$ the limits have to be adjusted.

4.A.1 Hard cut

For a hard cut-off, the density distribution is simple, see Figure 4.9 blue dotted line. Integrating Equation 4.36 leads to the acceleration from Burkert & Hartmann (2004):

$$a = -2\pi G\rho \left[\int_{-l/2-z}^{l/2-z} \mathrm{d}z' \frac{z'}{(R^2 + z'^2)^{1/2}} - \int_{-l/2-z}^{0} \mathrm{d}z'(-1) - \int_0^{l/2-z} \mathrm{d}z'(+1) \right] \tag{4.37}$$

$$= -2\pi G\rho \left[\sqrt{R^2 + (l/2 - z)^2} - \sqrt{R^2 + (l/2 + z)^2} + 2z \right]. \tag{4.38}$$

. Simple differentiation leads to the acceleration gradient:

$$\nabla a = -2\pi G\rho \frac{\mathrm{d}}{\mathrm{d}z} \left[\sqrt{R^2 + (l/2 - z)^2} - \sqrt{R^2 + (l/2 + z)^2} + 2z \right] \tag{4.39}$$

$$= -2\pi G\rho \left[-\frac{l/2+z}{\sqrt{R^2+(l/2+z)^2}} - \frac{l/2-z}{\sqrt{R^2+(l/2-z)^2}} + 2 \right]. \tag{4.40}$$

4.A.2 Step

For the step function integration over the density distribution given in Figure 4.9 by the green dashed line leads to the acceleration along such a filament

$$\begin{aligned} a = &-2\pi G \left[\int_{-l/2-dl-z}^{-l/2-z} \mathrm{d}z' \frac{\rho}{2} \left(\frac{z'}{(R^2+z'^2)^{1/2}} - 1 \right) \right. \qquad (4.41) \\ &+ \int_{-l/2-z}^{0} \mathrm{d}z' \rho \left(\frac{z'}{(R^2+z'^2)^{1/2}} - 1 \right) \\ &+ \int_{0}^{l/2-z} \mathrm{d}z' \rho \left(\frac{z'}{(R^2+z'^2)^{1/2}} + 1 \right) \\ &\left. + \int_{l/2}^{l/2+dl/2-z} \mathrm{d}z' \frac{\rho}{2} \left(\frac{z'}{(R^2+z'^2)^{1/2}} + 1 \right) \right] \qquad (4.42) \\ = &-2\pi G\rho \left[-\frac{1}{2}\sqrt{R^2+(l/2+z)^2} + \frac{1}{2}\sqrt{R^2+(l/2-z)^2} \right. \\ &\left. + 2z - \frac{1}{2}\sqrt{R^2+(l/2+dl+z)^2} + \frac{1}{2}\sqrt{R^2+(l/2+dl-z)^2} \right]. \qquad (4.43) \end{aligned}$$

From this the acceleration gradient follows as

$$\begin{aligned} \nabla a = &-2\pi G\rho \left[-\frac{1}{2}\frac{l/2+z}{\sqrt{R^2+(l/2+z)^2}} - \frac{1}{2}\frac{l/2-z}{\sqrt{R^2+(l/2-z)^2}} \right. \\ &\left. + 2 - \frac{1}{2}\frac{l/2+dl+z}{\sqrt{R^2+(l/2+dl+z)^2}} - \frac{1}{2}\frac{l/2+dl-z}{\sqrt{R^2+(l/2+dl-z)^2}} \right]. \end{aligned} \tag{4.44}$$

4.A.3 Linear

Calculating the acceleration gradient for a filament with a linear end region is a bit more complex than in the previous cases. Thus, we only calculated it for the exact end of the filament at $z = l/2$ building the difference quotient at location $-l/2$ and $-l/2 + dz$ as indicated by the grey dashed lines in Figure 4.9. The contribution of the linear part is given by integrating with a liner density distribution $\rho(z') = mz' + b$:

$$\begin{aligned} I(z') &= \int \mathrm{d}z'(mz'+b) \left(\frac{z'}{\sqrt{R^2+z'^2}} + 1 \right) \qquad (4.45) \\ &= \left[\frac{m}{2} \left(z'\sqrt{R^2+z'^2} - R^2 \tanh^{-1}\left(\frac{z'}{\sqrt{R^2+z'^2}} \right) \right) \right. \\ &\quad \left. + \frac{m}{2}z'^2 + b\sqrt{R^2+z'^2} + bz' \right] \qquad (4.46) \end{aligned}$$

$$= \left[\left(\frac{m}{2} z' + b \right) \left(\sqrt{R^2 + z'^2} + z' \right) - \frac{R^2 m}{2} \tanh^{-1} \left(\frac{z'}{\sqrt{R^2 + z'^2}} \right) \right]. \tag{4.47}$$

As before the contribution of the inner part is given by the acceleration of the constant-density filament:

$$a(z) = \rho \left[\sqrt{R^2 + \left(\frac{l}{2} - z \right)^2} - \sqrt{R^2 + \left(\frac{l}{2} + z \right)^2} + 2z \right]. \tag{4.48}$$

To determine the gradient of the acceleration we use these density distributions at the filaments end and dz infinitesimal shifted from the end:

$$\rho_1(z) = \rho \left(\frac{1}{dl} z + 1 \right), \tag{4.49}$$

$$\rho_2(z) = \rho \left(\frac{1}{dl} z + 1 + \frac{dz}{dl} \right). \tag{4.50}$$

Since we are only calculating the gradient for the end of the filament, the contributions from the other end can be neglected in this case, which leads to the following difference quotient:

$$\Delta a = \frac{2\pi G}{dz} \left[I|_{-dl}^{0} + a(-l/2) - I|_{-dl-dz}^{-dz} - a\left(-\frac{l}{2} + dz \right) \right] \tag{4.51}$$

$$\begin{aligned}
=& \frac{2\pi G\rho}{dz} \Bigg[R - \frac{1}{2} \left(\sqrt{R^2 + dl^2} - dl \right) + \frac{R^2}{2dl} \tanh^{-1} \left(\frac{-dl}{\sqrt{R^2 + dl^2}} \right) \\
&+ \sqrt{R^2 + l^2} - R - l - \left(\frac{-dz}{2dl} + 1 + \frac{dz}{dl} \right) \left(\sqrt{R^2 + dz^2} - dz \right) \\
&+ \frac{R^2}{2dl} \tanh^{-1} \left(\frac{-dz}{\sqrt{R^2 + dz^2}} \right) + \left(\frac{1}{2} + \frac{dz}{2dl} \right) \left(\sqrt{R^2 + (dl + dz)^2} \right. \\
&\left. - dl - dz \right) - \frac{R^2}{2dl} \tanh^{-1} \left(\frac{-dl - dz}{\sqrt{R^2 + (dl + dz)^2}} \right) - \sqrt{R^2 + (l - dz)^2} \\
&+ \sqrt{R^2 + dz^2} + l - 2dz \Bigg]
\end{aligned} \tag{4.52}$$

$$\begin{aligned}
=& \frac{2\pi G\rho}{dz} \Bigg[- \frac{1}{2} \sqrt{R^2 + dl^2} + \frac{dl}{2} + \frac{R^2}{2dl} \tanh^{-1} \left(\frac{-dl}{\sqrt{R^2 + dl^2}} \right) \\
&+ \sqrt{R^2 + l^2} - \frac{dz}{2dl} \sqrt{R^2 + dz^2} + \frac{dz^2}{2dl} - \sqrt{R^2 + dz^2} + dz \\
&+ \frac{R^2}{2dl} \tanh^{-1} \left(\frac{-dz}{\sqrt{R^2 + dz^2}} \right) + \frac{dz}{2dl} \sqrt{R^2 + (dl + dz)^2} - \frac{dz}{2} \\
&- \frac{dz^2}{2dl} + \frac{1}{2} \sqrt{R^2 + (dl + dz)^2} - \frac{dl}{2} - \frac{dz}{2} \\
&- \frac{R^2}{2dl} \tanh^{-1} \left(\frac{-dl - dz}{\sqrt{R^2 + (dl + dz)^2}} \right) - \sqrt{R^2 + (l - dz)^2}
\end{aligned}$$

$$+\sqrt{R^2+dz^2}-2dz\Bigg]. \tag{4.53}$$

The gradient is then given for $dz \to 0$:

$$\nabla a = \lim_{dz\to 0} \Delta a \tag{4.54}$$

$$=2\pi G\rho\left[\frac{\sqrt{R^2+dl^2}}{dl}-\frac{R}{dl}+\frac{l}{\sqrt{R^2+l^2}}-2\right]. \tag{4.55}$$

For determining the edge effect formation timescale for a linear end region (e.g. Figure 4.4, and the critical density gradient), the centre of mass acceleration is needed. The centre of mass of the end region is again considered as $-l/2+\kappa R/2$, so the density distribution is given by:

$$\rho_{\rm cm}(z) = \rho\left(\frac{1}{dl}+1+\frac{kR}{2dl}\right) \tag{4.56}$$

with this, the center of mass acceleration follows

$$a_{\rm cm} = -2\pi G\left[I|_{-\kappa R/2-dl}^{-\kappa R/2} + a\left(-\frac{l}{2}+\frac{\kappa R}{2}\right)\right] \tag{4.57}$$

$$\begin{aligned}
=&-2\pi G\rho_0\Bigg[\left(\frac{\kappa R}{4dl}+1\right)\left(\sqrt{R^2+(\kappa R/2)^2}-\frac{\kappa R}{2}\right)\\
&-\frac{R^2}{2dl}\tanh^{-1}\left(\frac{-\kappa R/2}{\sqrt{R^2+(\kappa R/2)^2}}\right)+\sqrt{R^2+(l-\kappa R/2)^2}\\
&-\sqrt{R^2+(\kappa R/2)^2}+2\left(-\frac{l}{2}+\frac{\kappa R}{2}\right)-\left(\frac{\kappa R}{4dl}+\frac{1}{2}\right)\\
&\left(\sqrt{R^2+(\kappa R/2+dl)^2}-\frac{\kappa R}{2}-dl\right)\\
&+\frac{R^2}{2dl}\tanh^{-1}\left(\frac{-\kappa R/2-dl}{\sqrt{R^2+(\kappa R/2+dl)^2}}\right)\Bigg]
\end{aligned} \tag{4.58}$$

$$\begin{aligned}
=&-2\pi G\rho_0\Bigg[\frac{\kappa R}{4dl}\sqrt{R^2+(\kappa R/2)^2}\\
&-\frac{R^2}{2dl}\tanh^{-1}\left(\frac{-\kappa R/2}{\sqrt{R^2+(\kappa R/2)^2}}\right)+\sqrt{R^2+(l-\kappa R/2)^2}-l\\
&+\kappa R-\left(\frac{1}{2}+\frac{\kappa R}{4dl}\right)\sqrt{R^2+(\kappa R/2+dl)^2}\\
&+\frac{dl}{2}+\frac{R^2}{2dl}\tanh^{-1}\left(\frac{-\kappa R/2-dl}{\sqrt{R^2+(\kappa R/2+dl)^2}}\right)\Bigg].
\end{aligned} \tag{4.59}$$

Approximation for $l-\kappa R/2 \gg R$ leads to

$$a_{\rm cm} = -2\pi G\rho\left[\frac{\kappa R}{4dl}\sqrt{R^2+(\kappa R/2)^2}-\frac{R^2}{2dl}\tanh^{-1}\left(\frac{-\kappa R/2}{\sqrt{R^2+(\kappa R/2)^2}}\right)\right.$$

$$+\frac{\kappa R}{2}-\left(\frac{1}{2}-\frac{\kappa R}{4dl}\right)\sqrt{R^2+(\kappa R/2+dl)^2}+\frac{dl}{2}$$
$$+\frac{R^2}{2dl}\tanh^{-1}\left(\frac{-\kappa R/2-dl}{\sqrt{R^2+(\kappa R/2+dl)^2}}\right)\Bigg]. \tag{4.60}$$

In order to compare the analytic model to simulations and observations, it has to be considered that filaments are surrounded by an outside pressure which cuts off the density profile at the pressure equilibrium at boundary density ρ_b. Thus, the linear profile only extends to dl' while still having a gradient of $m = \rho/dl$ (see light orange dashed-dotted line in Figure 4.9). The centre of mass acceleration is then determined by:

$$a_\mathrm{cm} = -2\pi G\left[I|_{-\kappa R/2-dl'}^{-\kappa R/2}+a\left(-\frac{l}{2}+\frac{\kappa R}{2}\right)\right] \tag{4.61}$$
$$\begin{aligned}
=&2\pi G\rho\Bigg[\left(\frac{\kappa R}{4dl}+1\right)\left(\sqrt{R^2+\left(\frac{\kappa R}{2}\right)^2}-\frac{\kappa R}{2}\right)\\
&-\frac{R^2}{2dl}\tanh^{-1}\left(\frac{\kappa R/2}{\sqrt{R^2+(\kappa R/2)^2}}\right)-\left(\frac{\kappa R}{4dl}-\frac{dl'}{2dl}+1\right)\\
&\left(\sqrt{R^2+\left(\frac{\kappa R}{2}+dl'\right)^2}-\frac{\kappa R}{2}-dl'\right)\\
&+\frac{R^2}{2dl}\tanh^{-1}\left(\frac{-\kappa R/2-dl'}{\sqrt{R^2+(\kappa R/2+dl')^2}}\right)\\
&+\sqrt{R^2+\left(l-\frac{\kappa R}{2}\right)^2}-\sqrt{R^2+\left(\frac{\kappa R}{2}\right)^2}-l+\kappa R\Bigg]
\end{aligned} \tag{4.62}$$
$$\begin{aligned}
=&2\pi G\rho\Bigg[\frac{\kappa R}{4dl}\sqrt{R^2+\left(\frac{\kappa R}{2}\right)^2}-\frac{R^2}{2dl}\tanh^{-1}\left(\frac{\kappa R/2}{\sqrt{R^2+(\kappa R/2)^2}}\right)\\
&-\left(\frac{\kappa R}{4dl}-\frac{dl'}{2dl}+1\right)\sqrt{R^2+\left(\frac{\kappa R}{2}+dl'\right)^2}-\frac{dl'^2}{2dl}+dl'\\
&+\frac{R^2}{2dl}\tanh^{-1}\left(\frac{-\kappa R/2-dl'}{\sqrt{R^2+(\kappa R/2+dl')^2}}\right)\\
&+\sqrt{R^2+\left(l-\frac{\kappa R}{2}\right)^2}-l+\kappa R\Bigg].
\end{aligned} \tag{4.63}$$

For $dl' = dl$ this turns into Equation 4.59 since then $\rho_\mathrm{b} = 0$.

Chapter 5

Paper IV – Merging filaments II: The origin of the tuning fork

Elena Hoemann, Andrea Socci, Stefan Heigl, Andreas Burkert and Alvaro Hacar, 2023, submitted to *Monthly Notices of the Royal Astronomical Society*

The observational analysis presented in Section 5.5 was performed by Andrea Socci.

We suggest that filaments in star-forming regions undergo frequent mergers. As stellar nurseries, filaments play a vital role in understanding star formation and mergers could pave the way for understanding the formation of more complex filamentary systems like networks and hubs. We compare hydrodynamic RAMSES simulations of merging filaments to an ALMA observation of the tuning fork-like split-up in the LDN 1641-North star-forming region in the Orion tail. We find similar features in line-mass, column density and velocity dispersion. This supports the hypothesis of filament mergers shaping the structure of the interstellar medium.

Keywords: stars:formation – ISM:kinematics and dynamics – ISM:structure

5.1 Introduction

Observations showed that the molecular interstellar medium is permeated by filamentary substructures. From isolated cylindrical structures (Palmeirim et al., 2013; Kainulainen et al., 2016; Yuan et al., 2020) to large filamentary networks (Peretto et al., 2013; Könyves et al., 2015) and hub systems (Myers, 2009; Schneider et al., 2010; Treviño-Morales et al., 2019), they are the dominant feature in star-forming regions. Filaments are hierarchical structures and span nine orders of magnitude in mass and five in length (Hacar et al., 2023) and it has been known for a long time that they are the places where stars are formed (Schneider & Elmegreen, 1979) since most of the prestellar cores are found within these cold, dense environments (Arzoumanian et al., 2011; Könyves et al., 2015).

In theoretical studies, filaments are often considered cylinders (Burkert & Hartmann, 2004; Clarke & Whitworth, 2015; Heigl et al., 2021; Hoemann et al., 2023a). However, observations also show much more complex structures (Peretto et al., 2013; Busquet et al., 2013; Hacar et al., 2013), since filaments are frequently observed in networks or hub constellations (Könyves et al., 2015; Kumar et al., 2020). Also on smaller scales in the substructure of the Orion Integral Shaped Filament (ISF, Bally et al., 1987) the ALMA observations by Hacar et al. (2018) revealed more complex structures: several small-scale filaments show a tuning fork-like shape where two separate branches join to one strand. It is not clear how such structures are created and how they evolve. We suggest that these tuning forks are the result of filament mergers. Similar to Nakamura et al. (2014) who proposed that Serpens South was created due to a collision of three filaments.

In our first paper about merging filaments (Hoemann et al., 2021) we already discussed that filaments can only merge under special initial conditions before they collapse or create end cores. However, in our most recent paper (Hoemann et al., 2023b) we found, that a density gradient at the end of the filament can slow down the end-dominated collapse. This opens more possibilities for filaments to merge.

In this paper, we show that hydrodynamic simulations of filament mergers can recreate the observed tuning fork structures and trigger star formation in the merged region. We present characteristic features which identify a tuning fork as a merger and which distinguish it from other creation mechanisms. If the two filaments are separated along the line of sight a projection effect mimicking a tuning fork could be an alternative explanation, or that the tuning fork originated from one structure which broke apart. In addition, we present an example observation of a tuning fork observed with ALMA in LDN 1641-North which is part of the Orion A tail. Hosting about a dozen of young stars and protostars, also in the vicinity of the tuning fork, it is a good target to investigate the early phases of star formation. In comparison to the simulations, we find indications that the observed tuning fork structure in LDN 1641-North is a merged filament. However, this needs to be validated by further studies.

5.2 Basic Principles

Stodólkiewicz (1963) and Ostriker (1964) found that filaments in hydrostatic equilibrium

follow this radial density profile:

$$\rho(r) = \rho_{\rm c} \left[1 + \left(\frac{r}{H}\right)^2\right]^{-2}, \tag{5.1}$$

where $\rho_{\rm c}$ is the central density and H the scale height of the filament

$$H^2 = \frac{2c_{\rm s}^2}{\pi G \rho_{\rm c}}, \tag{5.2}$$

with G being the gravitational constant and $c_{\rm s}$ the sound speed which is $0.19\,{\rm km\,s^{-1}}$ in a medium of 10 K and a molecular weight of 2.36. This radial profile is confined by the pressure of the surrounding interstellar medium $P_{\rm ext} = P_{\rm b}$ at boundary density $\rho_{\rm b}$. The line-mass is then defined as the mass confined in the filament divided by its length:

$$\mu = \frac{M}{l}. \tag{5.3}$$

There exists an upper line-mass limit for which a filament can be in hydrostatic equilibrium. Integrating Equation 5.1 radially till infinity, gives the critical line-mass above which no hydrostatic solution can be found

$$\mu_{\rm crit} = \frac{2c_{\rm s}^2}{G} \approx 16.4\,{\rm M_\odot\,pc^{-1}}. \tag{5.4}$$

The criticality (Fischera & Martin, 2012) is then defined as the ratio between the line-mass of a filament and its critical line-mass

$$f = \frac{\mu}{\mu_{\rm crit}}. \tag{5.5}$$

The criticality then determines the density at the boundary

$$\rho_b = \rho_{\rm c}(1 - f)^2 \tag{5.6}$$

and the corresponding radius of the filament

$$R = H \left(\frac{f}{1 - f}\right)^{1/2}. \tag{5.7}$$

5.3 Simulations

We did simulations with the adaptive-mesh-refinement code RAMSES (Teyssier, 2002) to validate our analytic predictions and to perform comparisons to observations (respectively in Section 5.4 and Section 5.5). In RAMSES a second-order Gudonov solver is used to solve the Euler Equations in their conservative form, applying the MUSCL (Monotonic Upstream-Centered Scheme for Conservation Laws, van Leer, 1979), the HLLC-Solver (Harten-Lax-van Leer- Contact, Toro et al., 1994) and the MC slope limiter (monotonized central-differenc, van Leer, 1979).

Two different kinds of simulations were performed. On the one hand, we executed simulations of infinite long filaments to validate the model of the merging process, described in Subsection 5.4.1. On the other hand, we show simulations of mergers with finite filaments to recreate tuning forks, shown in Subsection 5.4.2.

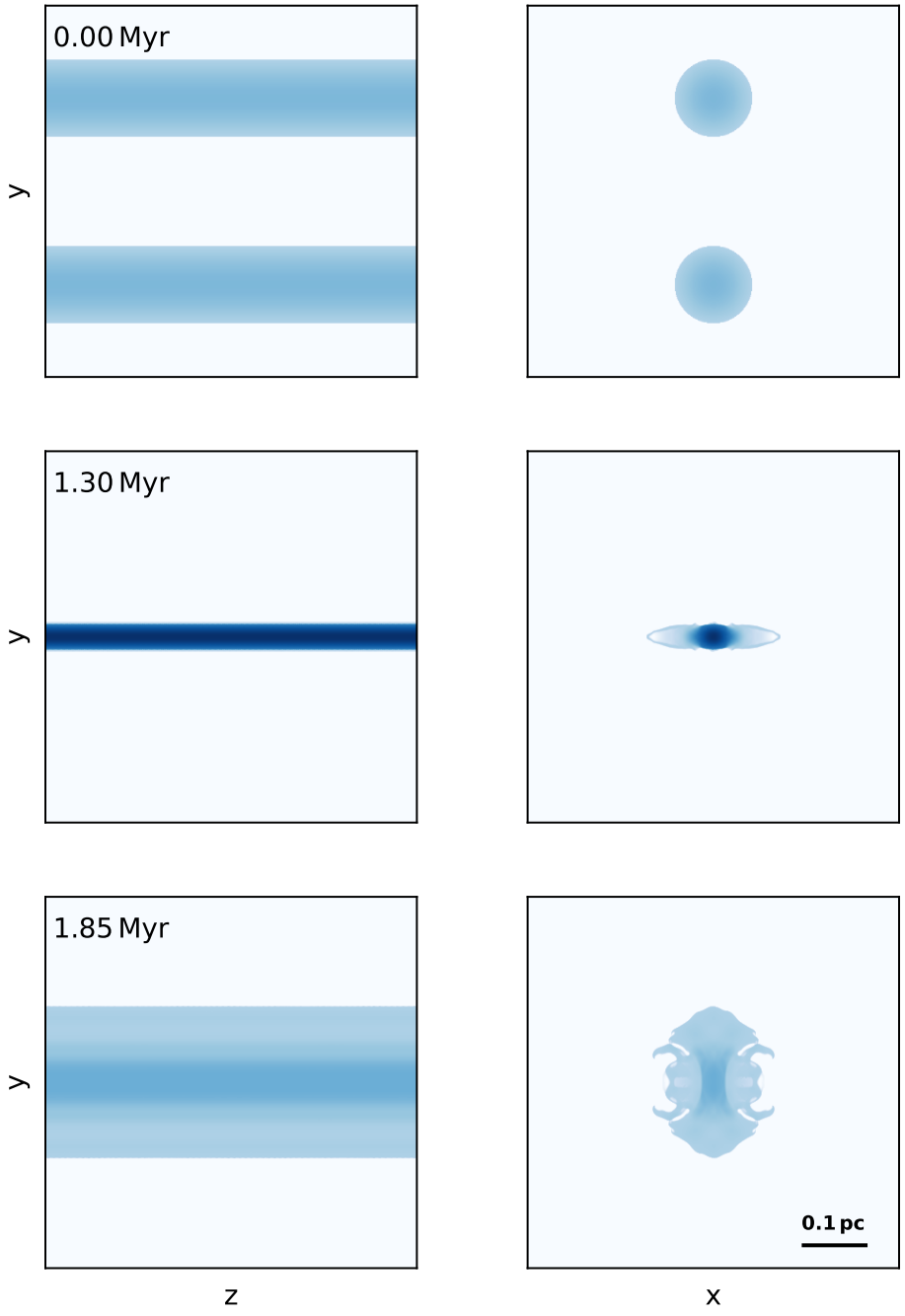

Figure 5.1: Three density cuts of the simulation of the merger of infinite filaments for different timesteps indicated by the time given in the upper left corner. The simulations were performed with the follwoing parameters: $f_1 = f_2 = 0.3$, $v_0 = 0.0\,\mathrm{km\,s^{-1}}$, $d_0 = 0.3\,\mathrm{pc}$. The left-hand side shows the merger face-on, whereas the right-hand side shows a cut through the merger. The three different time steps are chosen as the initial conditions, the highest compression in y-direction and its first relaxation. This shows the oscillatory pattern of the merger.

5.4 Theory of merging filaments

Already in our first paper, Hoemann et al. (2021), we discussed the theory of merging filaments. We found that special initial conditions are necessary for filaments to merge before they collapse. Since the timescale on which filaments merge

$$t_{\mathrm{merge}} = \sqrt{\frac{\pi}{G(\mu_1+\mu_2)}}\frac{d_0}{2}, \tag{5.8}$$

with μ_1, μ_2 being the line-masses of the filaments and d_0 their initial distance, is on the same order of magnitude as their collapse time (Clarke & Whitworth, 2015; Hoemann et al., 2023a). However, we showed in Hoemann et al. (2023b) that density gradients at the ends of the filament can slow down the collapse, which makes the merger much more probable.

In the following, we will go into more detail about how a merger evolves for finite and infinite filaments, respectively.

5.4.1 Infinite filaments - oscillatory pattern

In order to investigate the evolution of a filament merger, we start from the same initial condition as in our first paper: two parallel filaments with a distance d_0 in a box with periodic boundary conditions along the filament and open boundaries perpendicular to the filament's main axis. The evolution of the simulation is depicted in Figure 5.1. The left column shows density cuts in the z-y plane and the right column in the x-y plane. The initial conditions are given in the first row. As the simulation evolves, the filaments fall into each other's potential and merge. The highest compression along the y-axis is given in the second row and the third shows the maximum relaxation in the y direction. This oscillation around their common centre of mass is long-lived and depends on the initial condition of the merger. A similar behaviour is seen in recent 2D MHD simulations of merging filaments by Kashiwagi et al. (2023), showing oscillatory patterns for magnetically subcritical filaments.

The first oscillation can be described by adding a drag term to the gravitational acceleration as the two filaments start to overlap:

$$a = -\frac{2G\mu(r)}{r} - bv^2\rho(r). \tag{5.9}$$

The dependency of $\mu(r)$ means the enclosed line-mass within r (derivation in Appendix 5.7)

$$\mu(r) = \mu_{crit}\left[1 - \left(1 + \frac{r^2}{H^2}\right)^{-1}\right], \tag{5.10}$$

whereas $\rho(r)$ represents the density at position r and the free parameter b is fitted to the simulation. An example is given in Figure 5.2: the model for the radius evolution is given by the solid blue line in the top panel. It fits well to the first oscillation period of the simulation in y-direction displayed by the light blue dots. At later times, the pattern gets too messy to predict. Since observers can only detect the line of sight

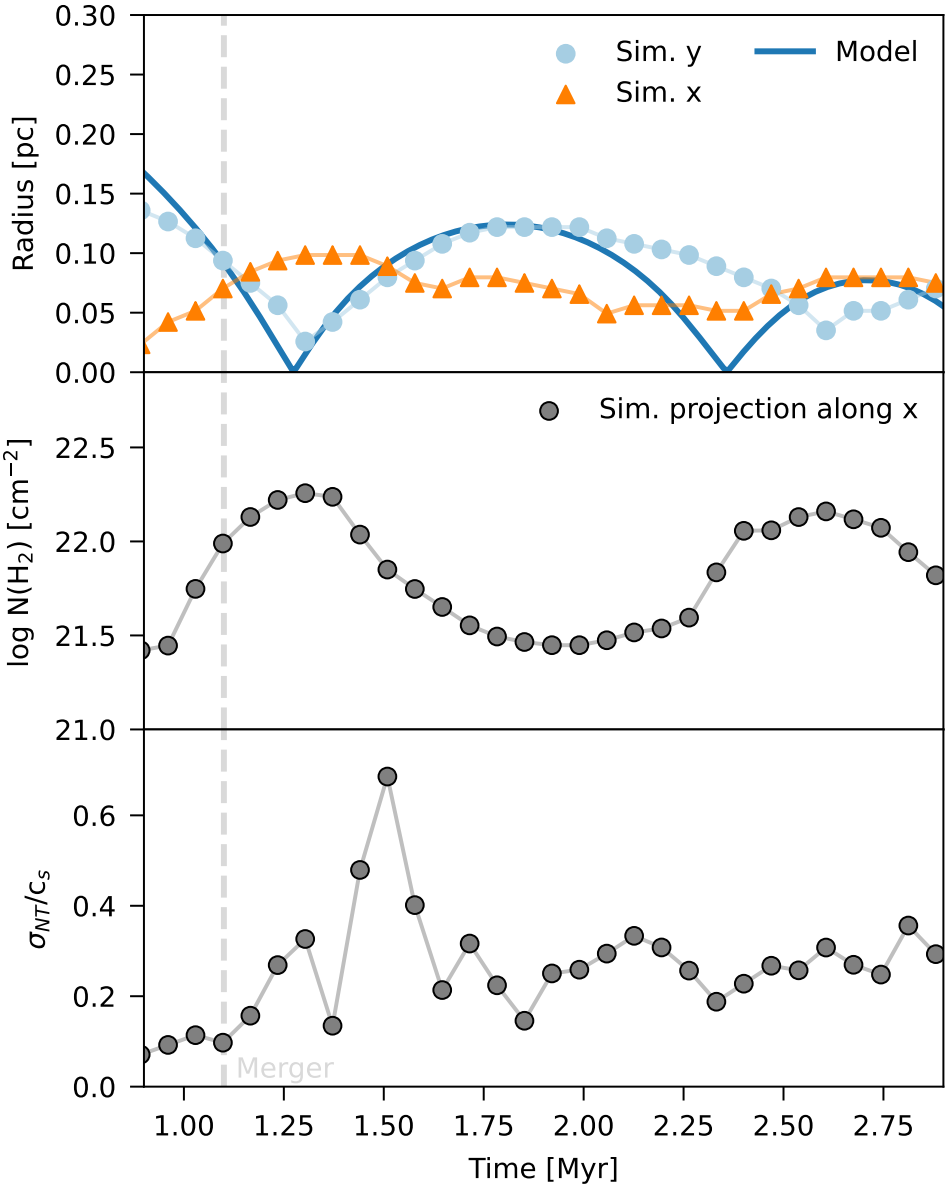

Figure 5.2: Time evolution of Radius, column density and the mach number of the simulation of two merging filaments with $f_1 = f_2 = 0.3$, $d_0 = 0.3\,\mathrm{pc}$ and no initial velocity. The top panel shows the radius evolution where the proposed model is given by the blue line (parameter $b = 4 \times 10^{-3}\,\mathrm{pc}^2\,\mathrm{M}_\odot{}^{-1}$) and the simulated values by the light blue dots. As observations can only detect the movement along the line of sight, the component in the y direction is given by the orange triangles as a comparison. The two lower panels show the corresponding quantities in projection along the x-axis, the line of sight in this example.

velocity, the oscillation in z-direction is plotted in orange for comparison. Especially for the first oscillation the two phases are shifted by half a period. Thus, when the highest compression in the z-direction appears, the radius in the y-direction is maximally extended, followed by a maximal extension in the z-direction. This leads to alternating peaks in column density and velocity dispersion, displayed in the two lower panels. These quantities can be observed since they are measured along the line of sight (x-axis) where the gas is either compressed, meaning a high column density, or relaxing, seen as a peak in velocity dispersion.

To approximate the maximum velocity which can be observed in a merger, we use energy conservation between the initial and final state, assuming dissipative losses are small:

$$E_{\mathrm{pot,i}} + E_{\mathrm{kin,i}} = E_{\mathrm{kin,f}}. \tag{5.11}$$

The potential energy for infinite filaments is given by (derivation in Appendix 5.7):

$$E_{\mathrm{pot}}(r) = 2Gm \left[\mu \log\left(\frac{r^2}{R^2}\right) + \mu_{\mathrm{crit}} \log\left(\frac{R^2}{H^2} + 1\right) \right], \tag{5.12}$$

considering $\mu_1 = \mu_2 = \mu$. This leads to the maximal velocity which can be reached during the merger:

$$v_{\mathrm{max}} = \sqrt{4G \left[2\mu \log\left(\frac{d_0}{R}\right) + \mu_{\mathrm{crit}} \log\left(\left(\frac{R}{H}\right)^2 + 1\right) \right] + v_0^2}, \tag{5.13}$$

with v_0 the initial velocity. Altogether, with this simple model, some characteristics as the maximal velocity and the radius evolution for the first oscillation can be predicted.

5.4.2 Finite filaments - tuning forks

As depicted in Figure 5.3 the merger of two inclined, finite filaments leads to a tuning fork-shaped structure. The figure shows three different snapshots of the column density from the simulation at 0.00, 0.18 and 0.27 Myr. On the left-hand side, the initial conditions are shown. As expected the filaments merge, forming a tuning fork-shaped structure reminiscent of those observed in the ISF (e. g., OMC-1 ridge, OMC-2 FIR 6, see Hacar et al., 2018). Since the ends on the left side merge first before the right part, the tuning fork shows the time evolution of the merger with infinite filaments along the merger. This is shown in Figure 5.4 where the blue line indicates the evolution of the radius predicted by the model. Thus, on the right-hand side, the filaments have not merged yet, the highest contraction along the y-axis is reached at about -0.1 pc and relaxation happens then to the left. The dashed green line shows the distance of the filaments in the simulation where they do not overlap yet. The light blue dots then show the radius evolution along the filament in the already merged regions. The simulation is well reproduced by the model discussed in Section 5.4.1. Therefore, you would also expect peaks in the column density and the velocity dispersion due to the oscillation happening along the merger. In addition to the fact that the sum of the respective line-masses should match the one of the merged region, these can be used as indications in observations to determine merged filaments.

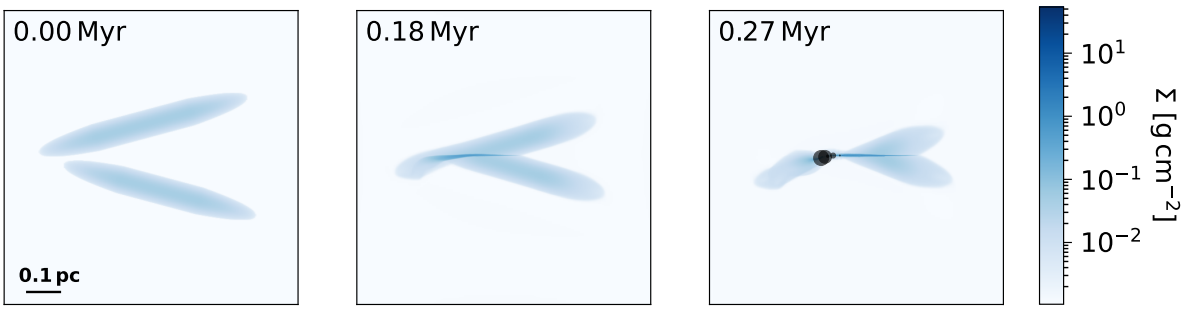

Figure 5.3: Evolution of two merging filaments, creating a tuning fork-like structure as observed in Orion. Three snapshots in time are given, depicting the column density of the merger as indicated by the colour bar. The filaments both have a criticality of $f = 0.6$, their initial velocity is $v_0 = 0.7\,\mathrm{km\,s^{-1}}$ and $l_1 = 0.25\,\mathrm{pc}$, $l_2 = 0.3\,\mathrm{pc}$, $\rho_b = 4.7 \times 10^{-20}\,\mathrm{g\,cm^{-3}}$, $d_0 = 0.2\,\mathrm{pc}$.

The merging of filaments is not only important to understand the structure formation in the interstellar medium but also for their fragmentation. Since the overlapping region can become supercritical filament merger can trigger core formation. This creates cores aligned along the merger as depicted in Figure 5.3 which shows the column density of the merged filament and the formed sink particles as circles whose size scales with their mass. The core formation is not as ordered as perturbation theory predicts. The pattern is much more messy and due to the dynamics of the system, cores also merge frequently. In this example, the core at the first overlapping point is created earliest and afterwards merges with several of the later formed cores and is therefore the most massive one. Mergers with flatter angles seem to produce more cores since the over-dense area is larger than for a more inclined merging angle.

In conclusion, finite filaments can produce tuning fork shapes due to merging. They undergo long-lived oscillations which produce characteristic features in the velocity dispersion and column density. In addition, chaotic core formation can be triggered along the merger.

5.5 Comparison to observations

We also searched for the aforementioned characteristic signatures in ALMA observations of the ISF where several tuning fork-like structures are observed. For our comparison, we chose the LDN 1641-North in the Orion A tail because it seems to be a good candidate for a merging filament since it shows a clear, isolated tuning fork-shaped structure. Figure 5.5 shows ALMA 12 m observations (Project: 2019.1.00641.S) combined with IRAM 30 m observations of N_2H^+(1-0) as tracer of the distribution of the dense gas ($> 1 \times 10^5\,\mathrm{cm^{-3}}$) along the LDN 1641-North region (a full description of the data reduction and combination is included in Hacar et al. 2023, in prep.). A final resolution of $\theta_{\mathrm{FWHM}} = 4.5$" is reached. It is a star-forming region within the Orion A molecular cloud complex located at an average distance of $414 \pm 7\,\mathrm{pc}$ (Menten et al., 2007) (this value is used for the following analysis). LDN 1641-North is an active star-forming region forming a small

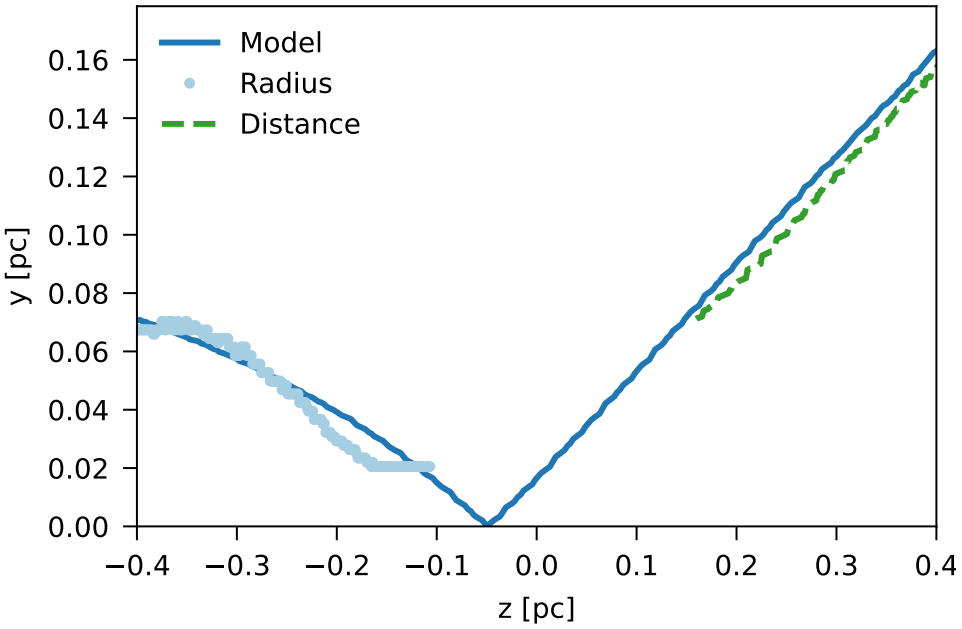

Figure 5.4: The distance (green dashed line) and radius (light blue dots) of a tuning fork simulation are depicted in comparison to the corresponding model calculations represented by the blue line, using the same value for $b = 4 \times 10^{-3}\,\mathrm{pc^2\,M_\odot{}^{-1}}$ as in the previous section. The simulation was done with the following parameters: $l_1 = 0.55\,\mathrm{pc}$, $l_2 = 0.75\,\mathrm{pc}$, $\rho_b = 4.7 \times 10^{-20}\,\mathrm{g\,cm^{-3}}$, $f_1 = f_2 = 0.3$, $v_0 = 0.7\,\mathrm{km\,s^{-1}}$ and $d_0 = 0.22\,\mathrm{pc}$. The model reproduces the simulated merger well.

cluster including 13 Class 0/I (aka protostars; cyan triangles in Figure 5.5) and more than 30 Class II (not shown) within the central parsec at the northern end of this cloud (Megeath et al., 2012, 2016). A small cluster is forming at the tuning fork which shows that it is an actively star forming region. In the subplot of Figure 5.5 a zoom onto the tuning fork structure is given. The axes were manually drawn following the high crest of the H_2 column density map derived from the N_2H^+ emission following a similar method that the one described in Hacar et al. (2018). They were centred by making cuts of the length of the beam size divided by 2 and determining the average coordinates in the cut by weighting the column density to the power of 4. The properties in each position were then extracted by sampling over the axis pixel-by-pixel and taking the average for each cut.

As a first indicator of a merger, we determine if the line-masses of both filaments add up in the merged region. Using the column density map of H_2 the mass can be calculated for each pixel. The sum of the pixels associated to one structure divided by its length is the corresponding line-mass which we derived for the merged part and both unmerged parts of the tuning fork: The blue non-merged part has a line mass of $\mu_{\mathrm{blue}} = 75\,\mathrm{M_\odot\,pc^{-1}}$, the orange non-merged part $\mu_{\mathrm{orange}} = 86\,\mathrm{M_\odot\,pc^{-1}}$ and the merged part $\mu_{\mathrm{junction}} = 176\,\mathrm{M_\odot\,pc^{-1}}$ which is in good agreement with the sum of the non-merged regions.

From theory and simulation, we expect an oscillation between column density and velocity dispersion, as was shown in the previous section. Figure 5.6 shows a comparison

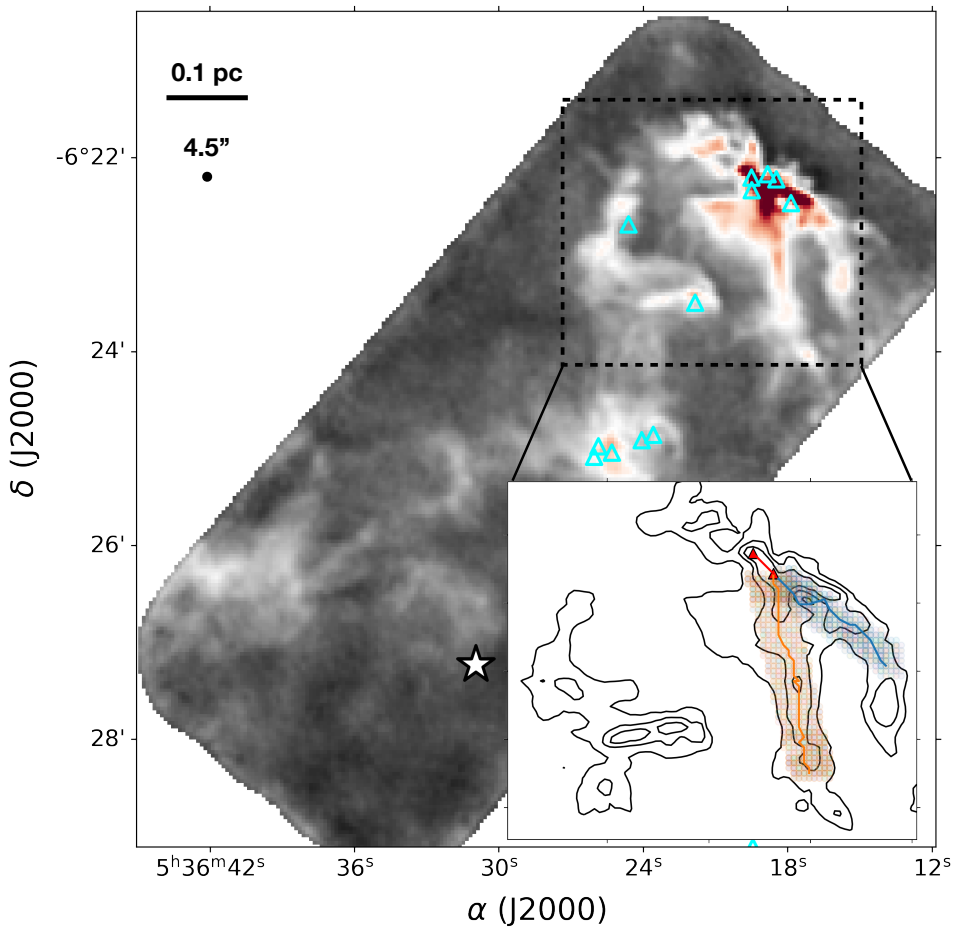

Figure 5.5: N_2H^+(1-0) map of LDN 1641-North as observed by ALMA (Project: 2019.1.00641.S). The triangles represent the young stars in the region given by Megeath et al. (2016). A zoom onto the tuning fork is given in the subplot. The coloured regions are the extracted filaments, defined by their main axis given by the corresponding coloured lines. The red line marks the potentially merged region.

between the observation in LDN 1641-North and our simulation. The example simulation was done with filaments with a length of $l_1 = l_2 = 0.7\,\mathrm{pc}$, a criticality of $f_1 = f_2 = 0.4$, an initial distance of $d_0 = 0.07\,\mathrm{pc}$, a velocity of $v_0 = 0.3\,\mathrm{km\,s^{-1}}$ and a boundary density of $\rho_b = 3.92 \times 10^{-19}\,\mathrm{g\,cm^{-3}}$. The merged region is marked in red and indeed both show peaks in column density and velocity dispersion, as expected. This could be a hint, that the structure in LDN 1641-North is indeed a merged filament. The order of magnitude of velocity dispersion and column density are also well reproduced by the example simulation.

5.6 Discussion

The similarity of our simulation and the observation in LDN 1641-North indicates that the tuning fork structure could be created due to filament mergers. If the tuning fork

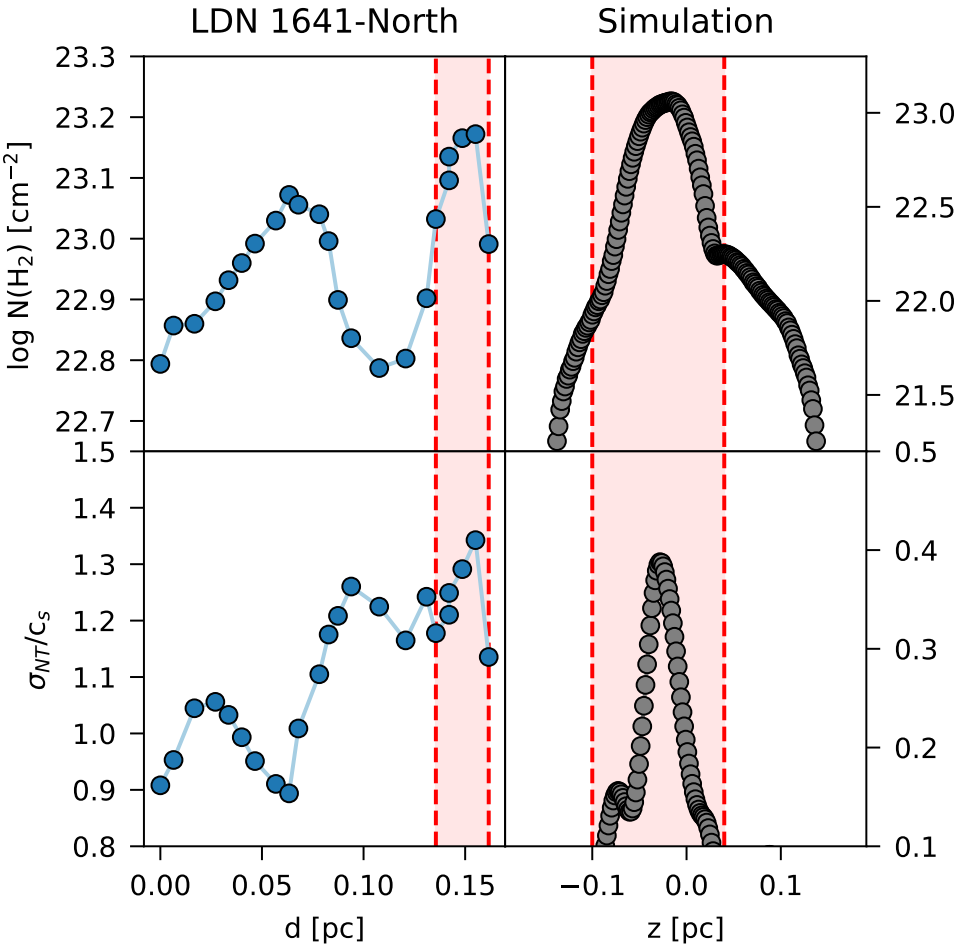

Figure 5.6: The column density and the mach number are displayed in the top and bottom panel respectively. The left-hand side shows the observed values along the blue axes in LDN 1641-North defined in Figure 5.5. The red area determines the potentially merged part. It indicates signatures of merged filaments: peaks in column density and velocity dispersion. In comparison an example from the simulation is depicted showing a similar pattern with parameters: $l_1 = l_2 = 0.07\,\mathrm{pc}$, $f_1 = f_2 = 0.4$, $d_0 = 0.07\,\mathrm{pc}$, $v_0 = 0.3\,\mathrm{km\,s^{-1}}$ and $\rho_b = 3.92 \times 10^{-19}\,\mathrm{g\,cm^{-3}}$.

features were just projection effects or originated from one structure we would not expect the peaks in column density and velocity dispersion. However, this is not final proof since also other phenomena, as collapsing cores, could lead to similar data. Further observations have to show whether other structures also show these indicators.

If there was a perfect compression and relaxation along the tuning fork the peak in column density and velocity dispersion would be shifted since the peak in column density represents the highest contraction along the line of sight and the velocity dispersion the following relaxation, as indicated in Figure 5.2. In the simulation, a minimal shift is present, whereas the resolution of the observation is not sufficient to capture this. The inclination between the merging parts could influence the separation of the peaks since this determines the gradient in initial conditions.

In addition, these merges could lead to a different core spacing, since the cores are created by the merger and not by initial perturbations. Our simulation showed a chaotic distribution of cores undergoing a lot of merges. Further studies should address the triggered core formation in merging filaments and what role perturbation theory plays in that regard. It would be interesting to address whether mergers can lead to any structured core formation and whether they can create more massive cores, as observations detect in hub filamentary systems (Peretto et al., 2013; Kumar, M. S. N. et al., 2022; Hacar et al., 2023).

Already in the first paper we discussed, that initial velocities increase the probability of filaments to merge before collapsing. However, the escape velocity sets an upper limit for filaments mergers:

$$v_{\mathrm{escape}} = \sqrt{4G\left(2\mu \log\left(\frac{d_0}{R}\right) + \mu_{\mathrm{crit}} \log\left(\left(\frac{R}{H}\right)^2 + 1\right)\right)}, \tag{5.14}$$

again considering $\mu_1 = \mu_2 = \mu$. For a filament with $f = 0.3$ and $R = 0.04\,\mathrm{pc}$ this would result in $v_{\mathrm{escape}} = 0.67\,\mathrm{km\,s^{-1}}$. Below this velocity, filaments merge alone due to gravity. Above, it is rather unlikely for them to merge having a random velocity orientation, since their paths have to cross. In this case, outer dynamics would need to influence the movement of the filament. This could happen due to magnetic fields, an outside gravitational potential or shock fronts for example.

5.7 Conclusion

Filament mergers produce tuning fork-like structures. These induce long-lived oscillations which can be observed through peaks in column density and velocity dispersion together with an increase in line-mass in the merged region. Observations with ALMA of the LDN 1641-North region in Orion show the expected sum in line mass and similar characteristic features in velocity dispersion and column density, indicating that the tuning fork-shaped filament could indeed be produced by a merger.

Acknowledgements

This research was supported by the Excellence Cluster ORIGINS which is funded by the Deutsche Forschungsgemeinschaft (DFG, German Research Foundation) under Ger-

many's Excellence Strategy - EXC-2094 - 390783311. We thank the CAST group for the helpful discussion and comments. AS and AH received funding from the European Research Council (ERC) under the European Union's Horizon 2020 research and innovation programme (Grant agreement No. 851435). This paper makes use of the following ALMA data: ADS/JAO.ALMA#2019.1.00641.S. ALMA is a partnership of ESO (representing its member states), NSF (USA) and NINS (Japan), together with NRC (Canada), MOST and ASIAA (Taiwan), and KASI (Republic of Korea), in cooperation with the Republic of Chile. The Joint ALMA Observatory is operated by ESO, AUI/NRAO and NAOJ. This work is based on IRAM-30m telescope observations carried out under project numbers 120-20 and 133- 22. IRAM is supported by INSU/CNRS (France), MPG (Germany), and IGN (Spain).

Appendix

5.A Derivation of the enclosed line-mass

To calculate the enclosed mass we integrate the Ostriker profile for $r < R$ otherwise $\mu(r) = \mu$

$$\mu(r) = \int_0^r \mathrm{d}r' \int_0^{2\pi} \mathrm{d}\theta \rho_c \left[1 + \left(\frac{r'}{H}\right)^2\right]^{-2} r'. \tag{5.15}$$

Substituting $u = \frac{r'^2}{H^2}$, $\frac{\mathrm{d}u}{\mathrm{d}r'} = \frac{2r'}{H^2}$ leads to

$$\begin{aligned}\mu(r) &= \pi H^2 \rho_c \int_0^{r^2/H^2} \mathrm{d}u (1+u)^{-2} \\ &= \pi H^2 \rho_c (-1) \cdot (1+u)^{-1} \Big|_0^{r^2/H^2} \\ &= \mu_{crit} \left[1 - \left(1 + \frac{r^2}{H^2}\right)^{-1}\right],\end{aligned} \tag{5.16}$$

with $\mu_{crit} = \frac{2c_s^2}{G}$ and $H^2 = \frac{\mu_{crit}}{\pi\rho_c}$.

5.B Derivation of the potential energy

We derive the potential energy for $\mu_1 = \mu_2 = \mu$

$$\begin{aligned}E_{pot}(r) &= \int_0^r \mathrm{d}r' F_G = \int_0^r \mathrm{d}r' m\ddot{r}' \\ &= \int_0^r \mathrm{d}r' 2\mu(r') m \frac{2G}{r'}.\end{aligned} \tag{5.17}$$

For $|r| > R$ this leads to

$$E_{pot}(r) = 4Gm \left[\int_R^r \mathrm{d}r' \frac{1}{r'} \cdot \mu + \int_0^R \mathrm{d}r' \frac{1}{r'} \cdot \mu_{crit} \left[1 - \left(1 + \left(\frac{r'}{H} \right)^2 \right)^{-1} \right] \right].$$

The potential energy is then given by:

$$E_{pot}(r) = 2Gm \left[\mu \log \left(\frac{r^2}{R^2} \right) + \mu_{crit} \log \left(\frac{R^2}{H^2} + 1 \right) \right]. \tag{5.18}$$

Chapter 6

Project – Multi-scale machine learning for column density factors in turbulent flows

Elena Hoemann, Miles Cranmer, Shirley Ho, Stefan Heigl, Kai Widmaier and Andreas Burkert, 2022, summer project at the Center for Computational Astrophysics at the Flatiron Institute in New York City

Chemical tracers are essential for simulations of the interstellar medium as they are needed for the correct description of heating and cooling. However, evolving a chemical network is computationally expensive for many reasons. One major bottleneck is for instance the attenuation of external UV-irradiation for which the local column density has to be determined. In order to circumvent this calculation we present a machine learning approach to determine column density factors using a U-Net which aims at reducing the cost of hydrodynamic simulations. Indeed, we show that the network is able to calculate column density factors and the speedup factor compared to the conventional method is approximately six. Nevertheless, further work has to be done to improve the accuracy and to adapt it to a real use case.

6.1 Introduction

The gas and dust located between the stars is called the interstellar medium (ISM). In its coldest regions, with temperatures of several Kelvin, molecules form and dense filaments are observed which are the sites where stars form (Schneider & Elmegreen, 1979; André et al., 2010; Könyves et al., 2015).

In order to determine the dynamics of these filaments, their collapse and the formation of prestellar cores, hydrodynamic simulations are performed (Smith et al., 2014; Clarke & Whitworth, 2015; Hoemann et al., 2021; Heigl et al., 2021). For more realistic modelling and comparison to observations, it is necessary to employ a chemical network (e. g. KROME Grassi et al. (2014) and GRACKLE Smith et al. (2017)), which traces the formation and evolution of different molecules (Walch et al., 2015; Anathpindika & Francesco, 2021) and determines the local heating and cooling rates.

As the chemistry strongly depends on external UV irradiation, the surrounding density structure is important to the evolution of the local cell. Accounting for this is computationally very expensive, as for every cell the surrounding structure must be evaluated which is currently done by ray tracing approaches (e. g. Razoumov & Scott, 1999; Abel et al., 1999; Raga et al., 1999; Razoumov & Cardall, 2005; Cantalupo & Porciani, 2011; Valdivia & Hennebelle, 2014), which will be discussed in section 6.2.

In order to avoid this costly calculation, we introduce a machine learning approach to predict the column density factor for each cell. Once trained, this leads to a significant speedup of the simulation, as the evaluation of the network is six times faster than the actual calculation. Not only does this benefit the calculation of chemical networks, but it can also potentially be used for radiative transfer. Code and data are made available at: `https://github.com/ehoemann/density2attenuation`

6.2 Data

As a test example for our machine learning approach, we use a continuously driven turbulent 3D-box simulation with a turbulent Mach number of 5. The simulation was performed with RAMSES (Teyssier, 2002), a hydrodynamic grid code. The simulation volume was $(5\,\mathrm{pc})^3$ with a resolution of $(0.0195\,\mathrm{pc})^3$ and periodic boundary conditions. The simulation evolved for nearly 40 Myr with 80 evenly spaced outputs. As the produced density cubes are rather large $(256)^3$ we decided to reduce the input in a first step to boxes of $(80)^3$ voxels. Thus, we could create a training set out of the sub-boxes of the simulation. 152 boxes were used, which we mirrored to increase the training sample, leading to a total of 564 density distributions which we used as input for our machine learning model.

For supervised learning, labels for the input have to be provided. Thus, we used the established method to determine the column density in a simulation via the so-called ray tracing approach (e. g. Razoumov & Scott, 1999; Abel et al., 1999; Raga et al., 1999). For each cell with index i, j, k the density is summed along several rays r, evenly covering the sphere around the cell, giving the local average column density:

$$\bar{N}_{ijk} = \frac{1}{N_{Rays}} \sum_{Rays} \rho_{ijk} \mathrm{d}r \tag{6.1}$$

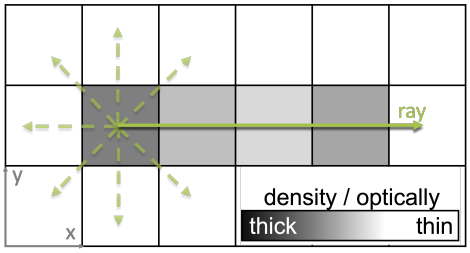

Figure 6.1: Example how a ray is traced for a specific cell. The rays start at the origin of the cell and sum up density until they reach a pixel below a certain column density.

We stop the summation along the ray if it reaches a voxel with low column density, as the ray can escape from there. The lower threshold for column density was set to $6.05 \times 10^{-5}\,\mathrm{g\,cm^{-2}}$ in this study, a graphical illustration is given in Figure 6.1. We define the column density factor η as:

$$\eta_{ijk} = \exp(-\bar{N}_{ijk}). \tag{6.2}$$

With this, the attenuation can be determined as $\chi_{ijk} = \eta_{ijk} \exp(\sigma)$, where σ is the wavelength-dependent absorption cross-section.

Since we loop over every cell and the number of rays, this method is computationally very expensive and strongly depends on resolution, the amount of voxels and the number of rays. Hence, there have been already some modified ray tracing approaches to reduce computing time (e. g. Razoumov & Cardall, 2005; Cantalupo & Porciani, 2011; Valdivia & Hennebelle, 2014). However, a machine learning approach does not have to loop over all the rays and thus could lead to a significant speedup.

6.3 Model

To determine the column density factors via machine learning we used a U-Net architecture. U-Nets were first used for biomedical image segmentation (Ronneberger et al., 2015), but are recently also applied in physics (e. g. He et al., 2019; Chen et al., 2020; Stachenfeld et al., 2021; Grassi et al., 2021; Wadekar et al., 2021; Jamieson et al., 2022). It consists of a de- and encoder, see Figure 6.2. First, the network is reduced by several convolution and pooling operations and then scaled up again using the spacial information stored while down sampling. As input the whole 3D density cube is inserted, in this case ($80 \times 80 \times 80$). The desired output is the 3D cube of column density factors ($40 \times 40 \times 40$), which are known from the ray tracing approach. We chose the input to be of higher dimension than the output since the local average column density depends on its surroundings and, thus, reasonable predictions can only be made for embedded voxels. Furthermore, input and output data were normalized using the mean and standard deviation (respectively, for density and column density factor) over all simulations, which made the code converge much easier.

After producing the predicted column density factors $\hat{y}$, the loss, given by the mean squared error (MSE), determines the distance between the prediction and the ground truth y, which in this case is the column density factors calculated by ray tracing. We weighted the contribution of each voxel to the loss function, to address that low column

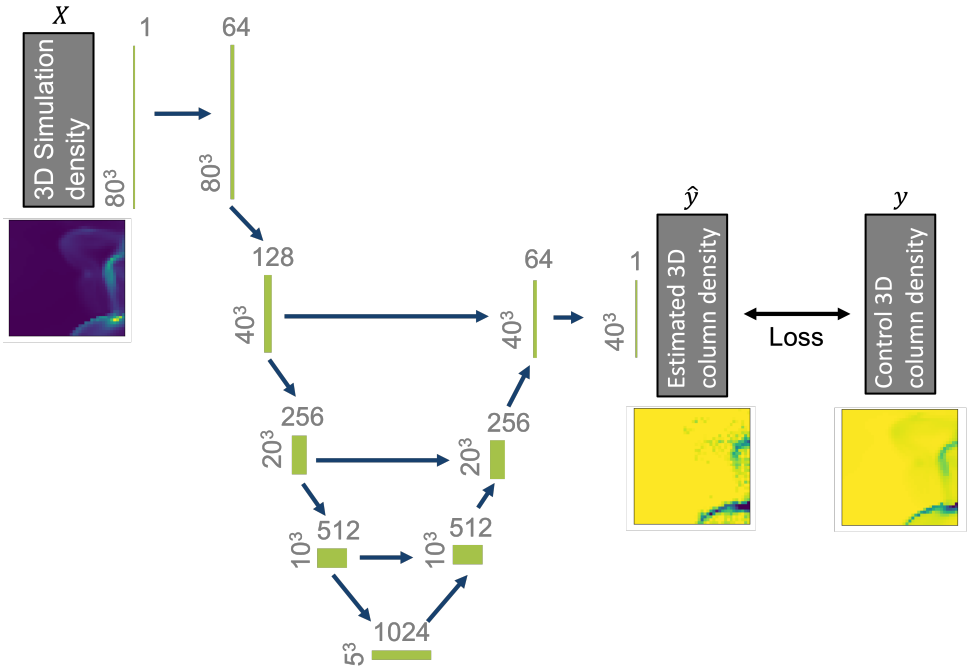

Figure 6.2: 3D U-Net adapted form the 2D version in Ronneberger et al. (2015) (licence: GNU GPL). Determine the 3D column density factors (output) from a 3D density distribution (input). The left part shows the down sampling as the right the up sampling part.

densities are overrepresented, whereas we are interested in the dense parts. The weights for each voxel were the inverse of a fitted power law to the occurrence of its column density (occurrence is depicted in Figure 6.4), although an exponential function is a better representation the network performed worse.

6.4 Results

Example snapshots of the results are given in Figure 6.3. In the first step, we performed a proof of concept. For that, we only considered the column density factor calculated by one ray. With a small training set, we overfitted the data (loss: MSE, without weights), which is displayed in the first row of Figure 6.3. The first column shows the inserted density structure, the second the column density factor determined with the ray tracing approach and in contrast to the machine learning approach in the third column. In the last column, the residuals between the two approaches are depicted.

The general model was done with the full data set described in Section 6.2. As can be seen in the second row of Figure 6.3 the structure is recovered quite well for the training data. However, an example of the test set is given in the third row where the high-density regions are not captured. This is also depicted in Figure 6.4, on the left-hand side the occurrence of column density factors in the two approaches are compared for the whole data set, where the machine learning approach misses the high-density part. The right-hand side shows the ratio between the 2D power spectra of the two methods of a subset

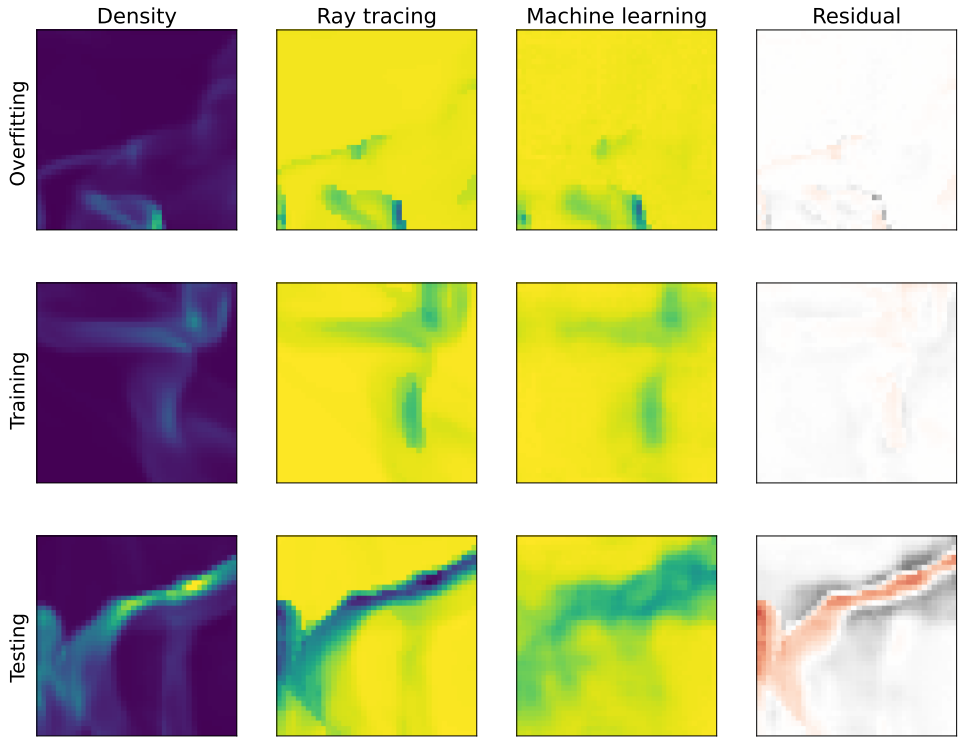

Figure 6.3: Comparison of the density input (first column), the column density factor determined with the ray tracing method (second column) and the machine learning method (third column) and the residuals from the two approaches (fourth column). The first row shows an example of the overfitted data, the second the bigger training set and the third the testing set.

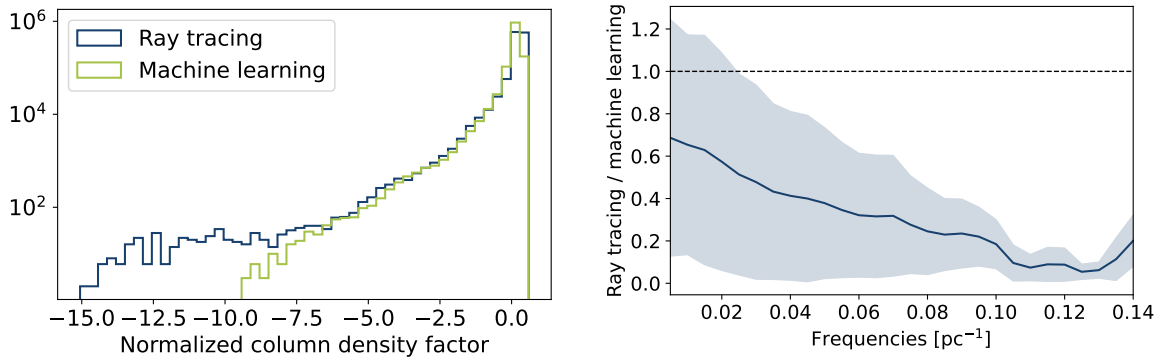

Figure 6.4: Left: The histogram shows the normalized column density factor in the simulation. Green indicates the machine learning approach and blue the ray tracing method. They agree well for the low column density part but show strong deviations for the dense one.
Right: The ratio between the 2D power spectra of the two methods of several simulations. For low frequencies,e. g. large scales, they agree well and for small scales, they deviate strongly.

of the simulation. It shows that the large structures are reproduced, whereas the small structures are smeared out and deviate strongly.

6.5 Discussion and Conclusion

This study shows a proof of concept that column density factors can be determined by machine learning, as the training data is reproduced well. However, further work has to be done before applying this approach to simulations during runtime, since we see strong deviations in the testing set. The accuracy of the prediction has to be increased possibly with a bigger training set and an optimized set of hyperparameters.

The considered data contained only results from one single turbulent box simulation. It needs to be tested, how the network performs on different simulations or different setups, in order to see how well it can be generalised.

Several run time tests showed that one can expect the machine learning method to achieve a speedup of a factor of six in comparison to the classical ray tracing approach. The tests were performed each on one identical CPU.

Acknowledgments

I thank the Simons Foundation for the great opportunity to do this project as part of the 2022 Flatiron Machine Learning X Science Summer School. Special thanks to my mentors Shirley Ho and Miles Cranmer for the organization of the program, helpful discussions and a lot of new insights and also to the other participants of the summer school, especially Thomas Pfeil and Roy Friedman.

Chapter 7

Final remarks

The thesis demonstrated how filaments merge, fragment, and collapse.

In the first paper, we showed that filaments can only merge under specific requirements. Since the timescales on which filaments merge and on which filaments collapse are similar, initial conditions such as velocity, mass, and distance determine whether two filaments can merge. We derived analytic models to describe the merger of two parallel filaments and how cores form at the end of a filament, validated by hydrodynamic simulations. We compared the corresponding timescales of merging and edge effect formation to the overall collapse time of a filament, which leads to quantitative constraints: mergers are expected for filaments with high velocities ($> 0.3\,\mathrm{km\,s^{-1}}$) and small initial distances ($< 0.4\,\mathrm{pc}$).

In the second paper, we developed a model which describes the longitudinal collapse of a filament, assuming a two-phase approach. The first phase is purely dominated by the self-gravity of the filament. Since the acceleration at the filament's ends is nearly independent of its length, the core feels a uniform acceleration in this phase. At some point, the ram pressure of the swept-up gas inside the filament counterbalances the self-gravity of the filament, leading to a uniform inward movement in the second phase. By assuming an instantaneous transition between the phases, an analytic solution was found for the evolution of the filament length. We could then determine the collapse timescale of a filament which explains the empirical timescale found already in Clarke & Whitworth (2015). Although the analytic solution was derived for filaments with a uniform density distribution, we found that it is basically independent of their radial profile and thus also a good approximation for filaments in hydrostatic equilibrium and for observed profiles which tend to be flatter.

In the third paper, we showed that the dominant fragmentation mechanism depends on the end region of the filament. Since a density gradient at the filament end softens the acceleration in this region, the edge effect can be slowed down but not stopped since the collapse is also delayed. If the slowdown is sufficient, perturbations inside the filament can grow faster than the edge effect itself. By comparing the timescales on which perturbations grow and end cores are created, we found a critical gradient for which the two effects occur at the same time. Thus, filaments with shallower density gradients fragment mainly through the growth of perturbations whereas filaments with steeper gradients form dominant end cores which was confirmed by hydrodynamic simulations. However, the simulations showed deviations from the critical gradient for low line-mass

filaments because of the approximations used in the derivation. Besides, the critical gradient depends not only on the criticality and density of the filament but also on the perturbation strength. For the observed perturbation strength, filaments with $f > 0.7$ would always grow perturbations faster than end cores.

In the fourth paper, we demonstrate that tuning fork-like structures, which are observed in the ISM, can be the result of filament mergers. Considering that a filament merger undergoes long-lived oscillations, an angle between the axes of the merging filaments leads to oscillations along the resulting structure. These produce peaks in velocity dispersion and column density which can be used as merger indicators in observations. We found such signatures in the ALMA observations of LDN 1641-North in the Orion A tail, suggesting that this structure has been created by a merger.

Finally, we showed some first approaches using machine learning to speed up hydrodynamic simulations. The integration of chemistry in turbulent ISM simulations is computationally very expensive due to the calculation of attenuation coefficients for external UV irradiation. We developed a three-dimensional U-Net which determines attenuation coefficients from the density distribution of the simulation. The overall structure is already well reproduced by our network which shows that it is a good proof of concept. However, a larger data set and further optimisation of hyperparameters are needed to predict the small-scale features and the underrepresented high-density regions.

The new findings pose a lot of new questions that should be addressed to further understand the physics of star-forming filaments.

The merging of filaments needs to be investigated in more detail. Comparing higher-resolution observations with simulations can enhance our confidence that tuning fork-like structures are produced by filament mergers since they can better resolve the anticipated oscillation. In addition, a more statistical analysis would be necessary to show whether the already observed features are a coincidence or a common feature. From the theoretical side, there are also many questions to unravel. The quantitative dependency between initial and resulting quantities is yet unknown and needs to be investigated via a parameter study. Important parameters in that regard would be the amplitude heights, line-masses, merging angles, velocities, and outside pressures. It would also be interesting to investigate how the merging of filaments triggers star formation and how it influences the fragmentation modes. We already saw that the common fragmentation schemes do not apply to filament mergers where the process is way more chaotic and dominated by the merger of sink particles. This also raises the question of whether filament mergers could be a scenario for high-mass star formation. Since the cores are triggered by the merger and not by the growth of perturbations, it is not restricted to the mass limit given by perturbation theory. With several filaments merging hub-like features may be created, which are observationally already indicated to host high-mass star formation. Consequently, simulations with a central gravitational potential would be interesting, where several filaments converge to a joint centre.

For the critical gradient, it would be interesting to see whether observations can confirm that this density gradient suppresses the edge effect. Observations of filament ends in different environments, with and without edge effect, would be necessary to validate this prediction. From the theory side, it would be interesting to see how the density gradient influences the overall filament lifetime since it not only slows down the

edge effect but also the overall collapse. This could have an impact on the lifetimes of filaments.

The machine learning project where we determined attenuation coefficients of UV irradiation with a neural network is only at its start, therefore, there is still a lot to improve. First, a bigger and statistically more relevant sample is needed to train the network. High-density regions have to be more prominent, such that it is easier for the network to learn these features and to fully converge. Furthermore, an adjustment of the hyperparameters would be necessary. For example, the loss function needs to be modified to better emphasise what features are important for the network to reproduce. In addition, the shape of the network and the data normalisation are parameters which could be optimised. The network would need to be tested during the simulation in comparison to the ray tracing approach to determine how accurate its predictions need to be to capture the underlying physics correctly. Moreover, a study on the actual speed up for simulations has to be done, also in comparison to non-classical ray tracing approaches.

Altogether, isolated simulations are necessary to understand the fundamental physical processes governing filaments. The determination and comparison of the corresponding timescales provide us insights into their initial conditions, evolution, and fragmentation. In the long run, these simulations have to be advanced step by step to determine the influence of the surroundings, such as magnetic fields, stellar feedback, or turbulence. The comparison between simulations and observations highlights the accuracy of state-of-the-art models and allows to reassess the current understanding of the underlying physics. As both simulations and observations will advance in resolution driven by better technical equipment and higher computing power, the forthcoming years and decades will be an exciting era to study the physics of star formation.

Bibliography

Abel, T., Norman, M. L., and Madau, P. (1999), *Photon-conserving Radiative Transfer around Point Sources in Multidimensional Numerical Cosmology*, ApJ, 523(1), 66

Aguti, E. D., Lada, C. J., Bergin, E. A., et al. (2007), *The Dynamical State of the Starless Dense Core FeSt 1-457: A Pulsating Globule?*, ApJ, 665(1), 457

Alves, J., Lada, C. J., Lada, E. A., et al. (1998), *Dust Extinction and Molecular Cloud Structure: L977*, ApJ, 506(1), 292

Anathpindika, S. V. and Francesco, J. D. (2021), *On filament fragmentation and the impact of ambient environment on it*, MNRAS, 502(1), 564

André, P. (2017), *Interstellar filaments and star formation*, Comptes Rendus Geoscience, 349(5), 187

André, P., Di Francesco, J., Ward-Thompson, D., et al. (2014), *From Filamentary Networks to Dense Cores in Molecular Clouds: Toward a New Paradigm for Star Formation*, in *Protostars and Planets VI*, edited by H. Beuther, R. S. Klessen, C. P. Dullemond, T. Henning, 27, University of Arizona Press

André, P., Men'shchikov, A., Bontemps, S., et al. (2010), *From filamentary clouds to prestellar cores to the stellar IMF: Initial highlights from the Herschel Gould Belt Survey*, A&A, 518, L102

Arcoragi, J.-P., Bonnell, I., Martel, H., et al. (1991), *Fragmentation of Elongated Cylindrical Clouds. II. Polytropic Clouds*, ApJ, 380, 476

Arzoumanian, D., André, P., Didelon, P., et al. (2011), *Characterizing interstellar filaments with Herschel in IC 5146*, A&A, 529, L6

Arzoumanian, D., André, P., Könyves, V., et al. (2019), *Characterizing the properties of nearby molecular filaments observed with Herschel*, A&A, 621, A42

Arzoumanian, D., André, P., Peretto, N., and Könyves, V. (2013), *Formation and evolution of interstellar filaments. Hints from velocity dispersion measurements*, A&A, 553, A119

Bally, J., Langer, W. D., Stark, A. A., and Wilson, R. W. (1987), *Filamentary Structure in the Orion Molecular Cloud*, ApJ, 312, L45

Bastien, P. (1983), *Gravitational collapse and fragmentation of isothermal, non-rotating, cylindrical clouds*, A&A, 119(1), 109

Bastien, P., Arcoragi, J.-P., Benz, W., et al. (1991), *Fragmentation of Elongated Cylindrical Clouds. I. Isothermal Clouds*, ApJ, 378, 255

Batten, P., Clarke, N., Lambert, C., and Causon, D. M. (1997), *On the Choice of Wavespeeds for the HLLC Riemann Solver*, SIAM Journal on Scientific Computing, 18(6), 1553

Berger, M. J. and Colella, P. (1989), *Local Adaptive Mesh Refinement for Shock Hydrodynamics*, Journal of Computational Physics, 82(1), 64

Berger, M. J. and Oliger, J. (1984), *Adaptive Mesh Refinement for Hyperbolic Partial Differential Equations*, Journal of Computational Physics, 53(3), 484

Bhadari, N. K., Dewangan, L. K., Pirogov, L. E., and Ojha, D. K. (2020), *Star-forming Sites IC 446 and IC 447: An Outcome of End-dominated Collapse of Monoceros R1 Filament*, ApJ, 899(2), 167

Bodenheimer, P., Laughlin, G., Rozyczka, M., et al. (2006), *Numerical Methods in Astrophysics: An Introduction*, Series in Astronomy and Astrophysics, Taylor & Francis

Bohlin, R. C., Savage, B. D., and Drake, J. F. (1978), *A survey of interstellar H I from Lalpha absorption measurements. II.*, ApJ, 224, 132

Burkert, A. and Hartmann, L. (2004), *Collapse and Fragmentation in Finite Sheets*, ApJ, 616(1), 288

Busquet, G., Zhang, Q., Palau, A., et al. (2013), *Unveiling a Network of Parallel Filaments in the Infrared Dark Cloud G14.225-0.506*, ApJ, 764(2), L26

Cai, M. J. and Taam, R. E. (2010), *The Equilibrium Structure of Prolate Magnetized Molecular Cores*, ApJ, 709(1), L79

Cantalupo, S. and Porciani, C. (2011), *RADAMESH: cosmological radiative transfer for Adaptive Mesh Refinement simulations*, MNRAS, 411(3), 1678

Chen, C., Li, Y., Villaescusa-Navarro, F., et al. (2020), *Learning the Evolution of the Universe in N-body Simulations*, arXiv e-prints, arXiv:2012.05472

Cheng, Y., Tan, J. C., Caselli, P., et al. (2021), *Star Formation in a Strongly Magnetized Cloud*, ApJ, 916(2), 78

Chira, R. A., Kainulainen, J., Ibáñez-Mejía, J. C., et al. (2018), *On the fragmentation of filaments in a molecular cloud simulation*, A&A, 610, A62

Clarke, S. D. and Whitworth, A. P. (2015), *Investigating the global collapse of filaments using smoothed particle hydrodynamics*, MNRAS, 449(2), 1819

Clarke, S. D., Whitworth, A. P., Duarte-Cabral, A., and Hubber, D. A. (2017), *Filamentary fragmentation in a turbulent medium*, MNRAS, 468(2), 2489

Cox, N. L. J., Arzoumanian, D., André, P., et al. (2016), *Filamentary structure and magnetic field orientation in Musca*, A&A, 590, A110

Dewangan, L. K., Pirogov, L. E., Ryabukhina, O. L., et al. (2019), *Observational Signatures of End-dominated Collapse in the S242 Filamentary Structure*, ApJ, 877(1), 1

Draine, B. T. and Lee, H. M. (1984), *Optical Properties of Interstellar Graphite and Silicate Grains*, ApJ, 285, 89

Egan, M. P., Shipman, R. F., Price, S. D., et al. (1998), *A Population of Cold Cores in the Galactic Plane*, ApJ, 494(2), L199

Fehér, O., Tóth, L. V., Ward-Thompson, D., et al. (2016), *Structure and stability in TMC-1: Analysis of NH_3 molecular line and Herschel continuum data*, A&A, 590, A75

Fiege, J. D. and Pudritz, R. E. (2000), *Helical fields and filamentary molecular clouds - I*, MNRAS, 311(1), 85

Fiege, J. D. and Pudritz, R. E. (2000), *Helical fields and filamentary molecular clouds — II. Axisymmetric stability and fragmentation*, MNRAS, 311(1), 105

Field, G. B. (1965), *Thermal Instability.*, ApJ, 142, 531

Field, G. B., Goldsmith, D. W., and Habing, H. J. (1969), *Cosmic-Ray Heating of the Interstellar Gas*, ApJ, 155, L149

Fischera, J. and Martin, P. G. (2012), *Estimating distance, pressure, and dust opacity using submillimeter observations of self-gravitating filaments*, A&A, 547, A86

Fischera, J. and Martin, P. G. (2012), *Physical properties of interstellar filaments*, A&A, 542, A77

Frau, P., Girart, J. M., Alves, F. O., et al. (2015), *Formation of dense structures induced by filament collisions. Correlation of density, kinematics, and magnetic field in the Pipe nebula*, A&A, 574, L6

Fukui, Y., Habe, A., Inoue, T., et al. (2021), *Cloud-cloud collisions and triggered star formation*, PASJ, 73, S1

Gehman, C. S., Adams, F. C., Fatuzzo, M., and Watkins, R. (1996), *Wave Motions in Molecular Clouds: Results in Two Dimensions*, ApJ, 457, 718

Goldsmith, P. F. and Langer, W. D. (1978), *Molecular cooling and thermal balance of dense interstellar clouds.*, ApJ, 222, 881

Goodman, A. A., Alves, J., Beaumont, C. N., et al. (2014), *The Bones of the Milky Way*, ApJ, 797(1), 53

Gould, R. J. and Salpeter, E. E. (1963), *The Interstellar Abundance of the Hydrogen Molecule. I. Basic Processes.*, ApJ, 138, 393

Grassi, T., Bovino, S., Schleicher, D. R. G., et al. (2014), *KROME - a package to embed chemistry in astrophysical simulations*, Monthly Notices of the RAS, 439(3), 2386

Grassi, T., Nauman, F., Ramsey, J. P., et al. (2021), *Reducing the complexity of chemical networks via interpretable autoencoders*, arXiv e-prints, arXiv:2104.09516

Gritschneder, M., Heigl, S., and Burkert, A. (2017), *Oscillating filaments. I. Oscillation and geometrical fragmentation*, ApJ, 834(2), 202

Hacar, A., Clark, S. E., Heitsch, F., et al. (2023), *Initial Conditions for Star Formation: a Physical Description of the Filamentary ISM*, in *Protostars and Planets VII*, edited by S. Inutsuka, Y. Aikawa, T. Muto, K. Tomida, M. Tamura, 153, ASPCS

Hacar, A. and Tafalla, M. (2011), *Dense core formation by fragmentation of velocity-coherent filaments in L1517*, A&A, 533, A34

Hacar, A., Tafalla, M., Forbrich, J., et al. (2018), *An ALMA study of the Orion Integral Filament: I. Evidence for narrow fibers in a massive cloud*, A&A, 610, A77

Hacar, A., Tafalla, M., Kauffmann, J., and Kovács, A. (2013), *Cores, filaments, and bundles: hierarchical core formation in the L1495/B213 Taurus region*, A&A, 554, A55

Hanawa, T., Yamamoto, S., and Hirahara, Y. (1994), *Sequential Star Formation in Taurus Molecular Cloud 1*, ApJ, 420, 318

Hartmann, L. and Burkert, A. (2007), *On the Structure of the Orion A Cloud and the Formation of the Orion Nebula Cluster*, ApJ, 654(2), 988

Haslam, C. G. T., Salter, C. J., Stoffel, H., and Wilson, W. E. (1982), *A 408-MHZ All-Sky Continuum Survey. II. The Atlas of Contour Maps*, A&AS, 47, 1

He, S., Li, Y., Feng, Y., et al. (2019), *Learning to predict the cosmological structure formation*, Proceedings of the National Academy of Sciences, 116(28), 13825

Heigl, S., Burkert, A., and Gritschneder, M. (2018), *Accretion-driven turbulence in filaments - I. Non-gravitational accretion*, Monthly Notices of the RAS, 474(4), 4881

Heigl, S., Burkert, A., and Hacar, A. (2016), *Non-linear dense core formation in the dark cloud L1517*, Monthly Notices of the RAS, 463(4), 4301

Heigl, S., Gritschneder, M., and Burkert, A. (2020), *Accretion-driven turbulence in filaments II: effects of self-gravity*, Monthly Notices of the RAS, 495(1), 758

Heigl, S., Hoemann, E., and Burkert, A. (2021), *Taking off the edge – simultaneous filament and end core formation*, arXiv e-prints, arXiv:2112.12640

Heigl, S., Hoemann, E., and Burkert, A. (2022), *Taking off the edge - simultaneous filament and end core formation*, MNRAS, 517(4), 5272

Hennebelle, P., Pérault, M., Teyssier, D., and Ganesh, S. (2001), *Infrared dark clouds from the ISOGAL survey. Constraints on the interstellar extinction curve*, A&A, 365, 598

Heyer, M., Krawczyk, C., Duval, J., and Jackson, J. M. (2009), *Re-Examining Larson's Scaling Relationships in Galactic Molecular Clouds*, ApJ, 699(2), 1092

Hill, T., Motte, F., Didelon, P., et al. (2011), *Filaments and ridges in Vela C revealed by Herschel: from low-mass to high-mass star-forming sites*, A&A, 533, A94

Hoemann, E., Heigl, S., and Burkert, A. (2021), *Merging filaments I: a race against collapse*, Monthly Notices of the RAS, 507(3), 3486

Hoemann, E., Heigl, S., and Burkert, A. (2022), *Filament collapse: A two phase process*, arXiv e-prints, arXiv:2203.07002

Hoemann, E., Heigl, S., and Burkert, A. (2023a), *Filament collapse: a two phase process*, MNRAS, 521(4), 5152

Hoemann, E., Heigl, S., and Burkert, A. (2023b), *Filament fragmentation: Density gradients suppress end dominated collapse*, arXiv e-prints, arXiv:2307.11162

Hollenbach, D. and Salpeter, E. E. (1971), *Surface Recombination of Hydrogen Molecules*, ApJ, 163, 155

Hosseinirad, M., Naficy, K., Abbassi, S., and Roshan, M. (2017), *Gravitational instability of filamentary molecular clouds, including ambipolar diffusion*, MNRAS, 465(2), 1645

Inutsuka, S.-I. and Miyama, S. M. (1992), *Self-similar Solutions and the Stability of Collapsing Isothermal Filaments*, ApJ, 388, 392

Jamieson, D., Li, Y., Alves de Oliveira, R., et al. (2022), *Field Level Neural Network Emulator for Cosmological N-body Simulations*, arXiv e-prints, arXiv:2206.04594

Kainulainen, J., Hacar, A., Alves, J., et al. (2016), *Gravitational fragmentation caught in the act: the filamentary Musca molecular cloud*, A&A, 586, A27

Kashiwagi, R., Iwasaki, K., and Tomisaka, K. (2023), *Simulation of Head-on Collisions Between Filamentary Molecular Clouds Threaded by a Lateral Magnetic Field and Subsequent Evolution*, arXiv e-prints, arXiv:2307.07698

Keto, E. and Burkert, A. (2014), *From filaments to oscillating starless cores*, MNRAS, 441(2), 1468

Könyves, V., André, P., Men'shchikov, A., et al. (2015), *A census of dense cores in the Aquila cloud complex: SPIRE/PACS observations from the Herschel Gould Belt survey*, A&A, 584, A91

Kumar, M. S. N., Palmeirim, P., Arzoumanian, D., and Inutsuka, S. I. (2020), *Unifying low- and high-mass star formation through density-amplified hubs of filaments. The highest mass stars (¿100 $M_\odot$) form only in hubs*, A&A, 642, A87

Kumar, M. S. N., Arzoumanian, D., Men´shchikov, A., et al. (2022), *Filament coalescence and hub structure in Mon R2 - Implications for massive star and cluster formation*, A&A, 658, A114

Lada, C. J., Alves, J., and Lada, E. A. (1999), *Infrared Extinction and the Structure of the IC 5146 Dark Cloud*, ApJ, 512(1), 250

Larson, R. B. (1981), *Turbulence and star formation in molecular clouds.*, MNRAS, 194, 809

Larson, R. B. (1985), *Cloud fragmentation and stellar masses*, MNRAS, 214(3), 379

Li, G.-X., Burkert, A., Megeath, T., and Wyrowski, F. (2016), *Gravitational acceleration and edge effects in molecular clouds*, arXiv e-prints, arXiv:1603.05720

Li, Z.-Y. (2001), *Ring Formation in Magnetically Subcritical Clouds and Multiple-Star Formation*, ApJ, 556(2), 813

Lizano, S. and Shu, F. H. (1989), *Molecular Cloud Cores and Bimodal Star Formation*, ApJ, 342, 834

Mathis, J. S., Rumpl, W., and Nordsieck, K. H. (1977), *The size distribution of interstellar grains.*, ApJ, 217, 425

Mattern, M., Kainulainen, J., Zhang, M., and Beuther, H. (2018), *Structure and fragmentation of a high line-mass filament: Nessie*, A&A, 616, A78

McKee, C. F. and Ostriker, J. P. (1977), *A theory of the interstellar medium: three components regulated by supernova explosions in an inhomogeneous substrate.*, ApJ, 218, 148

Megeath, S. T., Gutermuth, R., Muzerolle, J., et al. (2012), *The Spitzer Space Telescope Survey of the Orion A and B Molecular Clouds. I. A Census of Dusty Young Stellar Objects and a Study of Their Mid-infrared Variability*, AJ, 144(6), 192

Megeath, S. T., Gutermuth, R., Muzerolle, J., et al. (2016), *The Spitzer Space Telescope Survey of the Orion A and B Molecular Clouds. II. The Spatial Distribution and Demographics of Dusty Young Stellar Objects*, AJ, 151(1), 5

Menten, K. M., Reid, M. J., Forbrich, J., and Brunthaler, A. (2007), *The distance to the Orion Nebula*, A&A, 474(2), 515

Miettinen, O. and Harju, J. (2010), *LABOCA mapping of the infrared dark cloud MSXDC G304.74+01.32*, A&A, 520, A102

Moeckel, N. and Burkert, A. (2015), *The formation of filamentary bundles in turbulent molecular clouds*, ApJ, 807, 67

Molinari, S., Swinyard, B., Bally, J., et al. (2010), *Clouds, filaments, and protostars: The Herschel Hi-GAL Milky Way*, A&A, 518, L100

Motte, F., Bontemps, S., and Louvet, F. (2018), *High-Mass Star and Massive Cluster Formation in the Milky Way*, ARA&A, 56, 41

Myers, P. C. (2009), *Filamentary Structure of Star-forming Complexes*, ApJ, 700(2), 1609

Nagasawa, M. (1987), *Gravitational Instability of the Isothermal Gas Cylinder with an Axial magnetic Field*, Progress of Theoretical Physics, 77(3), 635

Nakamura, F., Sugitani, K., Tanaka, T., et al. (2014), *Cluster Formation Triggered by Filament Collisions in Serpens South*, ApJ, 791(2), L23

Ostriker, J. (1964), *The Equilibrium of Polytropic and Isothermal Cylinders.*, ApJ, 140(2), 1056

Palmeirim, P., André, P., Kirk, J., et al. (2013), *Herschel view of the Taurus B211/3 filament and striations: evidence of filamentary growth?*, A&A, 550, A38

Perault, M., Omont, A., Simon, G., et al. (1996), *First ISOCAM images of the Milky Way.*, A&A, 315, L165

Peretto, N. and Fuller, G. A. (2009), *The initial conditions of stellar protocluster formation. I. A catalogue of Spitzer dark clouds*, A&A, 505(1), 405

Peretto, N., Fuller, G. A., Duarte-Cabral, A., et al. (2013), *Global collapse of molecular clouds as a formation mechanism for the most massive stars*, A&A, 555, A112

Pon, A., Toalá, J. A., Johnstone, D., et al. (2012), *Aspect ratio dependence of the free-fall time for non-spherical symmetries*, ApJ, 756(2), 145

Raga, A. C., Mellema, G., Arthur, S. J., et al. (1999), *3D Transfer of the Diffuse Ionizing Radiation in ISM Flows and the Preionization of a Herbig-Haro Working Surface*, Rev. Mex. Astron. Astrofis., 35, 123

Razoumov, A. O. and Cardall, C. Y. (2005), *Fully threaded transport engine: new method for multi-scale radiative transfer*, MNRAS, 362(4), 1413

Razoumov, A. O. and Scott, D. (1999), *Three-dimensional numerical cosmological radiative transfer in an inhomogeneous medium*, MNRAS, 309(2), 287

Recchi, S., Hacar, A., and Palestini, A. (2013), *Nonisothermal filaments in equilibrium*, A&A, 558, A27

Recchi, S., Hacar, A., and Palestini, A. (2014), *On the equilibrium of rotating filaments*, MNRAS, 444(2), 1775

Redman, M. P., Keto, E., and Rawlings, J. M. C. (2006), *Oscillations in the stable starless core Barnard 68*, MNRAS, 370(1), L1

Ronneberger, O., Fischer, P., and Brox, T. (2015), *U-Net: Convolutional Networks for Biomedical Image Segmentation*, arXiv e-prints, arXiv:1505.04597

Rouleau, F. and Bastien, P. (1990), *Collapse and Fragmentation of Isothermal and Polytropic Cylindrical Clouds*, ApJ, 355, 172

Roy, A., André, P., Arzoumanian, D., et al. (2015), *Possible link between the power spectrum of interstellar filaments and the origin of the prestellar core mass function*, A&A, 584, A111

Rubin, A., Gal-Yam, A., Cia, A. D., et al. (2016), *Type II supernova energetics and comparison of light curves to shock-cooling models*, ApJ, 820(1), 33

Schmiedeke, A., Pineda, J. E., Caselli, P., et al. (2021), *Dissecting the Supercritical Filaments Embedded in the 0.5 pc Subsonic Region of Barnard 5*, ApJ, 909(1), 60

Schneider, N., Csengeri, T., Bontemps, S., et al. (2010), *Dynamic star formation in the massive DR21 filament*, A&A, 520, A49

Schneider, S. and Elmegreen, B. G. (1979), *A catalog of dark globular filaments.*, Astrophysical Journal, Supplement, 41, 87

Seifried, D. and Walch, S. (2015), *The impact of turbulence and magnetic field orientation on star-forming filaments*, Monthly Notices of the RAS, 452(3), 2410

Shu, F. (1991), *The Physics of Astrophysics*, number Bd. 2 in G - Reference,Information and Interdisciplinary Subjects Series, University Science Books

Smith, B. D., Bryan, G. L., Glover, S. C. O., et al. (2017), *GRACKLE: a chemistry and cooling library for astrophysics*, MNRAS, 466(2), 2217

Smith, R. J., Glover, S. C. O., and Klessen, R. S. (2014), *On the nature of star-forming filaments – I. Filament morphologies*, MNRAS, 445(3), 2900

Solomon, P. M., Rivolo, A. R., Barrett, J., and Yahil, A. (1987), *Mass, Luminosity, and Line Width Relations of Galactic Molecular Clouds*, ApJ, 319, 730

Stachenfeld, K., Fielding, D. B., Kochkov, D., et al. (2021), *Learned Coarse Models for Efficient Turbulence Simulation*, arXiv e-prints, arXiv:2112.15275

Stodólkiewicz, J. S. (1963), *On the Gravitational Instability of Some Magneto-Hydrodynamical Systems of Astrophysical Interest. Part III.*, Acta Astron., 13, 30

Tafalla, M. and Hacar, A. (2015), *Chains of dense cores in the Taurus L1495/B213 complex*, A&A, 574, A104

Teyssier, R. (2002), *Cosmological hydrodynamics with adaptive mesh refinement*, A&A, 385(1), 337–364

Toalá, J. A., Vázquez-Semadeni, E., and Gómez, G. C. (2011), *The free-fall time of finite sheets and filaments*, ApJ, 744(2), 190

Tomisaka, K. (1991), *The Equilibria and Evolutions of Magnetized, Rotating, Isothermal Clouds. V. The Effect of the Toroidal Field*, ApJ, 376, 190

Tomisaka, K. (2014), *Magnetohydrostatic Equilibrium Structure and Mass of Filamentary Isothermal Cloud Threaded by Lateral Magnetic Field*, ApJ, 785(1), 24

Toro, E. F. (1999), *Riemann Solvers and Numerical Methods for Fluid Dynamics*, Springer Berlin, Heidelberg

Toro, E. F., Spruce, M., and Speares, W. (1994), *Restoration of the contact surface in the HLL-Riemann solver*, Shock Waves, 4(1), 25

Treviño-Morales, S. P., Fuente, A., Sánchez-Monge, Á., et al. (2019), *Dynamics of cluster-forming hub-filament systems. The case of the high-mass star-forming complex Monoceros R2*, A&A, 629, A81

Valdivia, V. and Hennebelle, P. (2014), *A fast tree-based method for estimating column densities in adaptive mesh refinement codes. Influence of UV radiation field on the structure of molecular clouds*, A&A, 571, A46

van Leer, B. (1979), *Towards the Ultimate Conservative Difference Scheme. V. A Second-Order Sequel to Godunov's Method*, Journal of Computational Physics, 32(1), 101

Wadekar, D., Villaescusa-Navarro, F., Ho, S., and Perreault-Levasseur, L. (2021), *HInet: Generating Neutral Hydrogen from Dark Matter with Neural Networks*, ApJ, 916(1), 42

Walch, S., Girichidis, P., Naab, T., et al. (2015), *The SILCC (SImulating the LifeCycle of molecular Clouds) project – I. Chemical evolution of the supernova-driven ISM*, Monthly Notices of the RAS, 454(1), 238

Williams, J. P. (2021), *Introduction to the Interstellar Medium*, Cambridge University Press

Yuan, L., Li, G.-X., Zhu, M., et al. (2020), *Edge collapse and subsequent longitudinal accretion in Filament S242*, A&A, 637, A67

Zernickel, A., Schilke, P., and Smith, R. J. (2013), *The global velocity field of the filament in NGC 6334*, A&A, 554, L2

Zhang, Guo-Yin, André, Ph., Men´shchikov, A., and Wang, Ke (2020), *Fragmentation of star-forming filaments in the X-shaped nebula of the California molecular cloud*, A&A, 642, A76

Acknowledgements

First, I want to thank my supervisor Andreas Burkert for giving me the opportunity to write my thesis in his group, although I was completely new to Astrophysics. Your enthusiasm for science was inspiring and I learned a lot in the last four years.

Second, I thank Stefan Heigl for introducing me to hydrodynamic simulations and the numerous discussions about filaments, numerics and everything in between. Furthermore, I want to thank the whole CAST group for welcoming me so friendly and trying to keep communication alive, especially during the pandemic. Special thanks to Klaus Dolag who keeps the group together, Tadziu Hoffmann for fixing all the technical issues we produce and the secretaries for all the administrative support.

Third, I want to thank my thesis committee Paola Caselli and Leonardo Testi for the helpful advice and new inputs you provided. I also want to thank my collaborators: Andrea Socci and Alvaro Hacar from Vienna for showing me the perspective from an observational point of view, it was always fun working with you. In this course, I also want to thank Kai Widmaier and the whole "filaments" group for all the insightful meetings. Furthermore, I thank Shirley Ho and Miles Cranmer for giving me the possibility to do a summer project at the Flatiron Institute in New York and to expand my knowledge about machine learning, it was a great experience. In addition, I want to thank the AG Zilges at the University of Cologne for introducing me to the world of science during my undergrad studies, I especially want to thank Michelle Färber not only for the comments on my work but also for the many discussions about God and the universe.

What I will definitely miss the most is our fun office, the many pranks, the cake Wednesdays and the most amazing office mates Peter, Thomas, Daniel, Christiane, Sophie, Tommy and Ludwig. Thanks for making up for the long home office period during Covid.

Finally, but most of all, I want to thank my family and friends for your endless support and motivation, I could not have made it without you.